2009

Mechanics guided design of hybrid laser/waterjet system for machining of hard and brittle materials

Dinesh Kalyanasundaram
Iowa State University

Mechanics guided design of hybrid laser/waterjet system for machining hard and brittle materials

by

Dinesh Kalyanasundaram

A dissertation submitted to the graduate faculty

in partial fulfillment of the requirements for the degree of

DOCTOR OF PHILOSOPHY

Major: Mechanical Engineering
Program of study Committee:
Pranav Shrotriya, Major Professor
Pal Molian
Abhijit Chandra
Thomas Rudolphi
Frank Peters

Iowa State University

Ames, Iowa

2009

TABLE OF CONTENTS

ACKNOWLEDGEMENTS

In life there are two segments, one is the pre-achievement period and the other is the post-achievement period. It mostly happens that an individual is always pointed out in the post–achievement era whether the efforts are a success or whether it is a failure, and does not equally take into account of the huge team that have contributed for the work (in the pre-achievement era). It is rather a saddening point that there are no noble prize - equivalent recognitions for best mothers, fathers, teachers, and friends. And since there are none (may be there are some unheard), I would like to contribute all of this success, the pain and the pleasure of this work to the following people.

My mother would be the first in the list who gave me her blood, bones, and muscles and who was never been able recover completely after my birth. A high school graduate who wanted me to top in every single class, taught me to fight always for the better whatever it may cost. I am proud to be the first PhD in my whole family and the credit totally belongs to her. I would equally thank my father and my brother (who has surprisingly started to support my parents more extensively).

The next would be my major professor Dr Pranav Shrotriya whom I would like to thank for his patience, guidance, and encouraging style of research. He helped me a lot in every single aspect of research and to come across a guide/human being/professor like him is a very rare opportunity.

I would like to express my gratitude to Dr Pal Molian, the un-retiring researcher who works like a research student (many a times more than a research student) even after 27 years of completing his PhD. His unparalleled hard working nature has been a great inspiration for me. His presence added spice to the research and answering his questions would be a herculean task by itself.

I would also like to thank Dr Thomas Rudolphi, who is one of my committee members and an iconic figure at Iowa State University, known for his kindness towards students. I consider

myself very lucky to have studied under him. I would also like to thank my other committee members Dr Abhijit Chandra and Dr Frank Peters for having taken time to being part of the committee and the evaluation process.

I have to definitely mention my colleagues/co-workers/lab-mates for their moral and technical support especially to Yilei Zhang, my chief supporter and a "real researcher" who has printed off more journal articles than the whole department has; Jae-Joong Ryu (alias JJ), a wonderful man who is always ready to help everyone; Kanaga Karruppiah (alias KK), an epitome of a human being; Satyam Bhuyan, a tough smiling personality whom you can always bet on; Kyungho Kang, the ever smiling personality; Benjamin Pecholt, my greatest companion and constant debater about science, world politics and nearly everything; Rueben Flesner, the stock market analyst; Xue Zhao, the funny mathematician who considers me very funny; Xiao Ma, the "so-so" personality and Chris Tourek, a simple and a humble individual.

I would have to thank my close friends not for the support but for the trouble they caused to me and which kept me alive. The list starts with Shenbaga Sounder, Hemant Bhanot (an African who calls himself an Indian), Naveen Kumar (Rohit Narrulla), Gowri Shankar, Viswanath, Shamik Das Gupta, Supriyo Das, Saayan Mitra, and Ashutosh Bhanot.

I would also like to thank my other friends in the Badminton Club (Habirah Rosli, Zhen-yan Jin) and the soccer club (Stewart, Alejandro, Sean, Troy, Li, Joseph, Emmanuel, KC-1, KC-2, Charles, Didum). Actually speaking, playing a lot really helped me to revive a lot of energy to work and it helped me pace up the work. I would also like to thank ME staff for their strong support and special thanks to Marti Steelman, Hap steed and Nate Jensen.

PS: A policeman is one who doubts everyone to have caused the problem and a researcher is one who doubts everything to be the source of problem, an order of three higher (Do you know why??).

ABSTRACT

The two main objectives of this work is 1) to develop a mathematical model to efficiently capture the fracture behavior of materials undergoing thermal shock and 2) to design and develop a mechanics based hybrid laser/waterjet manufacturing process that will be able to machine hard and brittle materials at higher speeds and with better cut quality. The mathematical model relates the temperature generated during the machining process to the fracture behavior observed during machining. The hybrid manufacturing processes produces a synergetic effect of both laser and waterjet processes and overcomes the disadvantages of both of them.

The temperature distribution is obtained from the Green's solution of the Fourier Heat Conduction equation. Uncoupled thermoelastic stresses are obtained from the temperature distribution which in-turn is related to the stress intensity factor/Griffith Energy for Mode I crack growth by Bueckner's weight function approach. This model can also be used to predict fracture behavior for given laser processing conditions. This model can also be used to manipulate transformational stresses that occur during machining of high conductive materials. This model can be easily extended to many multi-physics problems involving thermo-elastic behavior.

CHAPTER 1. INTRODUCTION

1.1.Abstract

In this chapter, we will discuss the motivation for the development of the current research work. First, a literature survey on the need for machining ceramics will be discussed along with various traditional machining techniques (diamond grinding, sawing etc) and non-traditional machining techniques (laser cutting and waterjet). Second, we will discuss a hybrid manufacturing process to overcome the disadvantages of the existing machining techniques. Finally, we will present you a synopsis of the various ceramics that have been studied and their related chapter encompassing a detailed journal publication on LWJ machining of the particular ceramic.

1.2.Ceramic Machining

Ceramics are widely used for a variety of applications ranging from microelectronics to prosthetics because of desirable properties such as: high hardness, low chemical reactivity, high volume receptivity at elevated temperatures, low density, low thermal conductivity, and ultra-fine finishing capability[1-4]. The new high-tech materials achieve high levels of strength. Their figures are comparable with those for metals, and generally exceed those of any polymer. The properties of the ceramic material are heavily influenced by those of the particular microstructure. The mechanical and physical properties can be influenced in different ways through the deliberate creation of particular microstructures, a process referred to as "microstructure design". An important point always to bear in mind when applying ceramics is this - ceramics are brittle. The ductility of metal construction materials make metals "good-tempered and well-behaved". The small errors of construction (incorrect tolerance) are taken care due to the ability to disperse local stress peaks through elastic and plastic deformation. Also metals are typically

good electrical and thermal conductors and these properties are independent of orientation. Ceramic materials, on the other hand, are usually electrically and thermally insulating, have high hardness figures, and may have very low thermal expansion. Their shape is, furthermore, extremely stable due to the absence of a capacity for plastic deformation. Compression strengths ten times greater than the bending or tensile strengths can be achieved. In comparison with metals, ceramics are particularly suitable for application at high temperatures, since the characteristics of ceramic materials are altogether less strongly influenced by temperature than metals and even then only at particularly high temperatures. Ceramics offer equally high benefits in terms of corrosion and abrasion resistance. Because of these advantages, we find technical ceramics everywhere for eg: insulators found at each household. Ceramic substrates and parts are the basis for components and modules in all areas of electronics, while in machine and plant construction sliding and bearing elements provide low wear, corrosion-free function. Ceramic construction and insulation materials are indispensable to the industrial furnaces used in high-temperature technology.

Ceramic materials are inorganic and non-metallic. They are generally moulded from a mass of raw material at room temperature, and gain their typical physical properties through a high temperature firing process. In contrast, the Anglo-Saxon term "ceramics" also often includes glass, enamel, glass-ceramic, and inorganic cementitious materials (cement, plaster and lime). The German ceramics industry also distinguishes between coarse and fine ceramics, depending on the particle size in the raw material. The definition according to Hausner applies to the structure of the fired ceramic, specifically to the grain structure. The boundary is considered to lie at grain sizes of between about 0.1 and 0.2 mm. If the elements of the microstructure are smaller than 0.1 mm, which means that they can no longer be detected with the naked eye, the German usage then refers to fine ceramics – regardless of the material.

Technical ceramics refers to ceramic products for engineering applications. Terms commonly seen in literature such as:

- high performance ceramics
- structural ceramics
- construction ceramics
- industrial ceramics
- engineering ceramics
- functional ceramics
- electrical ceramics
- cutting ceramics and
- medical ceramics

Most of these applications require fast processing, tight dimensional tolerance and excellent surface integrity, therefore controlled processing and manufacturing becomes critically important. The high strength, high hardness, low ductility, and low electrical conductivity have significantly increased the challenges in machining these materials. Ceramic machining has been accomplished by both traditional (grinding, sawing etc) and non-traditional (laser, waterjet etc) methods.

1.2.1 Conventional Machining Techniques

Efforts have been made towards the development of machining, in particular grinding, technology for advanced ceramics in an efficient mode [5, 6]. High speed grinding has been studied for achieving a high removal rate in the machining of ceramics[6, 7]. In the high speed grinding process, an increasing wheel speed can reduce the maximum chip thickness, and thus the grinding force. This would promote ductile flow by reducing the tendency for brittle fracture [8]. On the other hand, the increased speed enables an increase in the wheel DOC or the workpiece feed rate to obtain a higher removal rate, without the deterioration of machined surface quality. Previous studies have been concerned with the high speed

grinding of advanced ceramics [9, 10]. For instance, Kovach et al.[10] carried out a feasibility study on the application of high wheel speeds in the low damage grinding of advanced ceramics, but the grinding was conducted at low efficiency modes. Hwang et al. [9, 11] systematically investigated the machining characteristics of silicon nitride under high speed grinding conditions. Their research focused on wheel wear mechanisms, again at low removal rates. Klocke et al. [7] studied various process strategies for the high speed grinding of aluminum oxide and silicon-infiltrated silicon carbide at high removal rates. The results indicated that the high speed grinding at high removal rates does not decrease the fracture strength of the machined ceramic components. However, in these works[7, 10], no detailed investigations of the effects of high speed grinding conditions on the material removal mechanisms and the surface integrity of advance ceramics have been reported.

Conventionally, machining of ceramics is accomplished through processes such as diamond machining and grinding which suffer from: 1) difficulties in obtaining complex contours; 2) low material removal rate; 3) excessive tool wear; and 4) high cost. Consequently non-traditional techniques such as water-jet and laser cutting have emerged as potential replacements for these diamond processes.

1.2.2 Non-conventional Machining

1.2.2.1 Laser Machining

In the past few decades, laser technology has also been successfully applied for the cutting of hard ceramic materials[3, 4, 12, 13]. During laser machining, the material separation may be accomplished through four different modes: vaporization; melt and blow; scribing; or thermal fracture [13]. The first two modes are energy intensive processes requiring power density in excess of 10^{10} W/m^2. These high-energy processes also induce residual stresses in the material (because of excessive thermal heating) affecting the strength of the finished product. Laser scribing followed by mechanical breaking is energy efficient but does not yield good finishing due to melting and resolidification of surface material.

Lumley [12] is one of the early researchers who proposed the thermal fracture mode of laser cutting ceramics due to its low energy requirement. Thermal gradients resulting from the absorption of light energy cause thermo-mechanical stresses sufficiently high to fracture the material. Tsai and Liou[4] have performed a number of experiments in thermal fracture mode of cutting in alumina using the CO_2 laser. Elperin et al.[14] proposed a thermal fracture model for scribing of glass and silicon wafers, wherein the wafer is heated by a laser beam and is immediately cooled by an air/water spray. Kondratenko [15] has patented the idea of cutting non-metallic materials by heating the substrate to temperatures below its softening point and cooling the heated zone subsequently to induce a blind crack. The blind crack then propagates to split the material apart. The effectiveness of this approach was demonstrated through experiments on Na-K glass. However, the patent did not discuss the type, flow, and pressure of coolant into the conventional laser cutting head. The patent was also limited to only glass materials.

The "Controlled thermal fracture mechanism" is an energy efficient process as low-powered lasers, operating below the melt/ablation threshold, are utilized for localized heating of workpiece and a gas stream is added for cooling the heated zone, leading to fracture of sample. Unfortunately, control of the fracture path necessitates use of slow feed rates (~ 5-30 mm/sec, see ref[4]). In order to improve the productivity, Segall and co-authors [16-18] have proposed a dual beam technique for cutting of ceramics where one beam causes pre-scoring of the workpiece surface while the other beam fractures the sample. The pre-score groove on the sample surface serves to guide the thermal stress-induced crack [17]. As compared to single-beam controlled fracture machining, dual beam machining produced a modest increase in the feed rate of alumina (~150%).

1.2.2.2 Waterjet Machining

Abrasive water-jet technologies have been utilized for cutting ceramic materials[19-22]. However, the use of high-pressure water (> 36,000 psi or 250 MPa) along with abrasives in water-jet requires special

pressure intensifiers and sapphire nozzles that are costly and have limited flow capacity. In addition, ceramic parts cut using abrasive water-jet exhibit large kerf width and poor surface roughness. Recently, Xu and Wang [22] have proposed controlled nozzle oscillation to improve the cut quality. However, the resulting improvements are only marginal and cut quality is still inferior to that obtained by conventional diamond machining.

But, contemporary non-traditional processes such as laser and water-jet which offer benefits over traditional processes for cutting these brittle materials also suffer from: high-power requirements (lasers ~ 2-10 kW, water-jet ~ 1 kilobar pressure), energy inefficiency, hazardous environment (laser and water-jet), abrasive requirements (water-jet), slow machining rates (water-jet), wear of machinery components (water-jet), etc. In this work, we address the issue of energy efficient and cost-effective machining of construction type of brittle materials at a rapid pace with the development of a novel hybrid Laser/Water-Jet (LWJ) manufacturing process.

1.3. Hybrid Machining Technique

Underlying hypothesis of the proposed hybrid laser/waterjet (LWJ) machining process is that elements of laser and water-jet machining can be synergistically combined such that material removal is accomplished by thermal shock assisted fracturing of material into fine fragments rather than energy-intensive erosive wear or melting and subsequent evaporation. The LWJ process (schematically shown in Figure 1.4) consists of a low-power laser for precise heating of a small processing zone on the work-piece. The laser heating will create temperature gradient in a zone approximately equal to thermal diffusion depth and rapid quenching of the zone by a low-pressure water-jet will cause development of thermal stresses that fracture this zone. The cycle of laser heating and water cooling will produce thermal shock, a phenomenon associated with rapid changes in the temperature generating internal thermal stresses and causing the brittle material to the extent of fracture. Thermal shock fracture is facilitated by low thermal

diffusivity, high thermal expansion coefficient, and low tensile strength. Thermal shock fracture caused by non-uniform thermal expansions/contractions, is a potential method of material removal in poor thermal conductive materials. Ashby's chart [37] of thermal shock resistance of all classes of materials, suggests that ceramics are highly susceptible to thermal shock fracture [1]. Rapid cooling rather than rapid heating will inflict the most of thermal shock since the induced surface stresses are tensile in nature during rapid cooling. The fractured debris will be washed away by the kinetic energy of the waterjet.

We have developed a novel manufacturing process that utilizes synergy of laser and water-jet for energy-efficient machining of brittle materials. Thermal shock induced non-uniform stress field and consequent fracture of material is identified as the key parameter affecting this synergy. Thus, this work explores the fundament phenomenological questions regarding the impact of thermal gradients and thermal shock-induced stress fields on controlled fracture of brittle materials as well as more practical issues related to machining of ceramics.

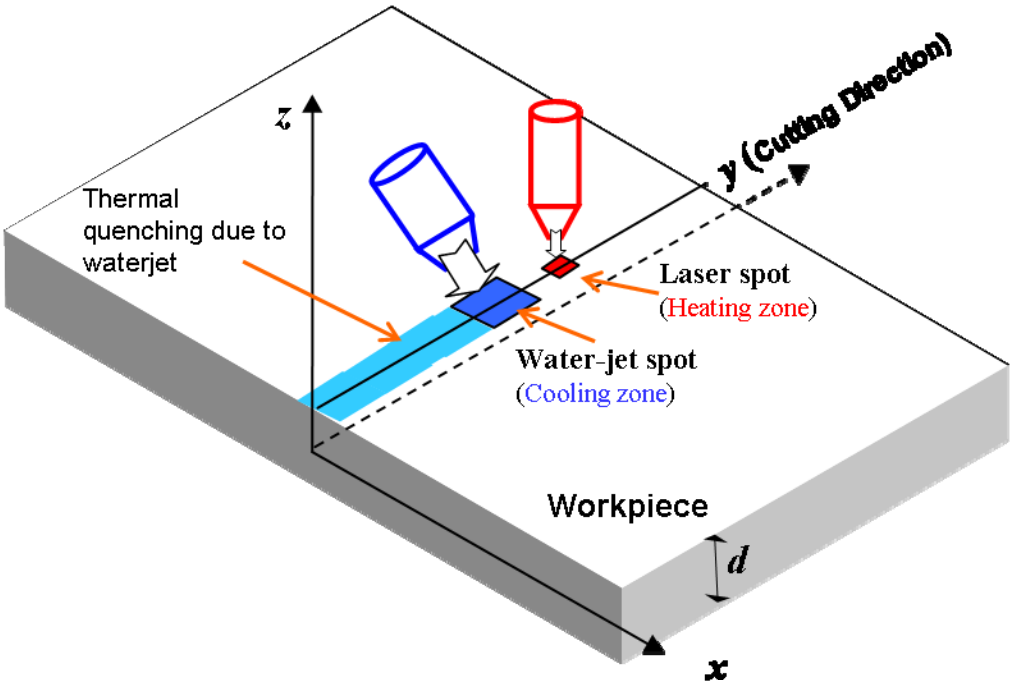

Figure 1.1: Schematic of the hybrid Laser/Waterjet process

Accordingly, the specific aims of the work were to:

1. Develop a mechanistic model for controlled fracture of brittle materials by thermal shock induced stress fields.
2. Build a laboratory scale implementation of the hybrid laser/waterjet system.
3. Explore the design space to identify the critical process parameters using the experimentally validated material removal model
4. Experimentally validate the model predictions using machining experiments on ceramics.

1.4.Ceramics considered for Machining

1.4.1 Alumina

Alumina or aluminum oxide is one of the most common and important industrial ceramics and finds application in various industries. It finds application as a substrate in electronics, as a sealing agent in the sanitary industry, as a insulation material in electrical engineering, as a wear resistant material in machine and plant construction, as a corrosion-resistant material in the chemical industry, as a protective tube for thermocouples used for high temperature measurements, and as a implant material in human medicine. Aluminum oxide is found in various grades such as 96% alumina and 99% alumina. The physical and mechanical properties are given in Table 1.1. Alumina has also been extensively experimented for machinability by thermal fracture[23-26].

Table 1.1: Properties of ceramics considered for machining

Material	Density (kg/m^3)	Thermal Conductivity (W/mK)	Specific Heat (J/kg K)	T. Expn Co-eff (1/K) X 1E-6	T. Diffusivity (m^2/s) X 1E-6	Young's Modulus (GPa)
Al_2O_3 (96%)	3290	24.7	880	8.00	8.53	344
AlN	3270	195	940	4.50	63.42	330
ZrO_2	6000	2	418	7.50	0.79	200
SiC	3200	160	920	4.00	54.32	410
Si_3N_4	3090	30	1000	3.30	9.71	310
BeO	2870	250	1250	9.00	69.71	380
BN	1920	161	1080	0.57	77.62	43

1.4.2 Zirconia

Zirconium oxide occurs as monoclinic, tetragonal and cubic crystal forms. Densely sintered parts can be manufactured as cubic and/or tetragonal crystal forms. In order to stabilise these crystal structures, stabilisers such as magnesium oxide (MgO), calcium oxide (CaO) or yttrium oxide (Y2O3) need to be added to the ZrO2. Other stabilisers sometimes used are cerium oxide (CeO2), scandium oxide (Sc2O3) or yttirium oxide (Yb2O3).

In fully stabilized zirconium oxide (FSZ – fully stabilized zirconia) the high-temperature cubic structure is preserved even after cooling due to the addition of the other oxides into the crystal structure. The increase in volume, undesirable for technical applications, does not take place in FSZ. Partially stabilized zirconium oxide (PSZ – partly stabilized zirconia) is of great technical significance. At room temperature, the substance includes a coarse cubic phase with tetragonal regions. This state can be retained in a metastable form through appropriate process control or annealing techniques. This prevents transformation of the tetragonal phase to the monoclinic phase, and the microstructure is "pre-stressed"; this is associated with an increase in strength and toughness.

In polycrystalline tetragonal zirconium oxide (TZP – tetragonal zirconia polycrystal) the use of extremely fine initial powders, and the application of low sintering temperatures, achieves an extremely fine-grained microstructure. Due to its extremely fine microstructure (grain size < 100 µm) and the metastable tetragonal structure, this material is characterised by extraordinary high mechanical strength, possibly even exceeding 1,500 MPa. The very finely developed tetragonal crystal phase in PSZ and in TZP displays a phenomenon unique to high-performance ceramics: transformation of the tetragonal phase into the monoclinic phase can be prevented by pressure. When the pressure is released, e.g. through crack tips or internal tensile stress, the transformation then occurs. The pressure-controlled increase in volume involved in the metamorphosis of the crystal phases closes cracks, slowing or deflecting their growth. This behaviour is exploited technically, and is known as transformation reinforcement. In PSZ ceramics, and in particular in TZP ceramics, it leads to extremely high component strength. Depending on the stabilisation method, it can be exploited at application temperatures between 600°C and 1,100°C. Zirconium oxide ceramics are therefore favoured for use in components that are subject to high mechanical stress. Due to its low thermal conductivity, the ceramic has higher machinability by thermal fracture but the cut quality may be affected due to its high fracture toughness.

1.4.3 Polycrystalline Cubic Boron Nitride

Cubic boron nitride (CBN) is the second hardest material on earth. It is advantageous over diamond, the first hardest material, in terms of greater thermal stability (high temperature) and chemical stability (less reactive to metals like iron and titanium). Due to its ultra-high hardness and high-temperature chemical stability, PCBN tool inserts are used for machining hard cast iron, high chrome alloy steels, high-strength nickel superalloys, powder metal alloys and metal matrix composites [27]. PCBN is available in two forms: one is in the form of thin layers backed on a cemented carbide substrate and the other is solid cylindrical compact produced by consolidation of boron nitride powders with binders at high pressures and temperatures. The binders infiltrated in PCBN are either metallic (cobalt) or ceramic (TiN and AlN).

Co and TiN-sintered PCBN cause the compacts to be electrically conductive, which allows convenient cutting of the blanks by EDM. However, a family of AlN-sintered PCBN blanks is electrically insulating and thus cannot be cut using EDM techniques. Waterjet cutting of blanks, a slow process, gives rise to wider kerf, poor surface finish and taper limiting the precision. Typically a Q-switched Nd:YAG laser in the fundamental mode is used to machine such PCBN blanks due to its excellent absorption characteristics [1]. However, this type of laser cutting removes the material through

There is considerable interest in investigating novel material removal methods and mechanisms to overcome the deficiencies of conventional laser cutting of PCBN. Hidai and Tokura [28] investigated the hydrothermal-reaction assisted laser drilling of PCBN in steam environment based on measurements of mass loss at high temperatures. CBN film deposited on copper substrate, binder-containing sintered PCBN, and binderless sintered PCBN were irradiated with an Ar-ion laser in water and steam as well as in different gas atmospheres. Single-crystal and binderless sintered CBN reacted very well with steam and thus hydrothermal-reaction-assisted laser machining was effective. However the technique failed in binder-containing sintered CBN. Hence the substrate is chosen for LWJ experimentation.

1.4.4 Polycrystalline Diamond

Polycrystalline diamond (PCD) is an excellent tool material as it incorporates high strength (~400 MPa), high hardness (~70 GPa), and high scratch and wear (~ 10 in Mohls scale). PCD has a typical mean particle size from 4 to 25 μm and a density of about 3560 to 4100 kg/m^3, depending on the particle size [1]. The orientation of the diamond grains is random and therefore the wear resistance is nearly equal in all directions. Cracks are likely to be discovered at grain boundaries producing local chipping but not complete failure [1]. PCD tools are widely used to machine engineering materials like ceramics, graphite epoxy composites, wood and plastics [29]. PCD micro tools are capable of achieving high machining rates along with producing finer surface finishes [29].

PCD is synthesised by sintering diamond powder at high pressure and high temperature [29] with a binder phase. Cobalt [30] is a commonly used binder while other binder phases such as nickel[2], magnesium carbonate [31, 32] are also used. Typically, PCD is stable up to about 700°C [1] and removing the metal binder will extend the stability up to 1200°C [1]. PCD composite tools are formed by depositing diamond layers on carbide substrates such as tungsten carbide. While PCD offers high wear resistance during machining, carbide substrates offer the required toughness making the composite tools an ideal choice for manufacturers. However, the material removal rate by EDG reported was very low (~ 9 mm^3/hr)[33]. Harrison *et al* [29] has investigated laser machining of PCD composite (thin layer of PCD on WC substrate) using Q-switched Nd:YAG laser at an average power of 420 W at repetition rates and pulse duration of 3-50 kHz and 20 to 200 ns respectively. The highest machining speed obtained was 36 mm/min. Hence, PCD is chosen for LWJ machining with an aim to improve cutting speed of the substrate.

1.5.Mathematical Model for fracture determination

A mathematical tool has been developed to obtain a relationship between the stresses associated with the laser heating and waterjet cooling and the fracture characteristics of the material/workpiece. The stresses are obtained from the temperature distribution by uncoupled quasi-static thermoelastic analysis [34]. Griffith Energy calculated from the stresses is compared to the fracture characteristics to determine material separation.

1.5.1 Temperature distribution

Green's function based approach is used to predict the temperature fields during laser and laser/water-jet machining. Temperature distribution, $T(x,y,z,t)$, in the workpiece is determined by modeling the laser and water-jet as rectangular source and sink [14], respectively as shown schematically in Figure 1.4 in order to simplify the analytical solutions. Transient temperature distribution are obtained by the solution of following diffusion equations

$$c_p \rho \frac{\partial T}{dt} = k\nabla^2 T + q\left(x, y, t, I_h, I_c\right) \qquad \text{Eqn (1)}$$

where c_p is the specific heat, ρ is the density of the material, T is the temperature field and $q(x, y, t, I_h, I_c)$ is the net heat input to the workpiece. The transient temperature distribution is determined using a Green's function approach

$$T(x,y,z,t) = \int_0^{\infty}\int_{-\infty}^{\infty}\int_0^{\infty} q\left(x_0, y_0 t_0, I_h, I_c\right)\theta\left(x, x_0, y, y_0, z, t, t_0\right) dy_0 . dx_0 . dt_0 + T_0 \qquad \text{Eqn (2)}$$

where $\theta\left(x, x_0, y, y_0, z, t, t_0\right)$ is the solution to the associated problem given by

$$c_p \rho \frac{\partial T}{dt} = k\nabla^2 T + \delta\left(x - x_0\right)\delta\left(y - y_0\right)\delta\left(z - \frac{d}{2}\right)\delta\left(t - t_0\right) \qquad \text{Eqn (3)}$$

where d is the thickness of the workpiece material, I_h is the laser heat intensity (W/m^2), and I_c is the cooling intensity (W/m^2) . To find solutions to the associated problem the following boundary conditions

are taken into account. Convective boundary conditions are used on the top surface where both laser heating and cooling takes place as well as on the workpiece edges (x = ± a and y = b). Insulated boundary conditions are assumed on the bottom surface (z = -d/2) and on the starting edge (y = 0). The solutions are detailed in the chapters to follow.

1.5.2 Stress distribution

Non-uniform heating and cooling of the specimen leads to development of thermal stresses in the specimen [34]. Uncoupled quasistatic thin plate analysis is used to determine the resulting thermal stress fields. Since the thickness of the wafer is thin in comparison to its length and width, we use a plane stress assumption in the mathematical model

$$\sigma_{zz} = 0 = \sigma_{xz} = \sigma_{yz} \qquad \text{Eqn (4)}$$

The inplane forces per unit length are N_x, N_y and N_{xy} and the equations of equilibrium that has to be satisfied are

$$\frac{\partial N_x}{\partial x} + \frac{\partial N_{xy}}{\partial y} = 0; \qquad \frac{\partial N_y}{\partial y} + \frac{\partial N_{xy}}{\partial x} = 0; \qquad \text{Eqn (5)}$$

We can find a stress function that can satisfy the following compatibility equation

$$N_x = \frac{\partial^2 T}{\partial y^2}; \; N_{xy} = -\frac{\partial^2 T}{\partial x \partial y}; \; N_y = \frac{\partial^2 T}{\partial x^2} \qquad \text{Eqn (6)}$$

Using the equation of compatibility, we can arrive at

$$\nabla^4 T = -\nabla^2 N_T \qquad \text{Eqn (7)}$$

Similarly the out-of-plane displacement, w can written as

$$D\nabla^4 w_d = -\frac{1}{1-\upsilon}\nabla^2 M_T \qquad \text{Eqn (8)}$$

The above equations could be easily solved if T and w_d could be represented by a series function as shown below

$$T(x,y) = \sum_{m=1}^{\infty}\sum_{n=1}^{\infty} T_{mn} cos\left(\frac{m\pi x}{2a'}\right) cos\left(\frac{n\pi y}{2b'}\right) \qquad \text{Eqn (9)}$$

Since the temperature T (from Eqn 3) is in the required mathematical form, the stress solution can be quickly obtained. The stress component (σ_{xx}) along the x axis that results in opening or closing of micro-cracks is given in Eqn (10). Similar analysis may be utilized to calculate the other components of stress.

$$\sigma_{xx} = \frac{1}{1-\upsilon}\left(-\alpha E T + \frac{1}{d}\left((1-\upsilon)N_x + N_T\right)\right) - \frac{12zD}{d^3}\left(\frac{\partial^2 w_d}{\partial x^2} + \frac{\partial^2 w_d}{\partial y^2}\right) \qquad \text{Eqn (10)}$$

where ν is Poisson's ratio, α is the coefficient of thermal expansion, E is the young's modulus, N_x is the in-plane force per unit length, D is bending rigidity of the plate per unit length, w_d is the out-of-plane displacement along z direction and N_T is calculated as:

$$w_d = \alpha E \frac{\omega_m^2 + \nu\xi_n^2}{\omega_m^2 + \xi_n^2} \int_{-d/2}^{d/2} z\, T dz \qquad \text{Eqn (11)}$$

$$N_x = -\alpha E \frac{\xi_n^2}{\omega_m^2 + \xi_n^2} \int_{-d/2}^{d/2} T dz \qquad \text{Eqn (12)}$$

$$N_T = \alpha E \int_{-d/2}^{d/2} T dz \qquad \text{Eqn (13)}$$

1.5.3 Griffith Energy Computation

The stress intensity factor K_I for Mode I crack loading can be determined from the stresses by using Bueckner's weight function method [35]. The weight functions for different crack lengths were computed using a finite element package, ABAQUS (Providence, RI). The channeling of an edge crack is a three dimensional process and for steady state crack extension, it is assumed that edge crack will channel at fixed depth, with a constant tip shape and constant release rate. Hence, driving force for a steady state crack growth is determined from average energy release rate over the depth of the channeling crack front [36]. The computed Griffith Energy is compared with materials critical energy for fracture.

$$G_t = \frac{1}{a}\int_0^a G_p(a')da' \qquad \text{Eqn (14)}$$

1.6.Preview of the chapters to follow

1.6.1 Chapter 2

Chapter 2 details the design of the laser/waterjet system for machining of the ceramics mentioned in Table 1.1. The system is designed for low and high thermal conductive materials. A validation experiment and cut quality analysis are performed on alumina ceramic to determine the effectiveness of the system.

1.6.2 Chapter 3

An important relationship between laser parameters and fracture characteristics are obtained in the LWJ machining of alumina. This graph would enable us to determine laser cutting parameters directly from stress intensity factors without performing experiments.

1.6.3 Chapter 4

The same mathematical model discussed previously is used to determine the laser cutting parameters from the fracture characteristics in the machining of zirconia. Experimental verification of the manipulated laser parameters is performed.

1.6.4 Chapter 5

Laser/Waterjet machining of high conductive and high strength polycrystalline diamond is discussed in this chapter. Additional stresses due to phase transformation of diamond to graphite helps in the material separation process.

1.6.5 Chapter 6

LWJ machining of polycrystalline cubic boron nitride is discussed in this chapter. PCBN, another high conductive ceramic undergoes material separation due to the additional transformation stresses taking place during oxidation.

1.6.6 Chapter 7

Future work of possible extension to other materials and profile cutting are discussed in the chapter.

1.7.References

[1] C. A. Harper, *Handbook of Ceramics, Glasses and Diamonds*: Mc Graw Hill, 2001.

[2] H. Huang and Y. C. Liu, "Experimental investigations of machining characteristics and removal mechanisms of advanced ceramics in high speed deep grinding," *International Journal of Machine Tools & Manufacture*, vol. 43, pp. 811-823, 2003.

[3] J. C. Rozzi, F. E. Pfefferkorn, Y. C. Shin, and F. P. Incropera, "Experimental evaluation of the laser assisted machining of silicon nitride ceramics," *Journal of Manufacturing Science and Engineering-Transactions of the Asme*, vol. 122, pp. 666-670, 2000.

[4] C. H. Tsai and C. S. Liou, "Fracture mechanism of laser cutting with controlled fracture," *Journal of Manufacturing Science and Engineering-Transactions of the Asme*, vol. 125, pp. 519-528, 2003.

[5] S. Agarwal and P. V. Rao, "Experimental investigation of surface/subsurface damage formation and material removal mechanisms in SiC grinding," *International Journal of Machine Tools & Manufacture*, vol. 48, pp. 698-710, 2008.

[6] V. E. Annamalai, T. Sornakumar, C. V. Gokularathnam, and R. Krishnamurthy, "Efficient Grinding of Ce-Tzp with Sic Wheels," *Journal of the European Ceramic Society*, vol. 11, pp. 463-469, 1993.

[7] S. Jahanmir, M. Ramulu, and P. Koshy, *Machining of Ceramics and Composites*. New york: Marcel Dekker, 1999.

[8] I. D. Marinescu, H. K. Haber, and I. Inaski, *Handbook of Ceramics Grinding and Polishing*. Park Ridge, New Jersey: Noyes Publications, 2000.

[9] T. W. Hwang, C. J. Evans, and S. Malkin, "An investigation of high speed grinding with electroplated diamond wheels," *Cirp Annals 2000: Manufacturing Technology*, pp. 245-248, 2000.

[10] J.A.Kovach, M.A.Laurich, S.Malkin, S.Srinivasan, B.Bandyopadhyay, and K.R.Ziegler, "A feasibility investigation of high-speed, low-damage grinding for advanced ceramics," presented at SME Fifth International Grinding Conference, 1993.

[11] T. W. Hwang, C. J. Evans, E. P. Whitenton, and S. Malkin, "High speed grinding of silicon nitride with electroplated diamond wheels, part 1: Wear and wheel life," *Journal of Manufacturing Science and Engineering-Transactions of the Asme*, vol. 122, pp. 32-41, 2000.

[12] R. M. Lumley, "Controlled Separation of Brittle Materials Using a Laser," *American Ceramic Society Bulletin*, vol. 48, pp. 850-&, 1969.

[13] W. Steen, *Laser Materials Processing*, 3rd Edition ed: Springer, 2003.

[14] T. Elperin and G. Rudin, "Controlled fracture of nonmetallic thin wafers using a laser thermal shock method," *Journal of Electronic Packaging*, vol. 126, pp. 142-147, 2004.

[15] V. S. Kondratenko, "Method of splitting Non-metallic materials," vol. United States Patent No: 5,609,204, 1977.

[16] R. Akapura, Li, B., and Segall, A.E., "A thermal stress failure model for laser cutting and forming operations," *Journal of Failure Analysis and Prevention*, vol. Vol 4, pp. 51-62, 2004.

[17] V. Pereles-Santiago, M. Washington, P. Brugan, G. Cai, R. Akarapu, S. Pulford, and A. E. Segall, "Faster and damage-reduced laser cutting of thick ceramics using a simultaneous prescore approach," *Journal of Laser Applications*, vol. 17, pp. 219-224, 2005.

[18] A. E. Segall, G. Cai, R. Akarapu, A. Romasco, and B. Q. Li, "Fracture control of unsupported ceramics during laser machining using a simultaneous prescore," *Journal of Laser Applications*, vol. 17, pp. 57-62, 2005.

[19] M. Hashish, Loscutoff, W.V., and Reich, P, "Cutting with Abrasive Waterjets," presented at Proceedings of the 2nd U.S. Water Jet Conference, WJTA, 1983.

[20] J. Wang, "Abrasive waterjet machining of polymer matrix composites - Cutting performance, erosive process and predictive models," *International Journal of Advanced Manufacturing Technology*, vol. 15, pp. 757-768, 1999.

[21] J. Wang and D. M. Guo, "The cutting performance in multipass abrasive waterjet machining of industrial ceramics," *Journal of Materials Processing Technology*, vol. 133, pp. 371-377, 2003.

[22] S. Xu and J. Wang, "A study of abrasive waterjet cutting of alumina ceramics with controlled nozzle oscillation," *International Journal of Advanced Manufacturing Technology*, vol. 27, pp. 693-702, 2006.

[23] C. Barnes, P. Shrotriya, and P. Molian, "Water-assisted laser thermal shock machining of alumina," *International Journal of Machine Tools & Manufacture*, vol. 47, pp. 1864-1874, 2007.

[24] P. Brugan, G. Cai, R. Akarapu, and A. E. Segall, "Controlled-fracture of prescored alumina ceramics using simultaneous CO2 lasers," *Journal of Laser Applications*, vol. 18, pp. 236-241, 2006.

[25] C. H. Tsai and C. J. Chen, "Formation of the breaking surface of alumina in laser cutting with a controlled fracture technique," *Proceedings of the Institution of Mechanical Engineers Part B-Journal of Engineering Manufacture*, vol. 217, pp. 489-497, 2003.

[26] A. N. Samant and N. B. Dahotre, "Computational predictions in single-dimensional laser machining of alumina," *International Journal of Machine Tools & Manufacture*, vol. 48, pp. 1345-1353, 2008.

[27] X. Ding, W. Y. H. Liew, and X. D. Liu, "Evaluation of machining performance of MMC with PCBN and PCD tools," *Wear*, vol. 259, pp. 1225-1234, 2005.

[28] H. Hidai and H. Tokura, "Hydrothermal-reaction-assisted laser machining of cubic boron nitride," *Journal of the American Ceramic Society*, vol. 89, pp. 1621-1623, 2006.

[29] P. M. Harrison, M. Henry, and M. Brownell, "Laser processing of polycrystalline diamond, tungsten carbide, and a related composite material," *Journal of Laser Applications*, vol. 18, pp. 117-126, 2006.

[30] H. Katzman and W. F. Libby, "Sintered Diamond Compacts with a Cobalt Binder," *Science*, vol. 172, pp. 1132-&, 1971.

[31] M. A. S. Y. Takashi Taniguchi, "Mechanical Properties of Polycrystalline Translucent Cubic Boron Nitride as Characterized by the Vickers Indentation Method," *Journal of the American Ceramic Society*, vol. 79, pp. 547-549, 1996.

[32] T. Irifune, A. Kurio, S. Sakamoto, T. Inoue, and H. Sumiya, "Materials - Ultrahard polycrystalline diamond from graphite," *Nature*, vol. 421, pp. 599-600, 2003.

[33] J. Y. Pei, C. N. Guo, and D. J. Hu, "Electrical discharge grinding of polycrystalline diamond," in *Advances in Materials Manufacturing Science and Technology*, vol. 471-472, *Materials Science Forum*, 2004, pp. 457-461.

[34] B. A. Boley, and Weiner,J.H.,, *Theory of Thermal Stresses*. Mineola, New York: Dover Publications, Inc., 1997.

[35] H. Tada, Paris, P.C., and Irwin, G.R., *Stress Analysis of Cracks Handbook*. St, Louis: Del Research, MI, 1985.

[36] L. G. Zhao, T. J. Lu, and N. A. Fleck, "Crack channelling and spalling in a plate due to thermal shock loading," *Journal of the Mechanics and Physics of Solids*, vol. 48, pp. 867-897, 2000.

[37] M. Ashby, F.,, *Materials Selection in Mechanical Design*. Oxford, England: Butterworth-Heinemann, 2001.

CHAPTER 2. DESIGN AND VALIDATION OF A HYBRID LASER/WATER-JET MACHINING SYSTEM FOR BRITTLE MATERIALS

(A paper published in Journal of Laser Applications, May 2008)

Dinesh Kalyanasundaram[1], Gamal Shehata, Clayton Neumann, Pranav Shrotriya and Pal Molian

Laboratory for Lasers, MEMS and Nanotechnology,

Department of Mechanical Engineering,

Iowa State University, Ames, IA 50011-2161

[1] Corresponding author: Email address - kdinesh@iastate.edu

2.1.Abstract

A unique laser/water-jet (LWJ) cutting head has been designed, built and interfaced with CO_2 laser for cutting and scribing of hard and brittle ceramic materials. Alumina samples were used to validate the effectiveness of the LWJ cutting head in thermal fracture mode. Results were compared with vaporization mode (focused beam) as well as thermal fracture mode (defocused beam) of air-assisted laser cutting. Thermal fracture mode in both LWJ and air-assisted laser cutting required three to five times less energy input for material separation than vaporization mode. However, the quality of the cut surfaces of LWJ was superior to both vaporization and thermal fracture modes of air-assisted laser cutting in terms of kerf, recast zone, density of micro-cracks, undercutting, and spatter. *The synergistic effects of laser and water-jet facilitated precise material separation and better cut quality through:* thermal shock-induced fracture mode of material separation rather than energy-intensive erosive wear (water-jet alone) or melting and subsequent evaporation (laser alone); and expulsion of cracked material with kinetic energy associated with the water-jet, leaving a clean cut surface.

Keywords: Hybrid machining, laser/water-jet, ceramic cutting, thermal fracture, alumina

Nomenclature :-

m_{zone} = mass of the laser irradiated zone in the specimen, kg

$\dot{q}_{zone}$ = Rate of heat absorption by the laser irradiated zone in the specimen, J/s

$\rho_{material}$ = density of the specimen material, kg/m^3

ρ_{water} = density of water, kg/m^3

d_{beam} = diameter of the laser beam on the surface of the specimen, m

T_s = temperature at the surface of the specimen, K

T_a = temperature of the surrounding environment, K

I = intensity of the laser beam, W/m^2

K = thermal conductivity of the specimen material, W/m K

κ = thermal diffusivity of the specimen material, m^2/s

t = interaction time of the laser at a point with the specimen, s

$C_{material}$ = specific heat capacity of the specimen material, J/kg K

$\dot{Q}_{water}$ = volume flow rate of the water required for cooling, m^3/s

C_{water} = specific heat capacity of the water, J/kg K

Δp = pressure differential across the inlet and outlet of the nozzle, Pa

C_d = coefficient of discharge of the nozzle, non-dimensional

$A_{orifice}$ = area of the orifice, m^2

Nu = Nusselt Number, non dimensional

Pr = Prandlt Number, non dimensional

2.2.Introduction

In this paper, we describe the design, fabrication and testing of a novel laser cutting head that utilizes synergistic combination of low-power laser (≤ 200W) beam and low-pressure water-jet (≤7 MPa or 1000 psi) for the cutting of 96% aluminum oxide (alumina). This work can be readily extended to other structural and electronic ceramics such as aluminum nitride, zirconium oxide, beryllium oxide, silicon carbide, and silicon nitride. Ceramics are widely used for a variety of applications ranging from microelectronics to prosthetics because of desirable properties such as: high hardness, low chemical reactivity, high volume receptivity at elevated temperatures, low density, low thermal conductivity, and ultra-fine finishing capability. Most of these applications require fast processing, tight dimensional tolerance and excellent surface integrity, therefore controlled processing and manufacturing becomes critically important. Conventionally, machining of ceramics is accomplished through processes such as diamond machining and grinding which suffer from: 1) difficulties in obtaining complex contours; 2) low material removal rate; 3) excessive tool wear; and 4) high cost. Consequently non-traditional techniques such as water-jet and laser cutting have emerged as potential replacements for these diamond processes.

Abrasive water-jet technologies have been utilized for cutting ceramic materials [1-3]. However, the use of high-pressure water (> 36,000 psi or 250 MPa) along with abrasives in water-jet requires special pressure intensifiers and sapphire nozzles that are costly and have limited flow capacity. In addition, ceramic parts cut using abrasive water-jet exhibit large kerf width and poor surface roughness. Recently, Xu and Wang [1] have proposed controlled nozzle oscillation to improve the cut quality. However, the resulting improvements are only marginal and cut quality is still inferior to that obtained by conventional diamond machining.

In the past few decades, laser technology has also been successfully applied for the cutting of hard ceramic materials [4-7]. During laser machining, the material separation may be accomplished through four different modes: vaporization; melt and blow; scribing; or thermal fracture [8]. The first two modes are energy intensive processes requiring power density in excess of 10^{10} W/m^2. These high-energy processes also induce residual stresses in the material (because of excessive thermal heating) affecting the

strength of the finished product. Laser scribing followed by mechanical breaking is energy efficient but does not yield good finishing due to melting and resolidification of surface material.

Lumley [5] is one of the early researchers who proposed the thermal fracture mode of laser cutting ceramics due to its low energy requirement. Thermal gradients resulting from the absorption of light energy cause thermo-mechanical stresses sufficiently high to fracture the material. Tsai and Liu [6] have performed a number of experiments in thermal fracture mode of cutting in alumina using the CO_2 laser. Elperin et al. [9] proposed a thermal fracture model for scribing of glass and silicon wafers, wherein the wafer is heated by a laser beam and is immediately cooled by an air/water spray. Kondratenko [10] has patented the idea of cutting non-metallic materials by heating the substrate to temperatures below its softening point and cooling the heated zone subsequently to induce a blind crack. The blind crack then propagates to split the material apart. The effectiveness of this approach was demonstrated through experiments on Na-K glass. However, the patent did not discuss the type, flow and pressure of coolant into the conventional laser cutting head. The patent was also limited to only glass materials.

The "Controlled thermal fracture mechanism" is an energy efficient process as low-powered lasers, operating below the melt/ablation threshold, are utilized for localized heating of workpiece and a gas stream is added for cooling the heated zone, leading to fracture of sample. Unfortunately, control of the fracture path necessitates use of slow feed rates (~ 5-30 mm/sec, see ref [6]). In order to improve the productivity, Segall and co-authors [11-13] have proposed a dual beam technique for cutting of ceramics where one beam causes pre-scoring of the workpiece surface while the other beam fractures the sample. The pre-score groove on the sample surface serves to guide the thermal stress-induced crack [11]. As compared to single-beam controlled fracture machining, dual beam machining produced a modest increase in the feed rate of alumina (~150%).

The objective of this work is to design a hybrid laser/water-jet (LWJ) cutting head that utilizes the thermal fracture mode concept for cutting of ceramics. A schematic representation of LWJ process is presented in Fig.2.1 which consists of precise heating of a small zone on the workpiece surface using a low-power laser, creating a temperature gradient in a zone approximately equal to thermal diffusion depth. The heated area tends to expand, but is restrained by the surrounding material, leading to

development of high compressive stresses acting on the heated area. Subsequent rapid quenching of the zone by a low-pressure water-jet causes the change in the state of stress from compression to tension. Rapid cooling rather than rapid heating will inflict most of thermal shock since the induced surface stresses are tensile in nature during rapid cooling. As a result of this, micro-cracks are formed at the top surface of material [9]. The fractured debris, if any, is washed away by the flow of water. Depending on the magnitude of the tensile forces created and the fracture toughness of the material, cracks created on top may extend and run through the thickness of material. Along the workpiece length, the cracks follow the laser-water jet path as the tensile stresses are created only in the path. Consequently, material separation will be accomplished through controlled propagation of cracks along the length of workpiece and resulting cut surfaces are expected to be free of thermal damage and residual stresses. In addition, the LWJ hybrid process avoids the formation of liquid and gaseous phases, making it more energy efficient and free from hazardous emission.

In short, the advantages of the thermal fracture process by LWJ process are: 1) the maximum temperature is significantly below the melting point; 2) cut surfaces are free of large visible defects – a property of great significance in electronics industry; and 3) the process is environmentally benign as there is near zero amount of material removal. 4) Small chips formed, if any, are washed away by the water-jet. Thus, controlled thermal fracturing obtainable through hybrid laser/water-jet can meet the challenges of higher feed rate, reduced energy and improved environment in the shaping of alumina.

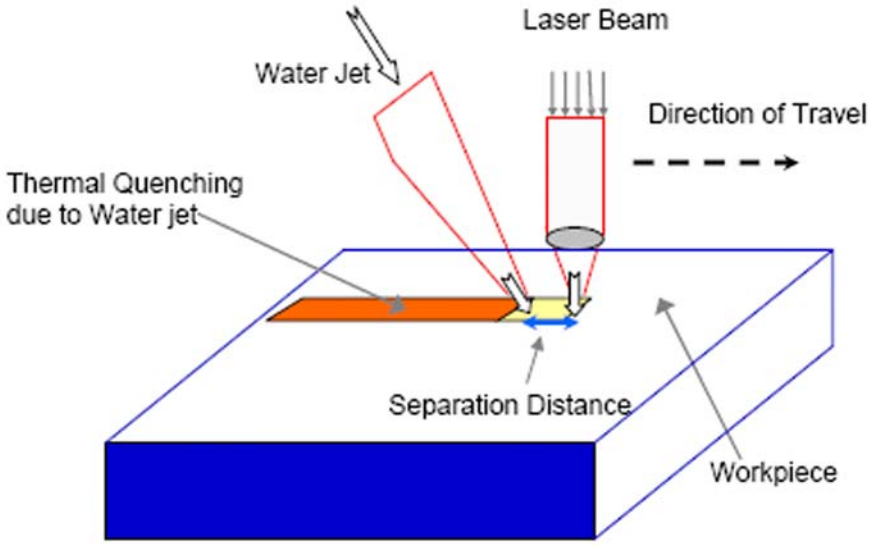

Figure 2.2.1: Schematic of Laser/Waterjet system

2.3.Prototype Design of LWJ Head

A unique LWJ cutting head was designed for interfacing with an existing 1.5 kW (maximum power) continuous wave CO_2 laser with an x-y computer numerical controlled (CNC) positioning table. The cutting head is expected to fulfill two functions: 1) allow the laser beam to focus on the workpiece with a shroud of assist gas as well as direct water-jet flow on the laser heated zone; and 2) accommodate the process requirement that the water-jet always trails the laser beam during cutting.

The first step in the design of the cutting head was to estimate water flow rate required for quenching the heated surface of ceramic materials considered: aluminum oxide (alumina), aluminum nitride, zirconium oxide, beryllium oxide, silicon carbide and silicon nitride. Thermal properties of the above-mentioned ceramics are listed in Table 2.1 [14]. During laser heating, the expected surface temperature (T_s) of ceramic work-piece is estimated assuming one-dimensional heat transport in a semi-infinite solid.

Table 2.2: Properties of different ceramics

Material	Density (kg/m^3)	Thermal Conductivity (W/mK)	Specific Heat (J/kg K)	T. Expn Co-eff (1/K) X 1E-6	T. Diffusivity (m^2/s) X 1E-6	Young's Modulus (GPa)
Al_2O_3 (96%)	3280	24.7	880	8.00	8.53	344
AlN	3270	195	940	4.50	63.42	330
ZrO_2	6000	2	418	7.50	0.79	200
SiC	3200	160	920	4.00	54.32	410
Si_3N_4	3090	30	1000	3.30	9.71	310
BeO	2870	250	1250	9.00	69.71	380
BN	1920	161	1080	0.57	77.62	43

$$T_s = T_a + \frac{2I}{K}\sqrt{\frac{\kappa t}{\pi}} \qquad \text{Eqn (1)}$$

Heat transfer calculations are performed to determine the flow rate required to cool workpiece surface from the heated temperature to room temperature within water-jet and sample interaction time [16]. Most commonly used water-jet orifices fall in the range of 0.125 mm (0.005") to 0.375 mm (0.015"). An orifice of diameter 0.33 mm (0.013") was chosen for the water-jet and pressure differential required to quench different ceramic materials are listed in Table 2.2.

As shown in the table 2.2, maximum pressure differential required to cool ceramic workpiece surface is only 1.69 MPa (241 psi). While it appears that relatively low pressures would be sufficient to produce the flow required, a high range of adjustability may be desired. To achieve this, a pump was selected that could produce a range of pressures, 0 to 21 MPa (3,000 psi), at the unusually low flow rates of this system. The pump selected to meet these criteria was a pneumatically powered pump (Rhino 3200D, Wilden Pump, Grand Terrace, CA).

Primary function requirement of the cutting head is to direct laser beam and water-jet on the workpiece surface. Laser beam and subsequently water-jet have to impinge on the same location to induce thermal stress fracture of the workpiece surface. Therefore, the head design should ensure that water-jet follows the same path as the laser beam to allow machining of straight as well as curvilinear profiles. In addition, system constraints that include compatibility of cutting head with existing laser machining system and large absorption of laser light by water (about 75% [17]), require that the head design should be compact, compatible to existing hardware and ensure little or no interaction between laser beam and water.

Table 2.3: Waterjet calculation for different ceramics

Material	heated mass (kg) x 1E-9	Temp rise (K) x 1E4	Heat Generated (W)	Covective co-efficient (W/m^2K) X 1E4	Nu	Velocity (m/s)	Pressure (N/m^2) X 1E5	Vol Flow rate Q (m^3/s) X 1E-6	Vol Flow rate Q (L/min)
Al_2O_3 (98%)	6.89	5.51	42.4	2.45	13.94	25.83	8.55	2.19	0.132
AlN	6.85	1.96	16.0	2.60	14.80	28.22	10.44	2.41	0.145
ZrO_2	12.62	22.41	149.0	2.12	12.08	20.29	5.36	1.74	0.104
SiC	6.70	2.25	17.6	2.49	14.17	26.33	9.02	2.25	0.135
Si_3N_4	6.47	5.04	41.4	2.61	14.88	28.46	10.53	2.43	0.146
BeO	6.01	1.73	16.5	3.04	17.27	36.10	16.91	3.09	0.185
BN	4.02	2.74	15.1	1.75	9.98	14.83	2.86	1.27	0.076

Second step was to design and fabricate a cutting head for the laser/water-jet system. The above-stated requirements and constraints may be satisfied by two different configurations: two independent heads for laser beam and water-jet or a single integrated head. First configuration is conceptually simple to design and fabricate but poses substantial challenges for satisfying the requirements of compactness and compatibility with existing hardware while ensuring that water-jet follows the laser beam. Therefore, second configuration of a single integrated head was pursued.

The design requirements were fulfilled by using a unique design for the cutting head assembly as shown in an exploded view (Fig 2.2(a)) and detailed sectional view (Fig 2.2(b)). Cutting head assembly consists of five components: fixed housing, bearing, rotating housing, orifice and nozzle as shown in the exploded view. The fixed housing is mounted on laser focusing hardware of an existing machining head. Nozzle and orifice are attached to the rotating housing and a roller bearing is positioned between the two housings such that the rotating housing can freely move with respect to the fixed housing.

The integrated head consists of non-interfering routes for the laser beam and water-jet as shown in Fig 2.2(b). Laser beam and assist gas are directed to workpiece surface through the central hole while the water flows from the inlet port (fixed) to the exit port (rotating) through two annular passages as shown in Fig 2.2(b). Annular passages and roller bearing allow the cutting head to rotate smoothly irrespective of water pressure and accomplish the design requirement that the water-jet follow the laser beam during cutting. The annular passages were sealed through the use of four neoprene o-rings. The water entering the cutting head from the pump travels through the two annular passages and then into

the orifice through vertical holes. The second annular passage prevents the threads on the water-jet tip from having to be indexed during manufacturing. The distance between the laser spot and the water-jet on the surface of the material can be varied by changing the orifice angle. Aluminum was selected as an appropriate material to fabricate the main unit due to its light weight, cost effectiveness, relative strength and the ease with which the design could be manufactured.

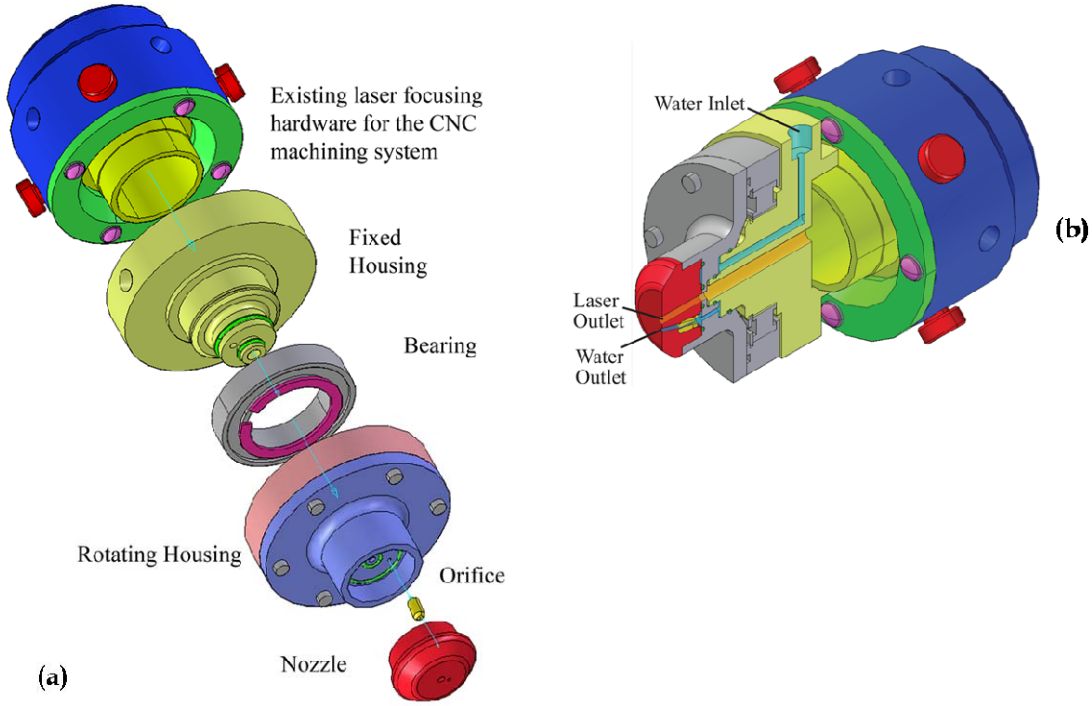

Figure 2.3.1 (a) Exploded view of Laser/Waterjet head (b) Cut section of the head

A photograph of the completed design is shown in Fig 2.3. The bottom portion of the head is fabricated from brass and its photograph that indicates the laser and water passages is shown in the inset of Fig 2.3. As shown in Fig 2.3, the rotating housing is machined with grooves on its circumference to assist in interfacing of laser cutting head to third axis of CNC positioning table through a belt and pulley system. Numerical control of cutting head rotation will facilitate material separation along curved profiles.

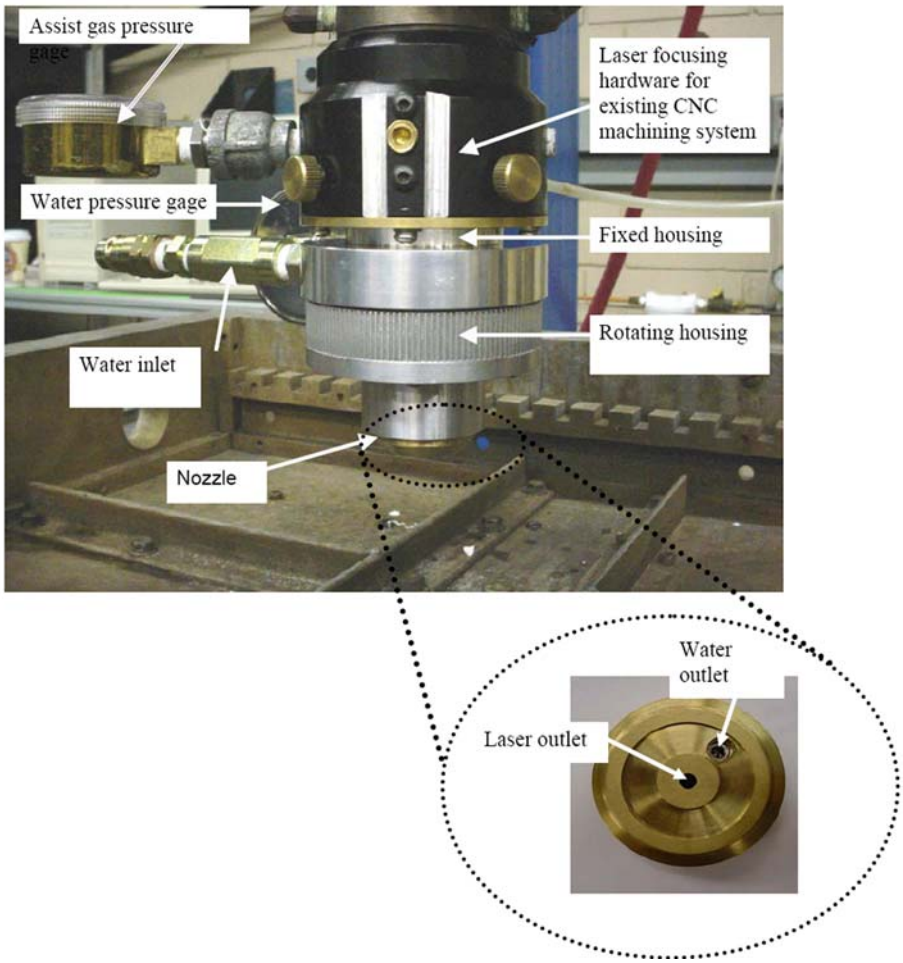

Figure 2.3.2: Assembled Laser/Waterjet head

2.4.LWJ Experiments of Cutting Alumina

Experiments were conducted to study the effectiveness of the LWJ system. Alumina (96%) was selected for these experiments as it finds many applications in microelectronic circuits and in structural components for aircraft, spacecraft, and automotives. Further, it is an excellent substrate material for laser processing and substantial literature could be easily located on laser processing of alumina [6,7].

LWJ cutting head was interfaced with the existing CNC controlled laser machining system. Cutting experiments were carried out on 96% alumina sample with a thickness of 1 mm (0.04″). In the first step, as-received 102 mm x 102 mm (4″ x 4″) alumina samples were cut into 25 mm x 25 mm (1″ x 1″) samples and the edges were then ground. The alumina samples were cut along the centerline to separate it into two parts for the validation experiments.

Initial experiments with air-cooling were carried out to find out the appropriate parameter range that would cause thermal fracture. The effects of the following parameters are studied: power, velocity, spot size and air-pressure.. The parametric study was undertaken by varying the laser power from 100 W to 200 W and cutting speed from 8 mm/sec to 76 mm/sec. and spot size from 0.2 mm diameter to 1 mm diameter. The effect of air pressure was studied for two extreme limits (60 kPa (5 psi) and 207 kPa (30 psi)) one being the minimal pressure needed to protect the laser lens from metallic and non-metallic vapors due to heating and the other being the maximum pressure that can be handled by the laser head nozzle without damage to the equipment.

Air-cooled thermal fracture results are used to decide the cutting parameter matrix for LWJ experiments. LWJ cutting experiments were carried out for one spot size,while the laser power was varied from 100 W to 200 W and cutting speed was varied from 8 mm/sec to 76 mm/sec. The water pressure is varied from 60 psi (414 kPa) to 6.30 MPa (900 psi).

For the vaporization mode of material separation laser beam was focused on the surface using a 127-mm focal length lens to a spot diameter of 0.2 mm. After each cutting test, the sample surface was carefully examined and then grouped into three different categories: scribed, material separation, and uncontrolled fracture. Sample surfaces obtained from each mode are compared to evaluate the cut quality.

2.5.Experimental Results and Discussion

Experimental observations for all three cutting modes are plotted in terms of line energy, which is a combination of processing parameters (ratio of power (P) to velocity (v)**)**. Line energy clearly distinguishes between different fracture characteristics obtained for the three different modes of cutting. As a representative example, sample fracture characteristics obtained for air-cooling under different powers and velocities are plotted in Fig 2.4(a). The plotted data was collected for a single spot size (0.4 mm) and two different air pressures. It can be inferred from the graph that for a constant velocity there is a transition from scribing to cutting as the power increases and this trend shifts proportionally at different velocities. Therefore the ratio of power (P) to velocity (v) can be considered to be a single fracture controlling parameter rather than two independent parameters. This ratio is termed as line

energy and has the units J/mm. Similar observations of transition from scribing to material separation were observed for LWJ and vaporization mode of cutting as well.

The focus of this paper is to investigate thermal fracture mode of material separation therefore, effect of spot size and coolant pressure on material separation obtained using air cooling and water-jet quenching are discussed first. In the later part, line energy requirements and cut surface quality are compared for the three modes of laser cutting.

2.5.1 Thermal Fracture mode by air cooling

Effect of Spot Size:

Fracture characteristics obtained for different spot sizes as function of line energy are plotted in Fig 2.4(b). As the spot size is increased, the transition from scribing to controlled fracture occurs at lower values of line energy. Similar observations of controlled cracking for defocused beams at larger spot sizes have been reported by Tsai and Liou [6]. The workpiece is more prone to damage for focused beams and uncontrolled fracture of the workpiece results while using focused beam of spot size diameter 0.2 mm.

Effect of air pressure:

Two different air-pressures were used for air-cooling. It was found that the increase of air-pressure from 69 kPa (10 psi) to 207 kPa (30 psi) had minimal effect on the fracture conditions as shown in Fig 2.4(a).

2.5.2 Thermal fracture mode by LWJ

A spot size of 0.6 mm was chosen for LWJ cutting as this spot size resulted in a clear transition from scribing to controlled fracture for air cooling in the parameter range investigated (Fig 2.4(b)). In addition, the spot size of 0.6 mm ensures minimum interaction between laser beam and water-jet.

Effect of water pressure:

Fracture characteristics obtained for different water pressures as a function of line energy are plotted in Fig 2.4(c). For a fixed orifice diameter, increase in water pressure results in increased flow rate and correspondingly in higher convective heat transfer coefficients. Due to increased heat transfer at the

surface, transition from scribing to controlled fracture is observed only at higher line energy with increase of coolant pressure.

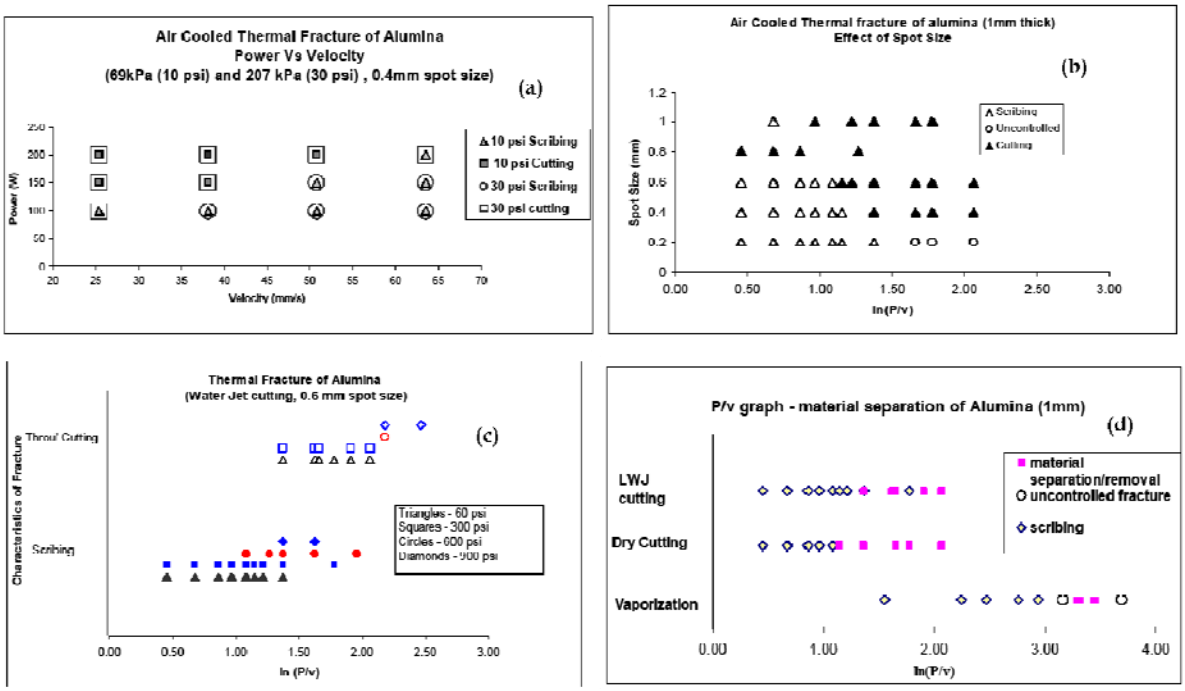

Figure 2.5.1 (a): Power vs velocity in air cooled thermal fracture (b) Effect of spot size in air cooled thermal fracture (c): Characteristics of cutting as a function of line energy for LWJ (d): Comparison of different laser cutting methods as a function of line energy

2.5.3 Comparison of Line energy for different modes of cutting

The line energy requirement for the three different modes of cutting namely vaporization, thermal fracture by air-cooling and thermal fracture by LWJ is plotted in Fig 2.4 (d). Vaporization mode requires the largest amount of energy input leading to *P/v* requirement of about 27-32 J/mm for material separation. In contrast, *P/v* requirement for controlled thermal fracture using air cooling (dry laser cutting) and water quenching (laser-water jet) are about three to five times less as compared to vaporization mode. There is a slight increase in energy requirements for thermal fracture in water quenching as compared to air cooling. Experimental results clearly indicate that the synergistic combination of laser heating and water-jet quenching led to efficient material separation through crack propagation as compared to conventional vaporization mode.

2.5.4 Comparison of Cut quality for different modes of material separation

(a) Vaporization mode:

Scanning electron microscope (SEM) images of cut surfaces were analyzed in order to evaluate the cut quality obtained for the three different modes of material separation. SEM images of the cut surface obtained for vaporization mode, thermal fracture by air cooling and thermal fracture by water quenching are presented in Fig 2.5(a), (b) and (c), respectively. For the vaporization mode in the Fig 2.5(a), a completely recast zone is seen across the whole cut surface and there is large dross attached to sample at the lower surface. The recast layer has a large number of micro-cracks which are expected to reduce the strength of cut specimen and may lead to uncontrolled fracture of specimen during machining and subsequent part handling [18].

(b) Thermal fracture by air-cooling:

For thermal fracture caused by air cooling as shown in Fig 2.5(b), there are two distinct regions similar to those reported by Tsai and Liou [6]. The cut surface exhibits clean fracture with a thin undercut region of about 200 μm close to the top surface. Groove near the top surface is caused by the material vaporization during laser heating and may be termed as undercutting. Undercut region also has number of micro-cracks while the fracture surface is free of any cracks. Since the undercut region is only a small proportion of the cut surface, the separated surfaces are expected to have minimal residual thermal stresses compared to the conventional vaporization mode of material separation.

(c) Thermal fracture by LWJ:

For thermal fracture caused by water quenching shown in Fig 2.5(c), the cut surface shows a clean fracture with no recast zone or undercut zone. Cut surface is free of any micro-cracks and consequently, specimen strength will not be compromised by the cutting process [18]. The dark areas in the Fig 2.5(c) are due to contamination of cut surfaces by minerals found in water. A chemical analysis of the contaminated and the uncontaminated areas was performed to identify the effect of water quality used during the cutting processes. The uncontaminated region shows mostly aluminum and oxygen, the primary constituents of alumina. The contaminated region shows potassium, calcium, sodium, chlorine –

the basic constituents of minerals found in tap water used in the water-jet during the current experiments. Use of pure water may alleviate the contamination problem for sensitive applications.

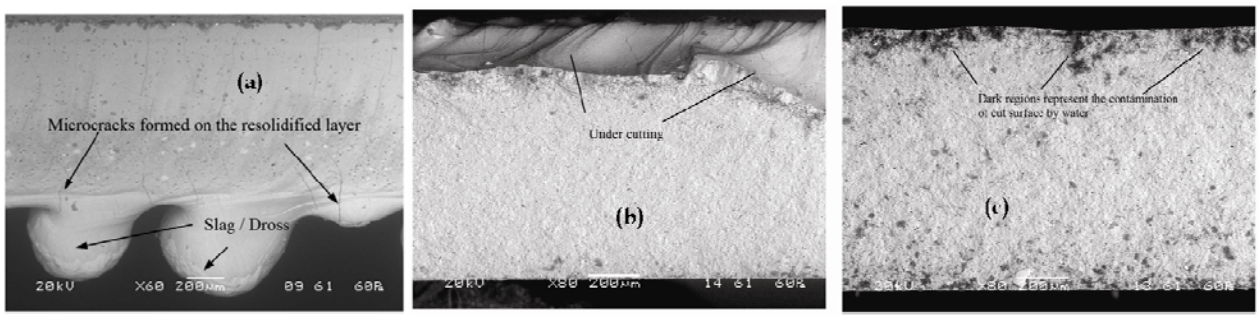

Figure 2.5.2 Cut cross-section in (a) melt & blow cutting (b): Air cooled thermal fracture (c): Laser/Waterjet cutting

Kerf widths for the two thermal fracture modes were also determined to compare the cut-quality obtained from each process. SEM images of the specimen surfaces cut using thermal fracture mode due to air cooling and water-quenching are presented in Fig 2.6(a) and (b), respectively. In air-cooled thermal fracture mode, a large kerf width is seen. In both cases of thermal fracture, crack path on the top surface is surrounded by a heat affected zone (HAZ). The HAZ zone is about 600 μm for air-cooled thermal fracture while it is only about 100-200 μm for water-quenched thermal fracture (LWJ).

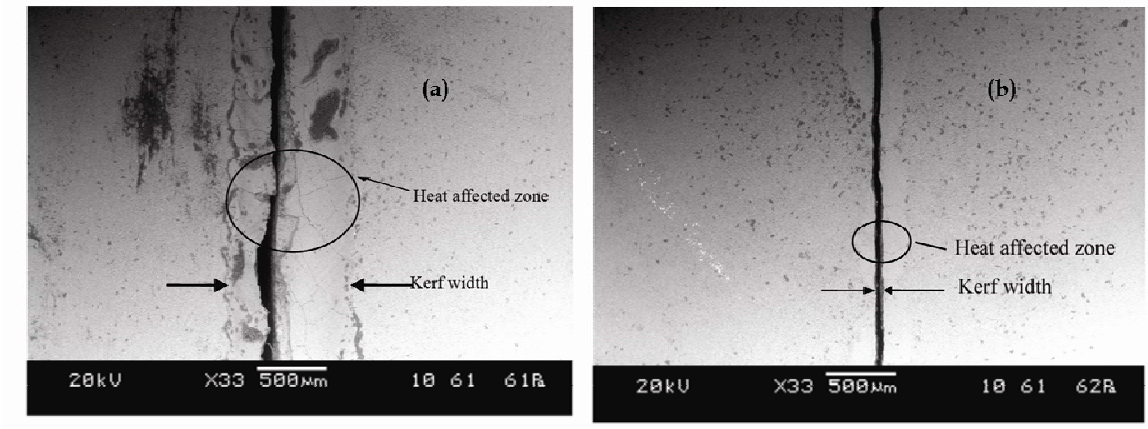

Figure 2.5.3 (a) Top view of the cut path in air cooled thermal fracture and (b): in LWJ cutting

In both cases of thermal fracture mode of cutting, there was not any significant improvement in the cut quality for increase in air pressure or water-jet pressure but in LWJ, higher water pressures resulted in higher power consumption and did prevent uncontrolled fracture.

In the case of abrasive water-jet cutting [1, 19], kerf width is very large (approximately 1300 μm, calculated from the figure shown in [19]) and cut surfaces are uneven. Conventional grinding processes lead to sub-surface damages due to grain dislodgement and action of shear forces [20]. Using laser alone for material separation through either vaporization or air-quenched thermal fracture leads to significant HAZ, residual thermal stresses and micro-cracks on the cut surfaces. In contrast, LWJ results in efficient material separation with small kerf widths and cut surfaces that are free of residual thermal stresses and micro-cracks. Experimental results presented in this study clearly demonstrate the advantages of hybrid laser/water-jet method over laser-alone and water-jet alone for machining ceramics.

2.6.Conclusions

A laser-water jet cutting head was designed, fabricated and integrated with an existing CNC laser system for machining hard and brittle materials such as ceramics. Cutting experiments were conducted on alumina to demonstrate the effectiveness of LWJ cutting head. Experimental results showed that laser/water-jet machining utilized the synergistic effects of laser and water-jet for material separation through controlled thermal fracture and required three to five times less energy input than conventional vaporization mode but in comparison to air cooled thermal fracture mode, LWJ material separation required more energy input. The quality of the cut surface was better in LWJ than those obtained from the conventional laser vaporization mode and air cooled thermal fracture mode of material separation in terms of kerf, recast zone, under-cutting, and presence of micro-cracks.

Acknowledgements

The authors gratefully acknowledge the financial support for this research provided by the U.S. National Science Foundation under the Grant # DMI-0522788. Any Opinions, findings and conclusions or recommendations expressed in this material are those of the author(s) and do not necessarily reflect those of the National Science Foundation.

2.7.REFERENCES

1. Xu, S., Wang, J., "A study of abrasive waterjet cutting of alumina ceramics with controlled nozzle oscillation", International Journal of Advanced Manufacturing Technology, 2006, Vol 27, pg: 693-702.
2. Wang, J., "Abrasive waterjet machining of polymer matrix composites cutting performance, erosive analysis and predictive models", International Journal of Advanced Manufacturing Technology, 1999, Vol 15, pg: 757-768.
3. Hashish, M., Loscutoff, W.V., and Reich, P., Cutting with Abrasive Waterjets", Proceedings of the 2nd U.S. Water Jet Conference, WJTA, 1983, 417.
4. Rozzi, J.C., Pfefferkorn, F.E., Shin, Y.C., Incropera, F.P., " Experimental Evaluation of the Laser Assisted Machining of Silicon Nitride Ceramics", Journal of Manufacturing Science and Engineering, 2000, Vol 122, pg: 666-670.
5. Lumley, R.M., "Controlled Separation of Brittle Materials Using a Laser," American Ceramic Society Bulletin, 1969, Vol 48, pg: 850-854.
6. Tsai, C.H., and Liou, C.S., "Fracture Mechanism of Laser Cutting with Controlled Fracture", Journal of Manufacturing Science and Engineering, 2003, August, Vol 125, pg: 519-528.
7. Tsai, C. H., and Liou, C. S., ''Apply On-line Crack Detection Technique to Laser Cutting with Controlled Fracture,'' International Journal of Advanced Manufacturing Technology, 2001, Vol 18, pg. 724–730
8. William Steen, "Laser Materials Processing", 2003, 3rd Edition, London ; New York : Springer, pg: 72-85
9. Elperin, T., Kornilov, A., "Formation of Surface Micro crack for separation of Nonmetallic wafers into chips", Journal of Electronic Packaging, Dec 2000, Vol 122, pg: 317-322.
10. Kondratenko, V.S., "Method of splitting Non-metallic materials", March 1977, United States Patent No: 5,609,204.

11. Pereles-Santiago, V., Washington, M., Brugan, P., Cai, G., Akarapu, R., Pullford, S. and Segall, A. E., " Faster and damage – reduced Laser cutting of Thick Ceramics Using a Simultaneous Prescore Approach", Journal of Laser Applications, 2005, Vol 17 (4), pg: 219-224.

12. Segall, A.E., Cai, G., Akapura, R., Romasco, A., and Li., B, "Fracture control of unsupported ceramics during laser machining using a simultaneous score", Journal of Laser Applications, 2005, Vol 17(1), pg 57-62.

13. Akapura, R., Li, B., and Segall, A.E., "A thermal stress failure model for laser cutting and forming operations, Journal of Failure Analysis and Prevention, 2004, Vol 4, pg: 51-62.

14. Harper, C.A., "Handbook of Ceramics, Glasses and Diamonds", Mc Graw Hill, 2001.

15. Carslaw, H.S., and Jaeger, J.C., "Conduction of heat in Solids", 2nd Edition, Oxford University Press, 1980.

16. Incropera, F.P., and DeWitt, D.P., "Introduction to heat transfer", 3rd Edition, John Wiley & Sons, 1996.

17. Payne, B.P., Nishioka, N.S., Mikic, B.B., Venugopalan, V., "Comparison of pulsed CO_2 ablation at 10.6 μm and 9.5 μm", Lasers in Surgery and Medicine, 1998, Vol 23, pg: 1-6.

18. Shehata, G., Molian, P.A., Bastawros, A., and Shrotriya, P., " Surface finish and flexural strength of CO_2 laser-cut alumina by evaporative and thermal stress fracture modes, To be published in Proceedings of NAMRC 35, Society of Manufacturing Engineers, MI, 2007

19. Wang,J., Guo, D.M., "The cutting performance in multi-pass abrasive water-jet machining of industrial ceramics", Journal of Material Processing Technology, 2003, Vol 133, pg: 371-377.

20. Huang, H., Liu, Y.C., " Experimental investigations of machining characteristics and removal mechanisms of advanced ceramics in high speed deep grinding", International Journal of Machine Tools & Manufacture, 2003, Vol 43, pg: 811-823.

CHAPTER 3. OBTAINING A RELATIONSHIP BETWEEN PROCESS PARAMETERS AND FRACTURE CHARACTERISTICS FOR HYBRID CO2 LASER/WATERJET (LWJ) MACHINING OF CERAMICS

(A paper accepted for publication in Transactions of ASME Journal of Engineering Materials and Technology)

Dinesh Kalyanasundaram[1], Pranav Shrotriya[*], and Pal Molian
[*]**Binger Assistant Professor of Mechanical Engineering**

Laboratory for Lasers, MEMS, and Nanotechnology
Department of Mechanical Engineering
Iowa State University, Ames, IA 50014

3.1.Abstract

A combined experimental and analytical approach is undertaken to identify the relationship between process parameters and fracture behavior in the cutting of 1 mm thick alumina samples by a hybrid CO_2 Laser/WaterJet (LWJ) manufacturing process. In LWJ machining, a 200W power laser was used for local heating followed by waterjet quenching of the sample surface leading to thermal shock fracture in the heated zone. Experimental results indicate three characteristic fracture response: scribing, controlled separation, and uncontrolled fracture. A Green's function based approach is used to develop an analytical solution for temperatures and stress fields generated in the workpiece during laser heating and subsequent waterjet quenching along the machining path. Temperature distribution was experimentally measured using thermocouples and compared with analytical predictions in order to validate the model assumptions. Computed thermal stress fields are utilized to determine stress intensity factor and energy release rate for different configuration of cracks that caused scribing or separation of the workpiece. Calculated crack driving forces are compared to fracture toughness and critical energy release rates to predict: the equilibrium crack length for scribed samples; and the process parameters associated with transition from scribing to separation. Both of these predictions are in good agreement with experimental observations. An empirical parameter is developed to identify the transition from controlled separation to uncontrolled cracking because the equilibrium crack length based analysis is unable to predict this transition. Finally, the analytical model and empirical parameter are utilized to create a map that relates the process parameters to fracture behavior of alumina samples.

Keywords:

CO2 Laser/Waterjet (LWJ) machining, thermal shock, alumina, fracture, crack propagation, ceramic

[1] *Corresponding author: kdinesh@iastate.edu*

3.2.Introduction

Structural ceramics such as alumina (aluminum oxide) are widely used for a variety of applications ranging from microelectronics to prosthetics because of desirable properties such as: high hardness, low chemical reactivity, high volume receptivity at elevated temperatures, low density, low thermal conductivity, and ultra-fine finishing capability. Traditional cutting methods for structural ceramics are limited by their brittleness, high hardness and low thermal expansion, leading to: increased vulnerability to workpiece fracture; significance loss of workpiece material; tool failure; difficulty in achieving the design requirements of high precision and excellent surface integrity; and need for regular maintenance due to wear [1-7].

It is crucial to develop novel machining processes that can fabricate ceramic parts at a relativity high rate, while eliminating the fractures and breakages associated with current manufacturing methods [2, 3]. CO_2 laser cutting is an accepted industrial technique for producing useful shapes in ceramics such as alumina due to its localized heating effect and non-contact nature over mechanical methods. However, it does not necessarily preclude damage and/or fracture of the workpiece due to uncontrolled cracking.

CO_2 laser cutting of ceramics can be accomplished by three different methods: 1) melting and evaporation where the melt layer is blown off by a high-pressure (80 to 90 psi) gas stream; 2) partial evaporation to form a deep groove followed by applying a mechanical force or ultrasonic energy to break the material; and 3) controlled thermal stress fracture where the laser energy produces thermal stress causing the material separation similar to a crack extension. The evaporation/melting mode of material removal requires extreme power lasers (> 500 W), leading to collateral thermal damages such as residual stresses, heat affected zone, recast layer, uncontrolled fracture etc [5, 7, 8]. Mechanical score and snap methods also result in surface damage such as micro-cracks and residual stress etc. In contrast, controlled thermal stress fracture mode of material removal can be achieved at low powers (15-20 W) but suffers from slowness and narrow range of process parameters.

Thermal shock fracture of brittle materials has been investigated for the last few decades. Lumley [9] was one of the earliest researcher to demonstrate controlled thermal fracture of glass specimens using lasers. Controlled thermal shock fracture mechanism is an energy efficient process as low-powered lasers operating below the melt/ablation threshold are utilized for localized heating of workpiece and a gas stream is added for cooling the heated zone, leading to fracture of sample. Tsai and co-workers [10, 11] have demonstrated thermal shock fracture mode for cutting alumina substrates. It was also observed that larger spot sizes helps in the increase of cutting speed as well as cut quality over traditional machining processes. Unfortunately, control of the fracture path necessitates use of slow feed rates (~ 5-10 mm/sec) (see refs [10, 11]). In addition, the scattering errors associated with the process often promote uncontrolled crack propagation. Segall and co-workers have reported a dual-beam laser cutting process where one beam causes pre-scoring of the workpiece surface while the other beam fractures the sample [12]. Pre-score groove on the sample surface serves to guide thermal stress-induced crack. As compared to single beam controlled fracture machining, dual-beam machining produced a modest increase in the feed rate in the cutting of alumina (~150%) [12].

Previous analysis of alumina fracture during laser cutting have primarily relied on finite element analysis for prediction of thermal stresses [10, 13-15] and localized melting in the workpiece has been modeled through removal of nodes in the region where the temperature exceeded the alumina melting temperature [13, 15]. Experimental observations of workpiece fracture is explained either by comparing the computed maximum tensile stress to alumina strength [10, 13, 14] or through empirical probabilistic measures based on computed stress fields [15]. These approaches are primarily suitable for analysis of experimental observations and may not be suitable for identifying processing conditions for controlled cutting of alumina workpiece.

A combined experimental and computational approach is utilized to analyze crack propagation in alumina workpiece during Laser/Waterjet (LWJ) machining. A novel approach of combining laser and waterjet (LWJ) (see Fig 3.1) was developed and proof-of-concept studies on cut quality and energy efficiency in machining alumina were reported in our previous publications [5, 7]. The laser heating

creates temperature gradient in a zone approximately equal to thermal diffusion depth and rapid quenching of that zone by the waterjet develops thermal stresses that fracture this zone. As a result, LWJ machining allows higher feed rates and cleaner cuts. In addition, it avoids the formation of liquid and gaseous phases, making the cutting process more energy efficient and free from hazardous emission.

In this work, cutting experiments are conducted to identify typical process parameters that correspond to scribing, controlled separation, and uncontrolled fracture of the workpiece. An analytical model is developed for determining the transient temperature and stress distribution during laser heating and subsequent water-jet quenching. Measured thermal histories of samples during LWJ cutting are compared with model predictions to validate the thermal analysis and modeling assumptions. Experimentally validated model is used to compute driving forces for two different crack configurations : (i) plane strain crack: a single dominant crack aligned with the through-thickness direction [16] and (ii) channeling: crack aligned along the cutting direction [17, 18]. Crack driving forces are compared to fracture toughness of alumina to obtain a relationship between process parameters and workpiece fracture characteristics.

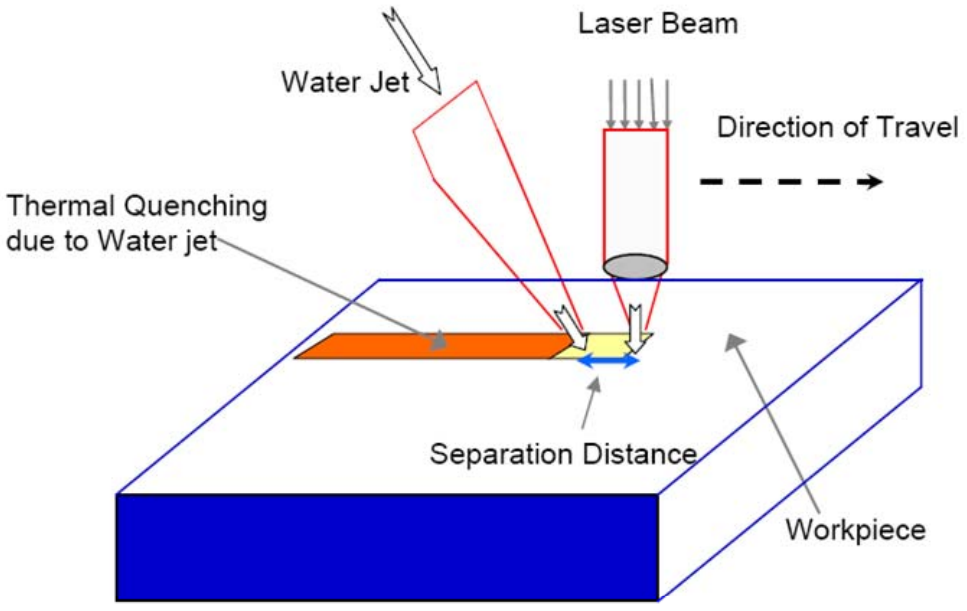

Fig 3.1: Schematic representation of Laser/Waterjet system

3.3.Experimental Procedure

Square plates of 96% alumina that were 100 mm X 100 mm X 1 mm in dimensions were purchased from Coorstek, (Golden, CO, USA) and samples of 25 mm X 25 mm were prepared for LWJ cutting experiments. Two different experiments are performed on alumina samples: first set of experiments were used to determine the processing parameters that correspond to controlled separation and second set of experiments were used to record temperature history of specimens during laser water-jet machining. A simple fixture was fabricated to hold the samples such that the area directly below the cutting path is not in contact with metallic surfaces to minimize heat transfer at the bottom surface (Fig 3.2). The details of the hybrid laser water-jet cutting system are described in a previous publication [5].

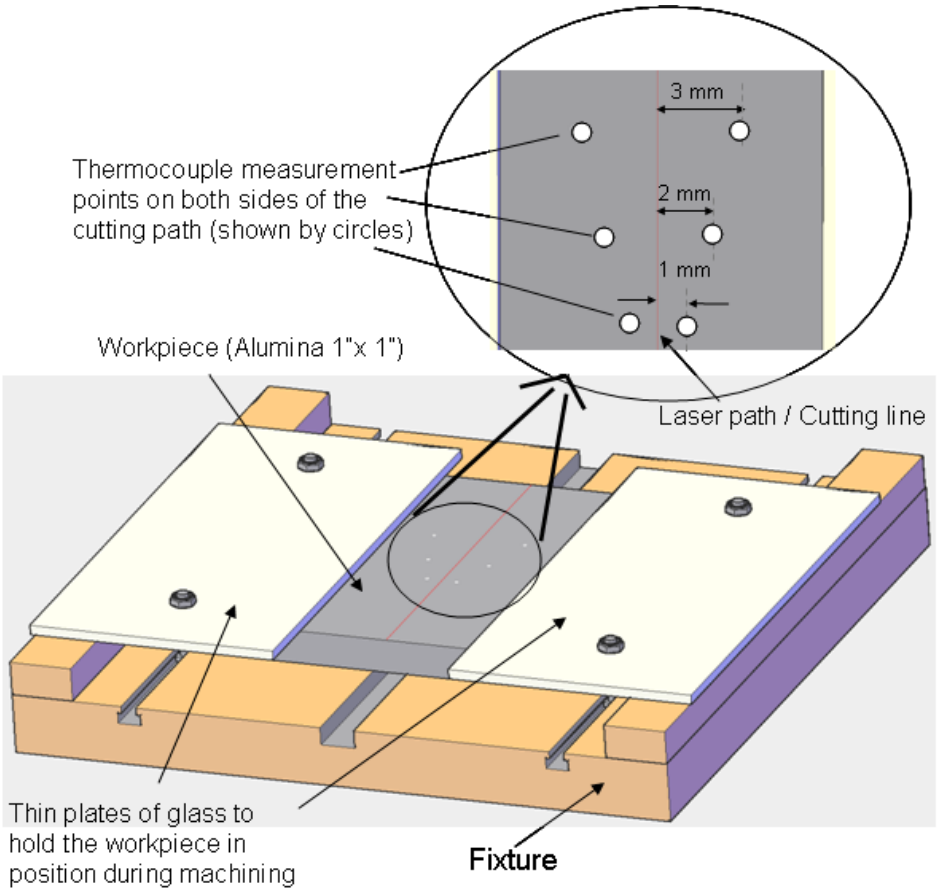

Fig 3.2 Schematic representation of the fixture with the workpiece in position during machining. Inset shows the thermocouple measurement points for recording the temperature history

3.3.1 Experiments on Machining of Alumina

LWJ experiments were conducted to investigate the effect of two process parameters – line energy (Laser energy per unit cutting length) and surface energy density (Laser energy per unit surface area) – on fracture behavior of alumina samples. Different values of process parameters were achieved by varying the laser power from 100 to 200 W and cutting speed from 25 to 50 mm/s (60 to 120 inch/min) and using two different laser spot sizes (0.6 mm (defocused beam) and 0.2 mm (focused beam)). Other process parameters such as water pressures, distance of separation between the heating and the cooling zone, and water-jet nozzle size were set at 2 MPa, 1.3 mm and 0.3 mm, respectively.

3.3.2 Thermal History of Alumina Samples during LWJ cutting

Thermocouples were attached to alumina samples at offset distances of 1 mm, 2 mm, and 3 mm from the laser path (as schematically shown in the inset of Fig 3.2) to record temperature history during laser/water-jet cutting. The temperature was measured using K-type thermocouples with 0.8 mm head diameter (Omega, PA) suitable to measure temperatures up to 1250°C. A data acquisition system was used to record the temperature at a time interval of 0.5 s during the LWJ cutting.

3.4.Thermal Stress and Crack Driving Force Calculation

An analytical model is developed to predict the temperatures and stress fields in alumina samples undergoing laser/water-jet machining. Computed stress field are subsequently used to obtain a relationship between the process parameters and driving forces for different configurations of cracks that lead to cutting/scribing of workpiece.

3.4.1 Analytical solution of temperature and stress fields

Temperature distribution, $T(x,y,z,t)$, in the workpiece is determined by modeling the laser and water-jet as rectangular source and sink [19], respectively as shown schematically in Fig 3.3 in order to simplify the analytical solutions. Transient temperature distribution are obtained by the solution of following diffusion equations

$$c_p\rho\frac{\partial T}{dt} = k\nabla^2 T + q\left(x,y,t,I_h,I_c\right)$$

where

$$q\left(x,y,t,I_h,I_c\right) = I_h \mathrm{H}\left(h_x - |x|\right)\left[\mathrm{H}\left(vt-y\right) - \mathrm{H}\left(vt-y-2h_y\right)\right] - I_c \mathrm{H}\left(c_x - |x|\right)\left[\mathrm{H}\left(vt-2h_y-l_0-y\right) - \mathrm{H}\left(vt-2h_y-l_0-2c_y-y\right)\right] \quad \text{Eqn (1)}$$

where c_p is the specific heat of the material, ρ is the density of the material, k is the conductivity of the material, $q(x,y,t,I_h,I_c)$ is the total heat input, I_h is the heating intensity of the laser beam and I_c is the cooling intensity of the water-jet, H is the Heaviside function, v is the velocity of the cutting head h_x, c_x, h_y, c_y are the half lengths of the heating and cooling zones along x and y direction respectively and l_0 is the separation distance between the laser spot and the waterjet cooling zone on the surface of the workpiece. Elperin et al. [19] have previously reported an analytical solution for the temperature field using an error function representation that provides an elegant solution but leads to complicated and cumbersome expressions in calculation of thermal stress distributions. In order to simplify the thermal stress calculation, we have used an Eigen function expansion for solution of temperature fields.

Both the laser heating and waterjet cooling occurs on the top surface, and hence the convective heat transfer boundary conditions are used for the top surface. Insulated boundary conditions are used at the bottom surface. Convective heat transfer boundary conditions are used for all the side surfaces except y = 0 mm (starting edge) which is modeled as an insulated surface to simplify the analytical solution. As a result, initial and boundary conditions for the heat flow are:

$$T(x,y,z,t=0)=T_0$$

$$k\frac{\partial T}{\partial z}_{z=d/2}=k\frac{\partial T}{\partial x}_{x=\pm a}=k\frac{\partial T}{\partial y}_{y=b}=-h(T-T_A):$$

$$\frac{\partial T}{\partial z}_{z=-d/2}=\frac{\partial T}{\partial y}_{y=0}=0\ \left(\text{Insulated Boundary Condition}\right) \qquad \text{Eqn (2)}$$

The transient temperature distribution is determined using a Green's function approach

$$T(x,y,z,t)=\int_0^t\int_0^b\int_{-a}^a q(x_0,y_0,t_0,I_h,I_c)\theta(x,x_0,y,y_0,z,t,t_0)dx_0dy_0dt_0+T_0 \qquad \text{Eqn (3)}$$

where $\theta(x,x_0,y,y_0,z,t,t_0)$ is the solution to the associated problem

$$c_p\rho\frac{\partial T}{dt}=k\nabla^2T+\delta(x-x_0)\delta(y-y_0)\delta(z-\frac{d}{2})\delta(t-t_0) \qquad \text{Eqn (4)}$$

Eigen function expansions along x, y, z coordinates are utilized to determine the series representation of green's function θ.

$$\theta(x,x_0,y,y_0,z,t,t_0)=\frac{\kappa}{k}\sum_{n=1}^{\infty}exp\left(-\kappa\omega_n^2(t-t_0)\right)cos(\omega_n x)cos(\omega_n x_0)\cdot$$
$$\sum_{m=1}^{\infty}exp\left(-\kappa\xi_m^2(t-t_0)\right)cos(\xi_m y)cos(\xi_m y_0)\cdot \qquad \text{Eqn (5)}$$
$$\sum_{l=1}^{\infty}exp\left(-\kappa\psi_l^2(t-t_0)\right)cos(\psi_l d)cos\left(\psi_l(z+d/2)\right)\cdot \mathrm{H}(t-t_0)$$

where ω_n, ξ_m, ψ_l are the Eigen values along x, y, z directions κ is thermal diffusivity.

Non-uniform heating and cooling of the specimen leads to development of thermal stresses in the specimen [20]. Uncoupled quasistatic thin plate analysis is used to determine the resulting thermal stress fields. For the sake of brevity, only the stress component (σ_{xx}) along the x axis that results in opening or closing of micro-cracks is discussed. Similar analysis may be utilized to calculate the other components of stress. Normal stress along x axis of free plate subjected to the temperature distribution, $T(x,y,z,t)$ is:

$$\sigma_{xx} = \frac{1}{1-\upsilon}\left(-\alpha E T + \frac{1}{d}((1-\upsilon)N_x + N_T)\right) - \frac{12zD}{d^3}\left(\frac{\partial^2 w}{\partial x^2} + \frac{\partial^2 w}{\partial y^2}\right) \qquad \text{Eqn (6)}$$

where ν is Poisson's ratio, α is the coefficient of thermal expansion, E is the young's modulus, N_x is the in-plane force per unit length, D is bending rigidity of the plate per unit length, w is the out-of-plane displacement along z direction and N_T is calculated as:

$$N_T = \alpha E \int_{-d/2}^{d/2} T dz \qquad \text{Eqn (7)}$$

The in-plane forces per unit length are determined from the in-plane equilibrium equations while the out-of–plane displacement field is determined from equilibrium of moments and out-of-plane forces.

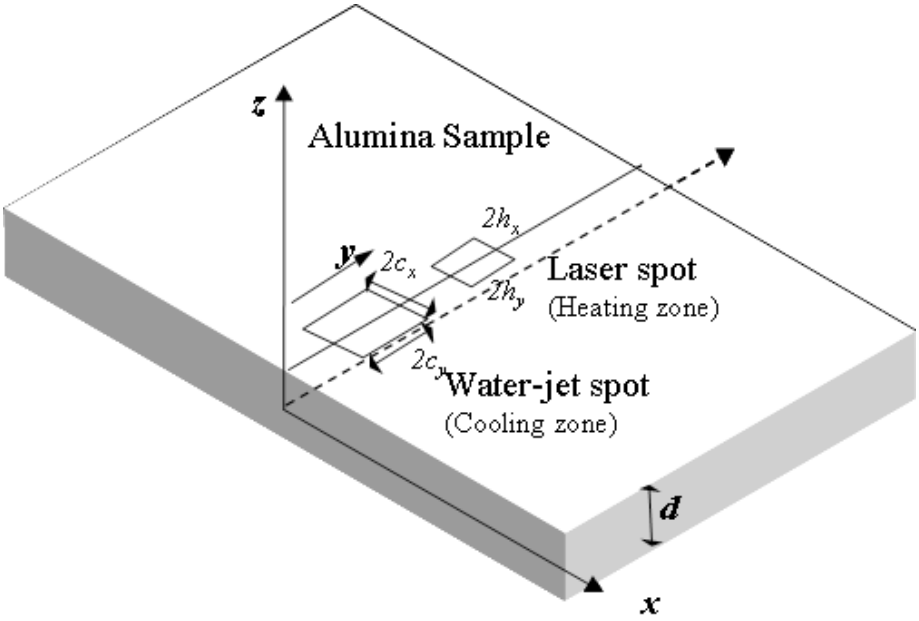

Fig 3.3: Orientation of the axes with respect to the workpiece. Y- axis represents cutting direction

The thermo-mechanical analysis of Laser/Water-jet machining is based on the following assumptions: physical and thermal properties of materials and surface heat transfer coefficients are assumed to be independent of temperature and uncoupled quasistatic thermoelasticity are used to describe material response. In addition, only a small volume of material is expected to undergo melting, evaporation and resolidification during LWJ machining and it is assumed that this small volume has a minimal influence

on thermal stress development in rest of the specimen. Consequently, the process of material melting, evaporation and solidification are not included in this analysis.

3.4.2 Computational Procedure for crack driving forces

During LWJ machining, laser irradiation not only heats the surface but also causes localized damage that results in crack nucleation and propagation during the waterjet quenching. Laser-induced damage can result into two possible crack configurations — edge crack towards center of plate or channeling crack along the surface — schematically represented in Fig 3.4. LWJ machining is represented through a two step analysis: 1) at the beginning of the cut when there are no pre-existing cracks in the workpiece, plain strain analysis of edge crack is utilized to approximate the initial cut depth; and 2) subsequent analysis of the channeling crack is utilized to approximate the propagation of the initiated cut along the laser path.

Thermal stress fields are used to compute the crack driving forces corresponding to different crack lengths for both crack configurations. The stress intensity factors for plane strain edge cracks are calculated using the weight function method for Mode I loading of crack in the *x*-*z* plane [21]. The weight functions for different crack lengths were computed using a finite element package, ABAQUS (Providence, RI).

The channeling of an edge crack is a three dimensional process and for steady state crack extension, it is assumed that edge crack will channel at fixed depth, with a constant tip shape and constant release rate. Hence, driving force for a steady state crack growth is determined from average energy release rate over the depth of the channeling crack front [17].

$$G_t = \frac{1}{a}\int_0^a G_p(a')da' \qquad \text{Eqn (8)}$$

The stress intensity factor calculated for plane strain cracks are used in above equation to compute the energy release rate for channeling cracks of different depths.

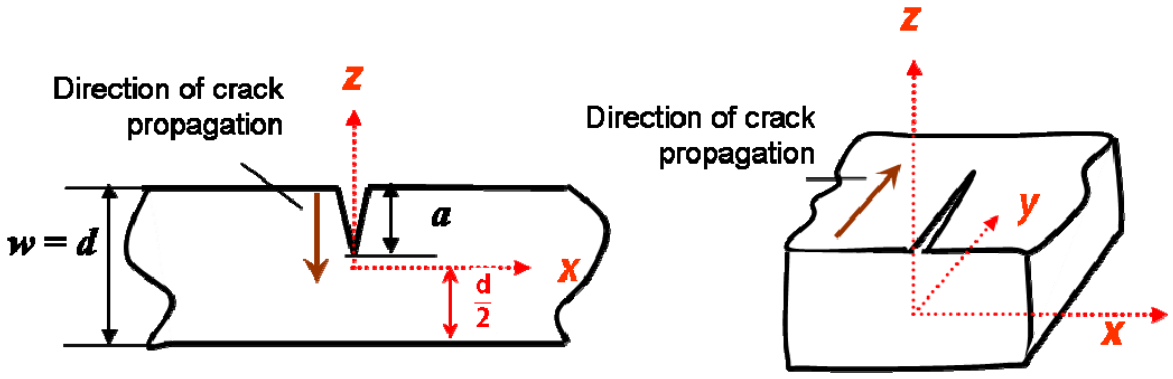

Fig 3.4 (a): Plane strain cracking (b): Crack Channeling

3.5.Experimental Results

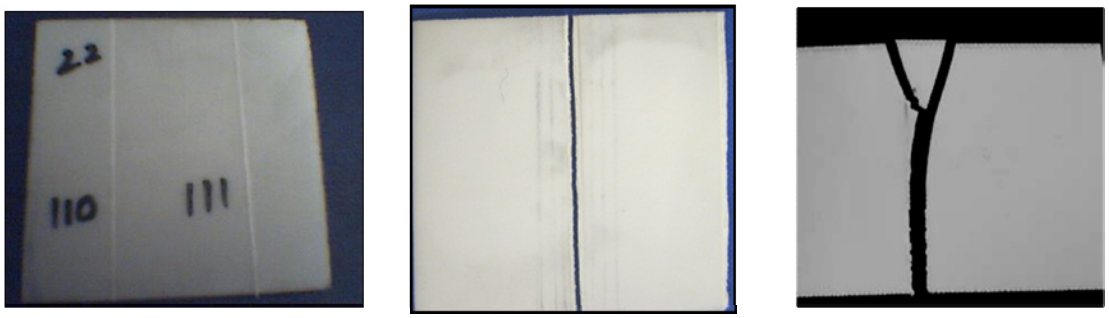

Fig 3.5 (a): Photographs of scribing (left), (b): controlled (center) and (c): uncontrolled fracture (right).

The samples obtained from cutting experiments were categorized on the basis of observed fracture response into scribing, controlled separation, and uncontrolled fracture as shown in the Fig 3.5. Fracture behavior at different line-energy (laser energy per unit length) inputs is plotted in Fig 3.6(a) for the two laser spot sizes. Cutting experiments with focused spot size of 0.2 mm results in uncontrolled cracking for high line energy values and controlled separation or scribing for only a narrow range of line energy values. In contrast, 0.6 mm spot size resulted in controlled separation over a wide range of line energy values and a sharp transition from scribing to controlled separation at a line-energy value of 4.00 J/mm.

Observed fracture behavior are also plotted as a function of surface energy density (laser energy per unit irradiated area) in Fig 3.6(b). At lower values of surface energy density samples either undergo scribing or controlled separation but at larger magnitudes of surface energy density, samples undergo uncontrolled cracking. These experiment results indicate that both line-energy and surface energy density are important parameters in determining controlled separation of alumina samples undergoing LWJ machining. Thus, line-energy determines the transition from scribing to fracture for larger spot sizes while the surface energy density determines the transition from controlled cracking to uncontrolled cracking.

Depth of crack induced in the scribed samples during LWJ machining was also measured to compare with theoretical predictions of crack growth. For this purpose, a low surface tension dye was applied and allowed to dry on the top surface. Subsequently, the samples were broken along the scribed crack and examined with the help of scanning electron microscope (SEM). Typical SEM images of cracked samples scribed at low (3 J/mm) and high line energy values (4 J/mm) are presented in Fig 3.7(a) and (b), respectively. The dye covered surfaces appear darker than uncovered alumina surfaces due to a difference in atomic numbers and hence can be used to identify the scribed crack depth. In the samples scribed at low line energy values, dye penetration and depth of scribed crack is consistently found to be less than 100 μm or less than 10% of sample thickness (Fig 3.7(a)). In the samples scribed at high line energy values, maximum dye penetration is found to be approximately 600-700 μm or about 60-70% of sample thickness. For the deeper cracks dye seems to have flown along the crack in form of fingers which may be attributed to the small crack opening to depth ratio. Hence, we have approximated the scribed crack depth at high line energy values to be the maximum dye penetration at about 60-70% of sample thickness.

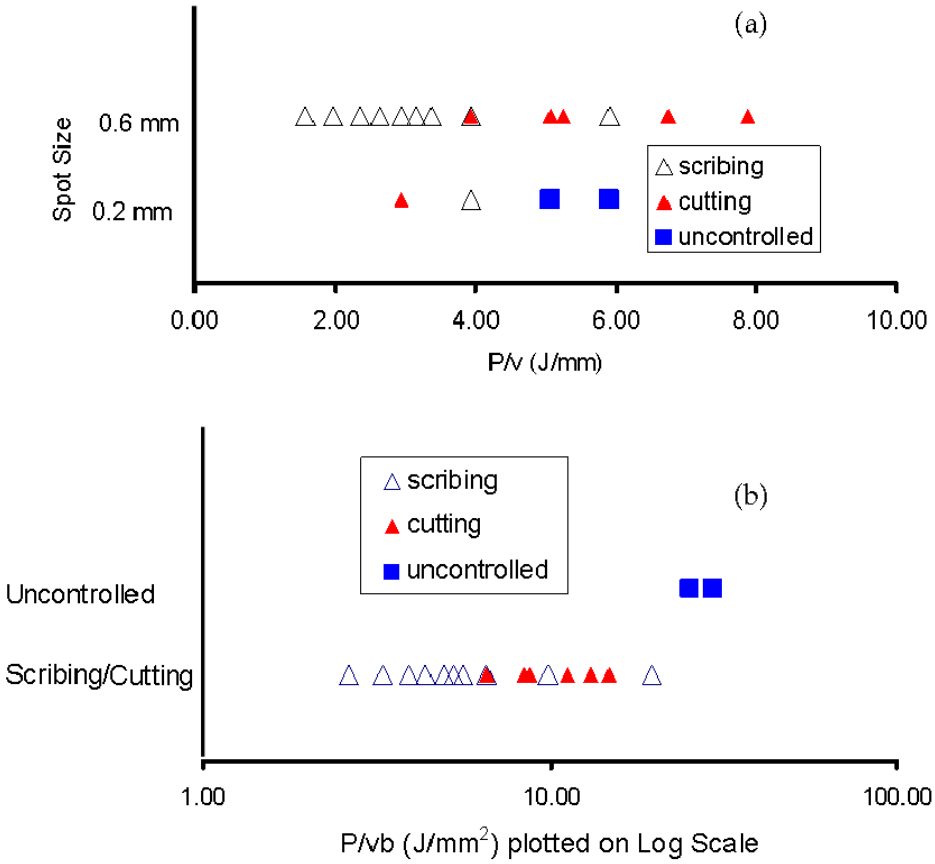

Fig 3.6(a): LWJ cutting of alumina for different spot sizes at 2.07 MPa water pressure (b): LWJ cutting results at 2.07 MPa water pressure

Representative temperature histories recorded at points that are at distances of 1 mm and 2 mm from the cutting line during LWJ machining at laser power of 150 W, spot size of 0.6 mm and cutting velocity of 29.6 mm/s (70 inch/min) are plotted in Figs 8(a) and (b), respectively. Temperature values measured at opposite sides of laser path match each other within ± 2°C.

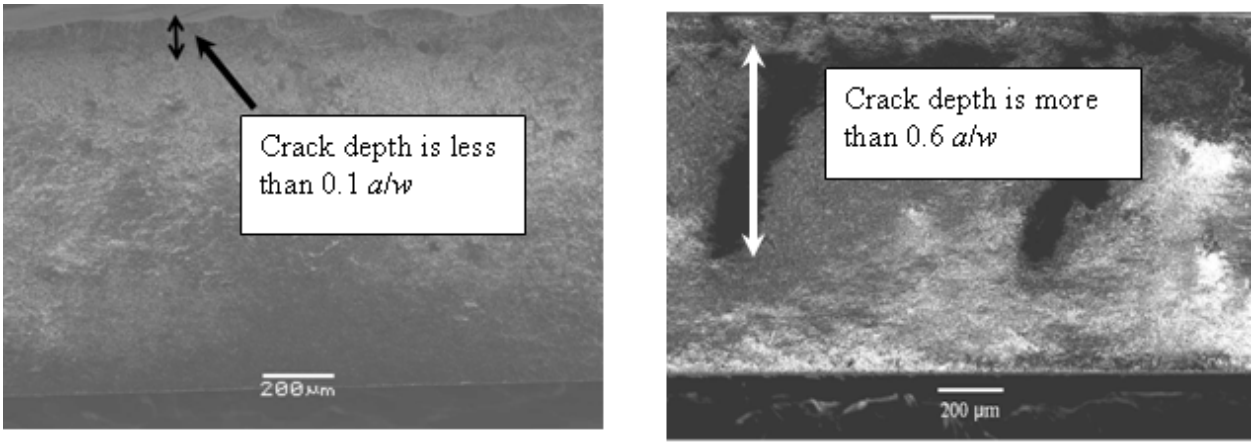

Fig 3.7: SEM image of dye penetration in broken scribed specimens (a): low line energy scribing (b): high line energy scribing.

3.6. Analytical Predictions and Discussion

3.6.1 Temperature and thermal stress distributions

Transient temperature and stress distributions in the alumina specimen were evaluated for a range of process parameters. In the analytical model, quantities such as specimen dimensions, cutting velocity, laser spot size, water-jet area, separation between laser beam and water-jet were chosen to exactly match the experimental conditions. Material properties used for alumina specimen are given in Table 1 and are assumed to be temperature independent. Intensity of the heat flux incident over laser spot was determined from:

$$I_h = a_s \frac{4P}{\pi b^2} \qquad \text{Eqn (10)}$$

where P represents laser power, b represents the diameter of the laser beam spot used in LWJ machining, and a_s represents the absorption coefficient for the alumina specimen. Alumina is known to exhibit high absorption of CO_2 laser radiation (on the order of 95%) [22, 23]. It was assumed that a_s = 0.72 i.e. 72% of the laser incident energy is absorbed in the sample based on approximating 5% losses in the laser optics and 20% losses due to the presence of water vapor and 95% absorbance of CO_2 laser beam at 10.6 µm wavelength for alumina

In the numerical model, waterjet quenching of the laser heated area is approximated using a heat sink along with convective cooling over the top surface because the large temperature variation over the sample generates non-uniform convection involving both forced convection due to water flow as well as pool boiling over the cutting path (water vapor/mist formation was observed during the experiments). The cooling intensity of heat sink and convection heat transfer coefficient were estimated using the following two assumptions: 1) waterjet quenching will rapidly reduce the temperature of laser heated area to room temperature; and 2) flow of water over the sample will result in forced convection (with coefficient value between 50 – 20,000 W/m^2K [24, 25]. In addition, analytical predictions were compared against measured temperature histories to obtain the effective sink intensity and heat transfer coefficient over the surface.

Temperature distribution is computed for a finite area of 0.04m X 0.1m for the boundary conditions mentioned in Eqn (3), using 50 Eigen values along x and z axis and 400 Eigen values along y axis. Number of Eigen values along each direction was chosen on the basis of numerical convergence studies to ensure that increase in the number of Eigen values produces an insignificant change in the predictions of maximum tensile stress on the surface during waterjet quenching. Comparison of numerical predictions for different combinations of laser power and cutting velocity showed that the predicted temperature and thermal stresses were approximately same for a fixed line energy value. Hence for the sake of brevity, all the results are presented as a function of line energy rather than different laser power and cutting velocity values.

Predictions at 1 mm from cutting path for three different cooling intensities and convective heat transfer coefficients are compared with experimental measurements during LWJ machining at line energy of 5 J/mm for a spot size of 0.6 mm in Fig 3.8(a). Case A corresponds to a cooling intensity (I_c) of 25 x 10^6 W/m^2 and convective co-efficient of 10 x 10^3 W/m^2K, Case B corresponds to a cooling intensity (I_c) of 25 x 10^6 W/m^2 and convective co-efficient of 6 x 10^3 W/m^2K and Case C corresponds to a cooling intensity (I_c) of 50 x 10^6 W/m^2 and convective co-efficient of 10 x 10^3 W/m^2K.

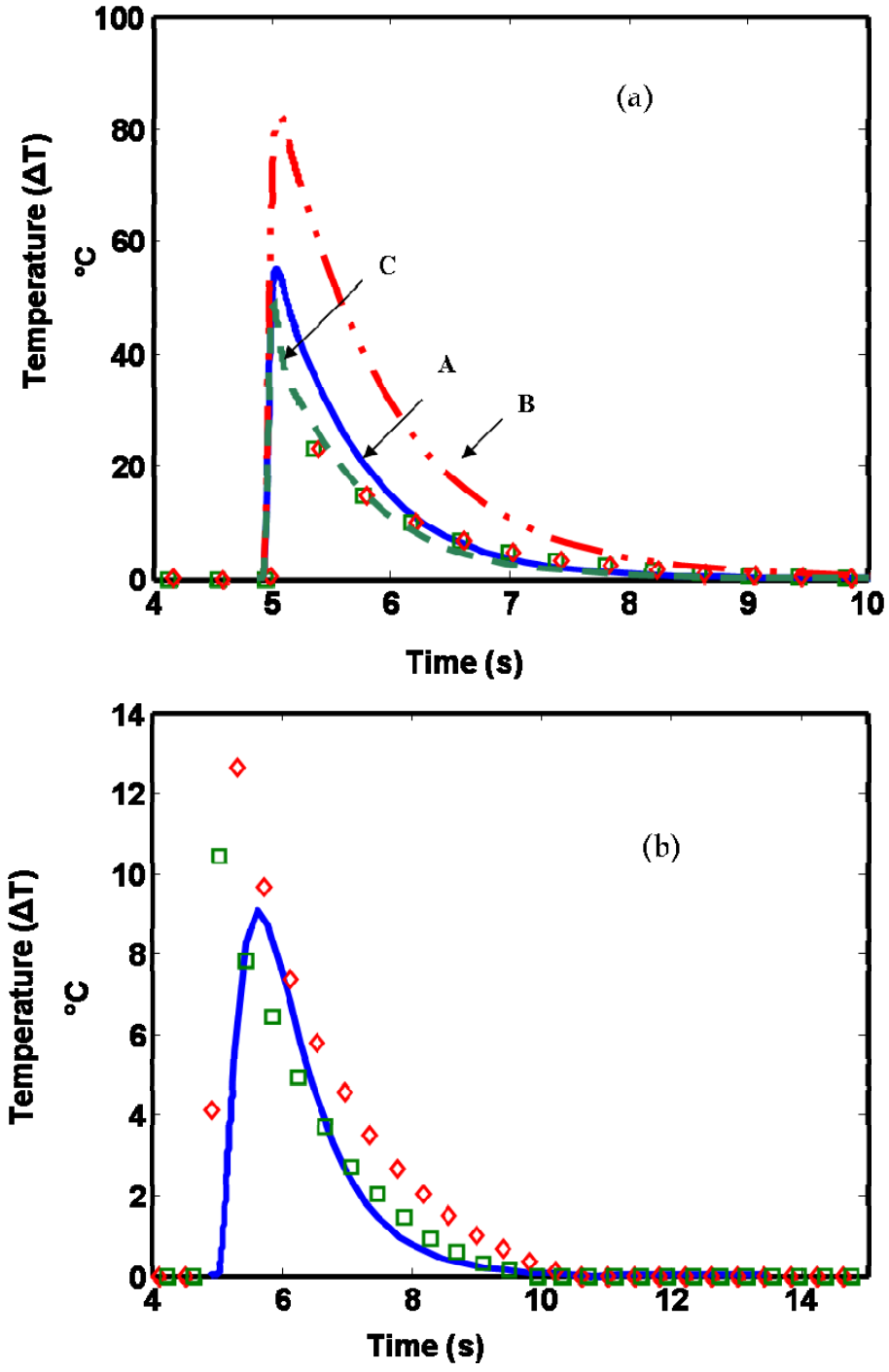

Fig 3.8: Comparison of experimental measurements and numerical prediction of temperature during LWJ machining: (a): Temperature measured at 1 mm from cutting path (markers) and numerical predictions (b) Measured temperature and numerical predictions (curve A) at 2 mm offset from cutting path.

A comparison of the three curves reveals that heat transfer coefficient determines the peak temperatures while cooling intensity determines the rate of cooling during the quenching process. Best approximation of the experimental data is achieved in case C but this choice of cooling intensity results in quenching of material on the cutting path to temperatures significantly below the waterjet temperature. As a result, value of cooling intensity in Case A was chosen to approximate the LWJ machining for line energy of 5 J/mm because it ensures quenching of material on the cutting path to room temperature and produces reasonable agreement to the experimentally measured temperature at distance of 1 mm and 2 mm from the cutting path as shown in Figs 3.8 (a) and 3.8(b), respectively.

Table 3.4: Properties of Alumina used in the analysis

Density (kg/m^3)	Thermal Conductivity (W/mK)	Specific Heat Capacity (J/kgK)	Young's Modulus (GPa)	Thermal Coefficient of Expansion (/K)
3720	5	1320	330	8.5×10^{-6}

Similar procedure was utilized to identify the cooling intensity that approximates the waterjet quenching at other line energy values. Predictions of temperature history at a point along the cutting path corresponding to two different line energy values (3.9 and 5 J/mm) are plotted in Fig 3.9(a). The peak temperatures are predicted to be higher than the melting temperature as the model considers conduction only. Phase transformations in the form of melting, vaporization, and resolidification are ignored in this analysis and as a result peak temperature predictions for points along the laser path are higher than vaporization temperature. It is appropriate to note that our main focus will remain in the prediction of tensile stresses which occurs during cooling rather the compressive stresses during heating and hence the melting and vaporization effect can be ignored. Also, the size of such high-temperature zones are small (~ 70 μm) and are shown in the experimental results discussed in ref [5]. However, these very high temperatures do not affect the calculation of crack driving forces and subsequent conclusion. It is

important to note that peak temperatures and associated compressive stresses does not influence the tensile stresses generated during water-jet quenching, and hence our assumption of ignoring phase transformations is justified and our model successfully captures the essential mechanisms governing material separation during LWJ machining.

Predictions of in-plane stress component, σ_{xx}, for LWJ machining at line energy of 3.9 J/mm at top, middle and bottom surface at a point along the laser path are plotted in Fig 3.9(b). Arrival of laser spot on the top surface leads to rapid heating and development of compressive stresses. Quenching of the laser heated area with the waterjet results in development of large tensile stresses on the top surface while the middle and bottom surface are relatively unstressed. Through-the-thickness stress distribution at the instance of maximum tensile stress on top surface is plotted in the inset shown in Fig 3.9(b). This large in-plane tensile stress will result in propagation of cracks that lead to scribing or splitting of the specimen.

Our solution approach for both temperature and stress calculation relies on summation of Eigen functions for temperature and stress computations. Number of Eigen values along each direction was chosen on the basis of numerical convergence studies to ensure that increase in the number of Eigen values produces an insignificant change in the predictions of maximum tensile stress on the surface during waterjet quenching. Eigen function expansion provides a simple form for the temperature and stresses but suffers from very slow convergence in resolving large gradients associated with changes in sign of surface heat flux from laser heating to waterjet cooling. The slow rate of convergence leads to wavy profile for the temperature between the laser heating and subsequent cooling. Increasing the number of Eigen functions in the temperature and stress calculations lead to smoother curves but leads to extremely large computational times. However, the increase in Eigen values has no effect on the magnitude of maximum tensile stress that occurs away from this undulating profile. Since the focus of this paper is to determine the crack propagation driven by the maximum tensile stress, convergence studies were based on the magnitude of maximum tensile stress rather than the shape of overall temperature curves.

3.6.2 Crack driving forces

Predicted stress histories were used to calculate the driving forces for plane strain and channeling cracks configurations. Crack driving forces reach the maximum at the instant when the top surface is subjected to maximum tensile stress during waterjet quenching (shown in Fig 3.9(b)). The computed stress intensity factors for plane strain cracks at that instant are plotted as a function of crack length for four different processing parameters in Fig 3.10. Computed energy release rates for channeling cracks are plotted as a function of crack depth for the same processing conditions in Fig 3.11. First three predictions correspond to LWJ machining with a laser spot size of 0.6 mm and line energies of 3.0, 3.9, and 5.0 J/mm, respectively. First two line energy line values resulted in scribing while the third case corresponds to controlled separation of alumina specimens. The fourth prediction corresponds to LWJ machining with spot size of 0.2 mm and line energy of 5.0 J/mm which results in high surface energy density (33 J/mm^2) and uncontrolled cracking. In all the cases, stress intensity factor (K_I) and energy release rates (G) are highest for cracks that are approximately 0.1 times the thickness due to the large tensile stresses induced on the top surface during quenching. K_I and G rate decreases as the crack becomes longer and reach a minimum for cracks that are roughly 0.5 to 0.6 times the thickness due to the compressive stresses induced in the middle portion of material (Fig 3.9(b)). In addition, increase in both line energy and surface energy density leads to increase in computed values of K_I and G. For the same line energy value, LWJ machining with smaller spot size results in higher values of K_I and G for cracks shorter than 0.4 times the thickness.

Numerical predictions of K_I and G are also compared to alumina's fracture toughness (K_{Ic}) and critical energy release rate (G_c) in Figs 10 and 11, respectively, in order to estimate the cut depth at the start of LWJ machining as well as the equilibrium depth of the channeling crack for each processing condition. As shown in the Fig 3.10, K_I for cracks shorter than 0.25 to 0.45 times the thickness is larger than K_{Ic} of alumina for the given range of line energy values. Thus, the initial cut depth will be in the range of 0.25 times to 0.45 times thickness. In addition, G for channeling cracks of these depths is higher

than G_c for the processing parameters considered in Fig 3.11, therefore the initial cracks are expected to propagate along the laser path. However, these predictions of cut depth are most appropriate for machining situations where laser irradiation-induced damage is only confined to the top surface of the specimen. These predictions cannot be directly compared to experimental observations of through-cuts where laser radiation is incident over the specimen boundary resulting in damage and subsequent cracking across the whole thickness during waterjet quenching. As a result, equilibrium depth of a channeling crack is most appropriate for determining the LWJ induced cut depth in the current experiments.

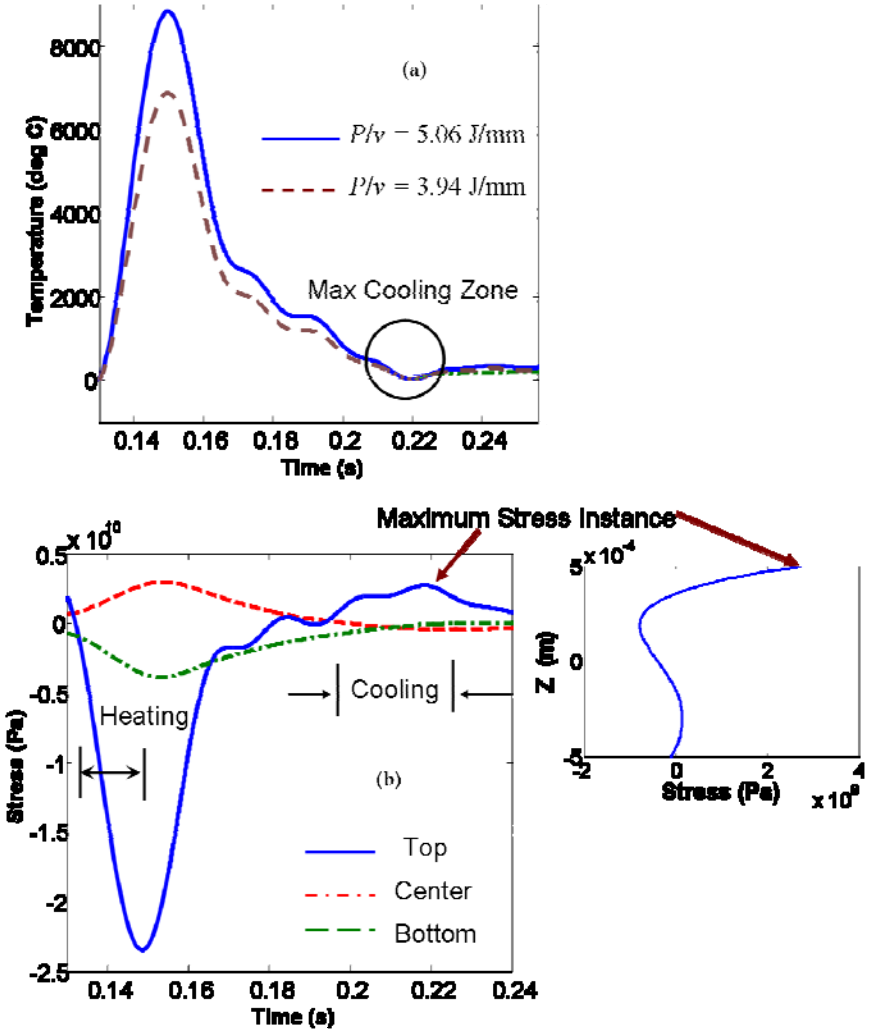

Fig 3.9 (a): Temperature plot at x = 0 m, and y = 0.004 m at various line energies. (b): Stress plot at x = 0 m, and y = 0.004 m at various z with the inset showing the stress across the thickness.

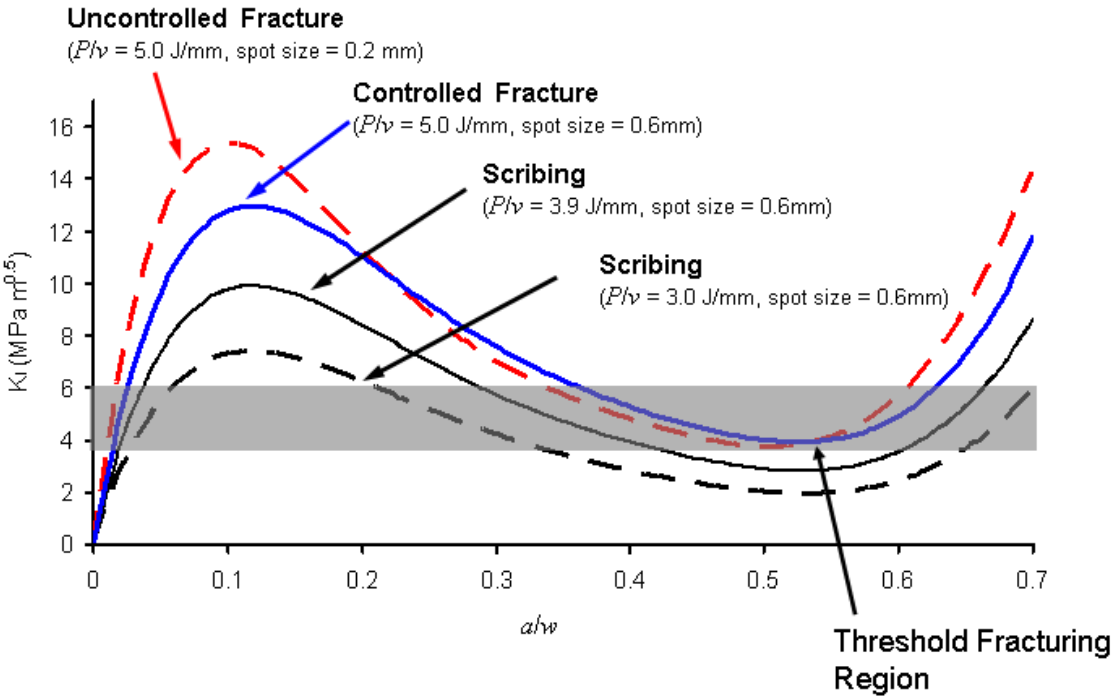

Fig 3.10: KI at various a/w (a ≡ crack length and w ≡ thickness) ratios

The maximum value of G increases with increase in line energy (P/v) for a fixed spot size of 0.6 mm as shown in Fig 3.10 and 11 respectively (see controlled fracture (P/v = 5 J/mm) and scribing (P/v = 3.9 J/mm, & P/v = 3.0 J/mm)). At line energy values lower than 3.0 J/mm, G for all crack length is lower than G_c hence scribing with crack depth less than 0.1 times the thickness is observed (see Fig 3.7(a)). For line energy values between 3.0 J/mm to 3.9 J/mm, G for short cracks is greater than G_c but for cracks approx 0.6 times the thickness G is lower than G_c and as a result, scribing with crack depth 0.6 time the thickness is observed. As the line energy values are further increased, the G value for all crack lengths becomes greater than G_c resulting in channeling of through-the-thickness cracks or material separation. In order to verify this hypothesis, magnitudes of predicted minimum G for channeling cracks are plotted as a function of line energy in Fig 3.12 for a fixed spot size of 0.6 mm. Comparison of the magnitude of minimum energy release rate to range of G_c indicates that transition from scribing to material separation

should occur for line energy value between 3.4 to 4.4 J/mm. During the cutting experiments, the transition from scribing to material separation is observed at line energy value of 3.9 J/mm and this excellent agreement between numerical predictions and experimental observations validates the hypothesis. Thus, the magnitude of minimum energy release rate may be used for predicting the transition from scribing to material separation during LWJ machining.

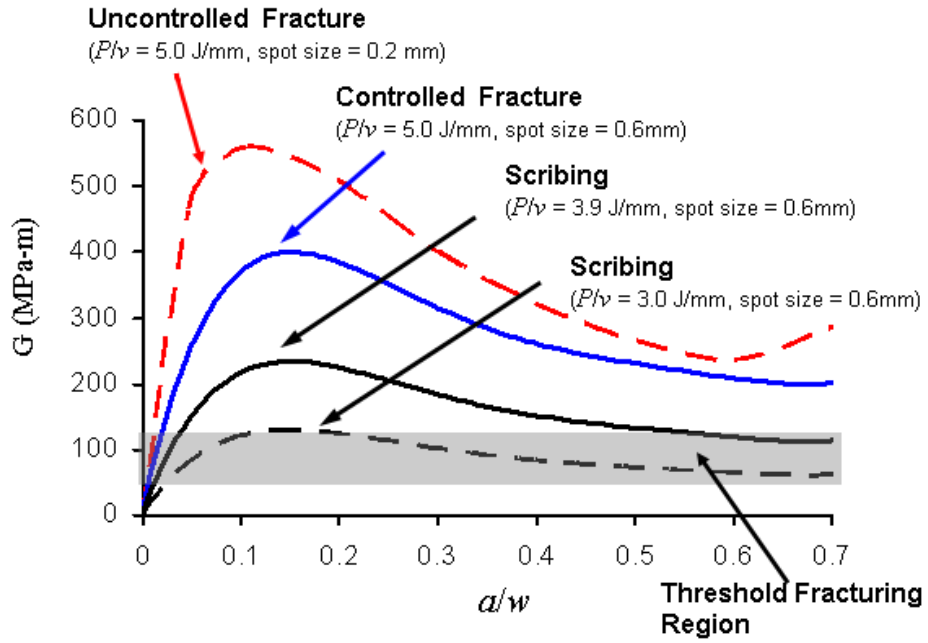

Fig 3.11: G curve at various a/w (a ≡ crack length and w ≡ thickness) ratios

During material separation, the transition from controlled separation to uncontrolled cracking depends on the surface energy density. As seen in Fig 3.11, the G for shorter cracks (smaller a/w) is much larger in the case of high surface energy density ("Uncontrolled fracture (33 J/mm^2)). Previous work [26] on stability of crack path has shown that increase in driving forces can result in transition from single straight crack to undulating and branched crack propagation. In addition, the extent of surface damage during laser irradiation is expected to scale in proportion to surface energy density. Therefore, the increase in surface damage and larger driving forces for smaller cracks are expected to result in transition from controlled separation to uncontrolled cracking. Based on the experimental observations, surface

energy density of 33 J/mm² is identified as the critical value at which transition from controlled separation to uncontrolled cracking takes place.

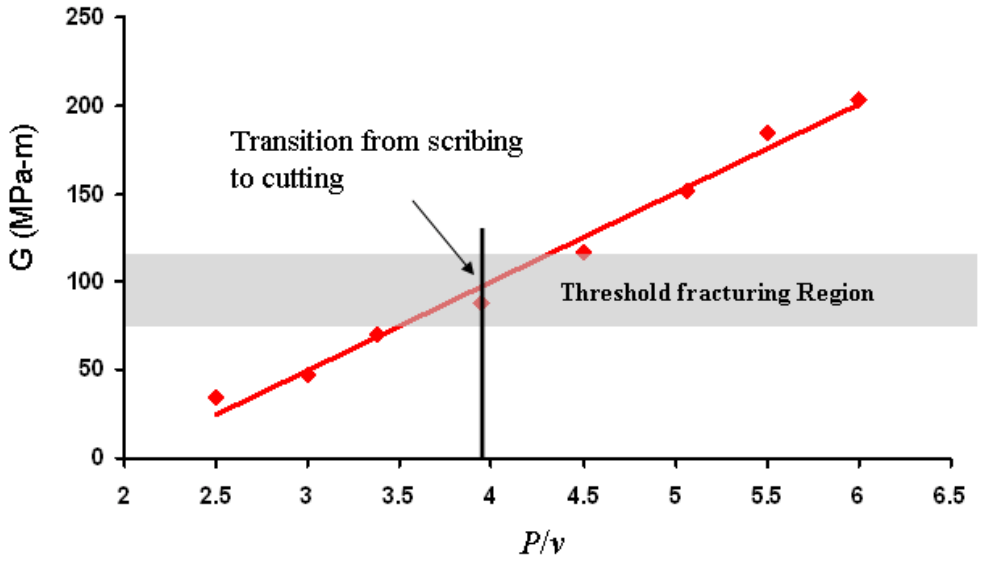

Fig 3.12: Minimum energy release rates plotted as a function of line energy for spot size of 0.6 mm.

Number of numerical simulations of LWJ machining at different line energy and surface energy values are carried out to create a map shown in Fig 3.13 that relates process parameter to expected fracture characteristics of alumina specimens. Minimum *G* for channeling cracks are used to identify the transition from scribing to material separation and critical value of surface energy density is utilized to predict transition from controlled separation to uncontrolled cracking. Line energy values greater than 30 J/mm will result in "melt and blow" mode of material separation in alumina [24] and hence are the upper limit of line energy values in LWJ machining. Experimental observations at laser spot sizes of 0.2 and 0.6 mm and numerical predictions at spot size of 0.4 mm are also plotted on the process map. The process map will serve as a useful tool for identifying appropriate LWJ parameters for cutting or scribing of alumina.

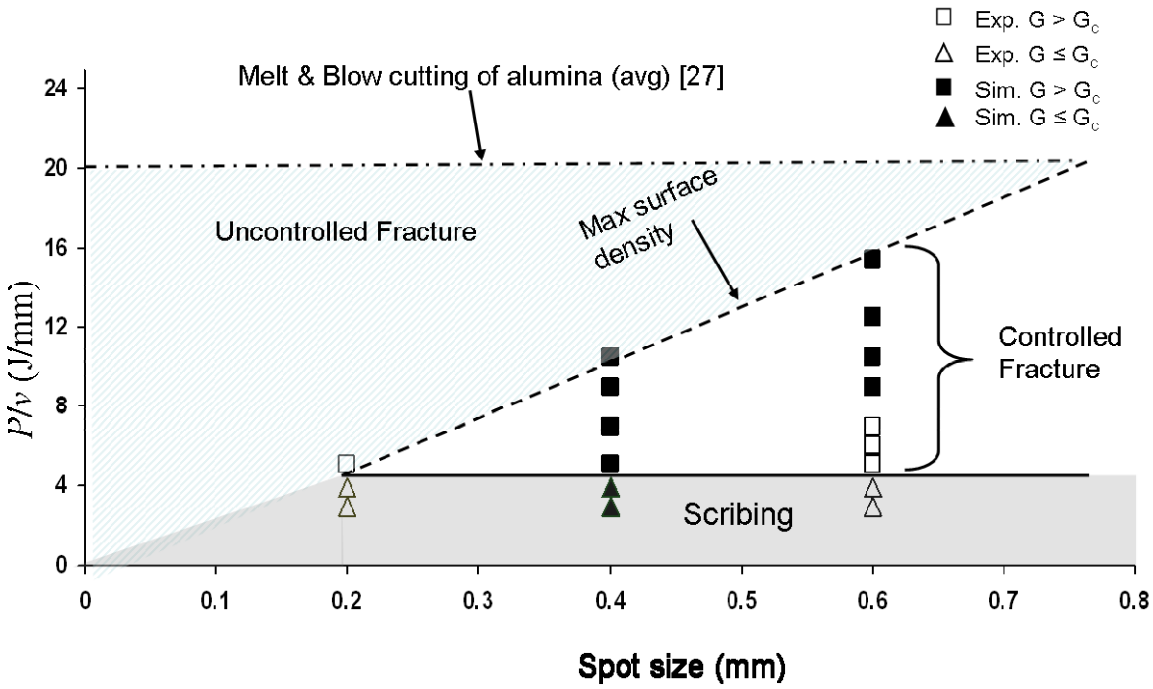

Fig 3.13: Graph relating process parameters and fracture characteristics

3.7. Conclusions

The analytical model and experimental results presented in the paper clearly demonstrate that fracture mechanics based approach can be used to design hybrid machining processes for brittle materials. A hybrid laser/waterjet machining process is investigated for cutting alumina specimen. Cutting experiments were conducted to observe fracture characteristics of alumina samples. Numerical model were developed to predict temperature, stress field and driving forces for cracks that results in scribing and separation of workpiece. Comparison of experimental and numerical results indicated that critical value of driving force for channeling cracks determines the transitions between scribing to material separation whereas a critical value of surface energy density determines the transition from controlled separation to uncontrolled cracking of the workpiece. Based on these observations, a map is created to relate process parameters to fracture characteristics of alumina specimens.

Acknowledgements

The authors gratefully acknowledge the financial support for this research provided by the U.S. National Science Foundation under the Grant DMI-0522788.

3.8. References

[1] M. Hashish, "Cutting with Abrasive Waterjets," *Mechanical Engineering*, vol. 106, pp. 60-69, 1984.

[2] P. Gudimetla, J. Wang, and W. Wong, "Kerf formation analysis in the abrasive waterjet cutting of industrial ceramics," *Journal of Materials Processing Technology*, vol. 128, pp. 123-129, 2002.

[3] Schroede.Dh and F. L. English, "Comparison of Strength of Alumina Substrates for Different Separation Techniques," *IEEE Transactions on Parts Hybrids and Packaging*, vol. PHP8, pp. 4-6, 1972.

[4] H. Huang and Y. C. Liu, "Experimental investigations of machining characteristics and removal mechanisms of advanced ceramics in high speed deep grinding," *International Journal of Machine Tools & Manufacture*, vol. 43, pp. 811-823, 2003.

[5] D. Kalyanasundaram, G. Shehata, C. Neumann, P. Shrotriya, and P. Molian, "Design and validation of a hybrid laser/water-jet machining system for brittle materials," *Journal of Laser Applications*, vol. 20, pp. 127-134, 2008.

[6] L. Hong and L. J. Li, "A study of laser cutting engineering ceramics," *Optics and Laser Technology*, vol. 31, pp. 531-538, 1999.

[7] G. Shehata, Molian, P.A., Bastawros, A., and Shrotriya, P, "Surface finish and flexural strength of CO2 laser-cut alumina by evaporative and thermal stress fracture modes," in *Transactions of the North American Manufacturing Research Institute*, vol. 35: Society of Manufacturing Engineers, 2007, pp. 391-400.

[8] D. Kalyana-sundaram, Wille, J., Shrotriya, P., and Molian, P, "CO_2 Laser/Waterjet machining of Polycrystalline Cubic Boron Nitride," in *Transactions of the North American Manufacturing Research Institute*, vol. 36: Society of Manufacturing Engineers, 2008, pp. 517-524.

[9] R. M. Lumley, "Controlled Separation of Brittle Materials Using a Laser," *American Ceramic Society Bulletin*, vol. 48, pp. 850-854, 1969.

[10] C. H. Tsai and C. S. Liou, "Fracture mechanism of laser cutting with controlled fracture," *Journal of Manufacturing Science and Engineering-Transactions of the Asme*, vol. 125, pp. 519-528, 2003.

[11] C. H. Tsai and C. J. Chen, "Formation of the breaking surface of alumina in laser cutting with a controlled fracture technique," *Proceedings of the Institution of Mechanical Engineers Part B-Journal of Engineering Manufacture*, vol. 217, pp. 489-497, 2003.

[12] A. E. Segall, G. Cai, R. Akarapu, A. Romasco, and B. Q. Li, "Fracture control of unsupported ceramics during laser machining using a simultaneous prescore," *Journal of Laser Applications*, vol. 17, pp. 57-62, 2005.

[13] K. Li and P. Sheng, "Plane-Stress Model for Fracture of Ceramics During Laser Cutting," *International Journal of Machine Tools & Manufacture*, vol. 35, pp. 1493-1506, 1995.

[14] C. Barnes, P. Shrotriya, and P. Molian, "Water-assisted laser thermal shock machining of alumina," *International Journal of Machine Tools & Manufacture*, vol. 47, pp. 1864-1874, 2007.

[15] R. Akapura, Li, B., and Segall, A.E., "A thermal stress failure model for laser cutting and forming operations," *Journal of Failure Analysis and Prevention*, vol. 4, pp. 51-62, 2004.

[16] T. J. Lu and N. A. Fleck, "The thermal shock resistance of solids," *Acta Materialia*, vol. 46, pp. 4755-4768, 1998.

[17] L. G. Zhao, T. J. Lu, and N. A. Fleck, "Crack channelling and spalling in a plate due to thermal shock loading," *Journal of the Mechanics and Physics of Solids*, vol. 48, pp. 867-897, 2000.

[18] C. Olagnon, J. Chevalier, and V. Pauchard, "Global description of crack propagation in ceramics," *Journal of the European Ceramic Society*, vol. 26, pp. 3051-3059, 2006.

[19] T. Elperin, A. Kornilov, and G. Rudin, "Formation of surface microcrack for separation of nonmetallic wafers into chips," *Journal of Electronic Packaging*, vol. 122, pp. 317-322, 2000.

[20] B. A. Boley, and Weiner,J.H.,, *Theory of Thermal Stresses*. Mineola, New York: Dover Publications, Inc., 1997.

[21] H. Tada, Paris, P.C., and Irwin, G.R., *Stress Analysis of Cracks Handbook*. St, Louis: Del Research, MI, 1985.

[22] M. Khelkhal and F. Herlemont, "Determination of Effective Optical-Constants of Infrared Co2 Wave-Guide Laser Materials," *Applied Optics*, vol. 31, pp. 4175-4181, 1992.

[23] C. J. Moorhouse, F. Villarreal, J. J. Wendland, H. J. Baker, D. R. Hall, and D. P. Hand, "CO2 laser processing of alumina (Al2O3) printed circuit board substrates," *Ieee Transactions on Electronics Packaging Manufacturing*, vol. 28, pp. 249-258, 2005.

[24] F. P. Incropera, and DeWitt, D.P., *Introduction to heat transfer*, 3rd Edition ed: John Wiley & Sons, 1996.

[25] M. Ashby, F.,, *Materials Selection in Mechanical Design*. Oxford, England: Butterworth-Heinemann, 2001.

[26] B. Yang and K. Ravi-Chandar, "Crack path instabilities in a quenched glass plate," *Journal of the Mechanics and Physics of Solids*, vol. 49, pp. 91-130, 2001.

[27] W. Steen, *Laser Materials Processing*, 3rd Edition ed: Springer, 2003.

CHAPTER 4. FRACTURE MECHANICS BASED ANALYSIS FOR HYBRID LASER/ WATERJET (LWJ) MACHINING OF YTTRIA-PARTIALLY STABILIZED ZIRCONIA (Y-PSZ)

Dinesh Kalyanasundaram*, Pranav Shrotriya, and Pal Molian
Laboratory for Lasers, MEMS, and Nanotechnology
Department of Mechanical Engineering
Iowa State University
Ames, IA 50011

4.1. ABSTRACT

Conventional machining of yittria partially stabilized zirconia (Y-PSZ) is difficult and time consuming due to its high strength and fracture toughness. A non-traditional hybrid laser/water-jet process that combines CO_2 laser and abrasive-free waterjet (LWJ) was investigated for cutting of Y-PSZ substrates. The hybrid system exploits the low thermal shock resistance of Y-PSZ for controlled crack propagation along cutting path through localized heating and rapid quenching by laser and waterjet, respectively. Analytical solutions for temperature and stress fields in the workpiece during laser heating and waterjet quenching were developed and were used to identify the processing parameters required for controlled separation of Y-PSZ substrates. Cutting experiments were performed for a number of different processing parameters and cut surfaces were analyzed to identify the mechanisms responsible for observed fracture. Experimental results were compared with theoretical predictions to validate the modeling assumptions underlying analytical models of the hybrid cutting process. The experimentally validated model of the cutting process relates processing parameters to the different modes of machining of the workpiece and can be effectively used for hybrid cutting of Y-PSZ substrates.

KEYWORDS:

CO_2 Laser/Waterjet (LWJ) system, Zirconia, phase transformation, thermal shock, Griffith Energy, crack propagation, ceramic machining

* - *Corresponding author* – kdinesh@iastate.edu

NOMENCLATURE

q – Heating /cooling source term (W/m^2)

C_p - Specific heat capacity (J/kg K)

T - Temperature (K)

t - time (s)

υ - poisson's ratio

α -Thermal coefficient of expansion (/K)

ρ - Density of the material (kg/m^3)

κ - Thermal diffusivity of the material (m^2/s)

w -Thickness of the wafer (m)

k - Thermal conductivity of the material (W/mK)

I_h- Heating Intensity (W/m^2)

I_c- Cooling Intensity (W/m^2)

h_y - Semi- length of the laser spot in y direction (m)

c_y - Semi- length of the waterjet spot in y direction (m)

h_x - Semi- width of the laser spot in x direction (m)

c_x - Semi- width of the waterjet spot in x direction (m)

l_0 - Distance of separation between the laser spot and waterjet spot (m)

d - Thickness of the wafer (m)

h - Convective heat transfer coefficient (W/m^{2}K)

T_A - Ambient Temperature (K)

T_0 - Initial Temperature (K)

a_s - absorptivity

P – Laser power (W)

b – Laser spot size (m)

a – Crack depth (m)

yb – Length of the heating/cooling region along y direction (m)

xa – Semi-width of the heating/ cooling region along x+/x- direction (m)

H - Heaviside function

δ - Dirac delta function

θ - Green's solution for temperature distribution

ω - Eigen functions along x direction

ξ - Eigen functions along y direction

Ψ - Eigen functions along z direction

n - Index number for Eigen values along x direction

m - Index number for Eigen values along y direction

l - Index number for Eigen values along z direction

Φ - Airy stress function

D - Bending rigidity per unit length (N-m)

w_d - out of plane displacement in the z direction (m)

σ_{xx} - Normal stress component along x direction (N/m^2)

σ_{zz} - Normal stress component along z direction (N/m^2)

σ_{xy} - Shear stress component in the x-z plane (N/m^2)

N_x - Normal force per unit length along x direction (N)

N_y – Normal force per unit length along y direction (N)

N_{xy} - Shear force per unit length in the x-z plane (N)

K_{IC} - Critical stress intensity factor (MPa$\sqrt{m}$)

K_I - Stress intensity factor for Mode – I crack loading (MPa$\sqrt{m}$)

G_c - Critical Griffith Energy release rate (MPa-m)

G_t - Griffith Energy release rate for channeling crack (MPa-m)

4.2. INTRODUCTION

Yttria partially stabilized zirconia (Y-PSZ) is a structural and electronic ceramic which finds numerous industrial applications due to its high dielectric constant, chemical stability, low thermal conductivity and high fracture toughness. The yttria stabilizer helps in retaining the tetragonal phase of zirconia at room temperature. The retained tetragonal phase undergoes monoclinic transformation under external applied stress. The volume expansion associated with the transformation and the compressive stress generated in the vicinity of the crack arrests crack propagation, resulting in transformation toughening [1, 2]. Transformation toughened Y-PSZ is used for wide range of industrial applications such as thermal barrier coatings [3, 4]; electrodes in solid oxide fuel cells (SOFC) [5]; replacement for silica as gate oxides in ULSI (Ultra – Large Scale Integration) chips [6]; and as restorative dental materials [1].

Due to its high strength and toughness, machining of PSZ by grinding processes is difficult and costly [7]. The grinding processes result in sub-surface damages adversely affecting the strength of the finished substrate [8]. Therefore a number of researchers have investigated non-conventional machining of PSZ. Pfefferkorn and co-authors [9] reported a hybrid laser assisted machining (LAM) of PSZ that utilizes a continuous wave CO_2 laser to heat the substrate locally and lower its strength and conventional lathe for easier and faster turning operation. However, this hybrid machining technique is only suitable for cylindrical substrates with the temperature at the laser heating zone have to be maintained between 1000° C and 1200° C for optimal specific energy required to yield plastic deformation and to avoid uncontrolled crack formation. Kuar and his coworkers [10] investigated laser drilling through controlled ablation using Nd:YAG laser for micro drilling. However to the best of our knowledge, there are no reported studies of machining processes for profile cutting of Y-PSZ substrates.

The low thermal shock resistance of PSZ makes it an ideal candidate for hybrid laser/water-jet (LWJ) cutting through controlled crack propagation [11-14]. During LWJ cutting schematically represented in

Figure 4.1, a laser beam traverses along a predetermined path leading to localized heating of the workpiece and the waterjet trails the laser spot inducing rapid quenching of the heated material. In low conductive materials such as Y-PSZ, rapid quenching of the surface layers leads to development of large tensile stresses and propagation of cracks along the cutting path. Appropriate selection of processing parameters such as laser power, cutting speed etc. are required to ensure that crack propagation results in controlled separation of workpiece instead of either scribing or uncontrolled fracture [15].

In this work, we report analytical solutions for the temperature and stress fields induced on the Y-PSZ workpiece during hybrid LWJ cutting. These solutions are utilized to devise a process map that relates processing parameters to different machining modes of the workpiece. LWJ cutting experiments were performed for a range of processing parameters and cut surfaces were analyzed using X-ray photoelectron spectroscopy (XPS) and X-ray diffraction (XRD) analysis to investigate the contribution of phase and chemical transformation to crack growth and material separation. Experimental results were compared to process map predictions in order to validate the modeling assumptions underlying the theoretical analysis.

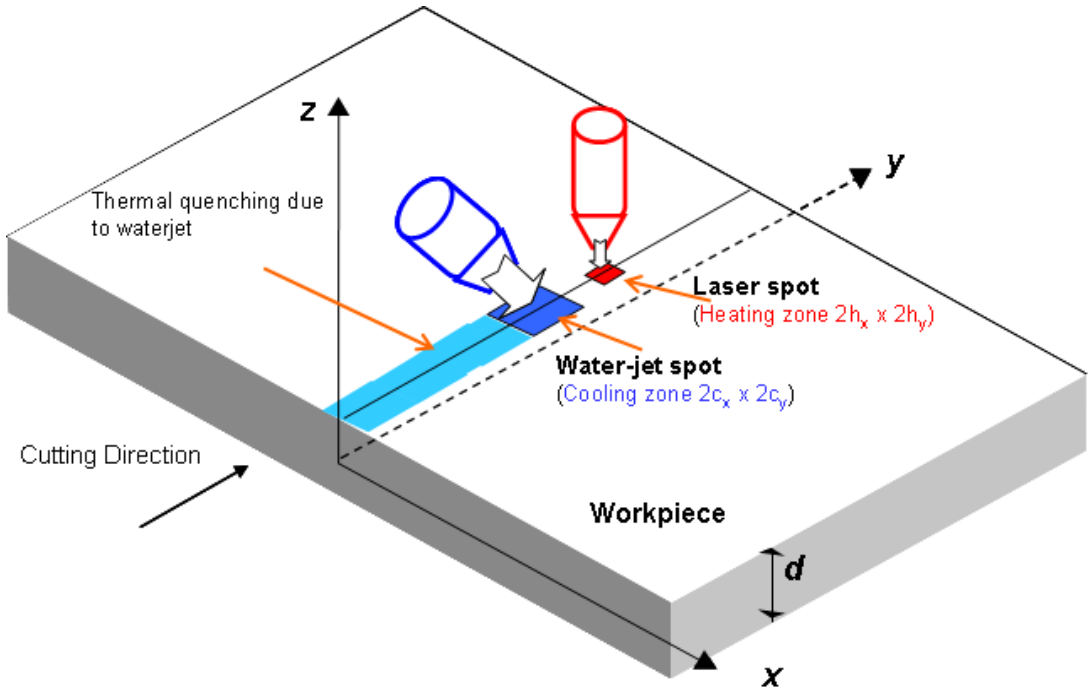

Figure 4.1: Schematic of Laser/Waterjet system

4.3. RELATIONSHIP BETWEEN LWJ PROCESS PARAMETERS AND FRACTURE CHARCTERISTICS OF THE WORKPIECE

4.3.1. Calculation of Thermal Stresses and Crack Driving Forces

The schematic of the laser/water-jet machining processes is shown in Figure 4.1. Green's function based approach is used to determine the solution of the heat conduction equation. The thermal stresses were determined from the temperature distribution using quasi-static thin plate analysis [16] and were used to determine the driving forces for cracks that lead to material separation.

4.3.1.1. Determination of temperature distribution

The temperature distributions at different points on the workpiece during LWJ cutting were determined from Fourier's Heat conduction equation with a source term as stated in Eqn (1).

$$c_p \rho \frac{\partial T}{dt} = k\nabla^2 T + q\left(x, y, t, I_h, I_c\right) \qquad \text{Eqn (1)}$$

where

$$\begin{aligned} q\left(x, y, t, I_h, I_c\right) = {} & I_h \mathrm{H}\left(h_x - |x|\right)\left[\mathrm{H}\left(vt - y\right) - \mathrm{H}\left(vt - y - 2h_y\right)\right] \\ & - I_c \mathrm{H}\left(c_x - |x|\right)\left[\mathrm{H}\left(vt - 2h_y - l_0 - y\right) - \mathrm{H}\left(vt - 2h_y - l_0 - 2c_y - y\right)\right] \end{aligned} \qquad \text{Eqn (2a)}$$

and

$$I_h = a_s \frac{4P}{\pi b^2} \qquad \text{Eqn (2b)}$$

The absorptivity a_s was calculated by taking into account of the various losses such as losses due to reflection and transmission of the laser light by the material, losses in the laser optics, losses due to heat emission of the material and losses due to the partial absorption of laser light by water vapor during machining, The cooling intensity I_c was calculated as the maximum cooling intensity that will force the temperature at the cooling spot to reach near room temperature [15].

Laser heating and waterjet cooling takes place on the top surface while minimal heat transfer takes place on the bottom surface [15]. Hence, the top surface of the workpiece was subjected to convective heat transfer while the bottom surface was modeled as insulated surface. The side walls were modeled as convective boundaries except y = 0 mm which was modeled as an insulated surface to simplify the analytical solution. The initial and boundary conditions for the system can be thus defined as follows:

$$k\frac{\partial T}{\partial z}_{z=d/2} = k\frac{\partial T}{\partial x}_{x=\pm xa} = k\frac{\partial T}{\partial y}_{y=yb} = -h\left(T - T_A\right)$$

$$\frac{\partial T}{\partial z}_{z=-d/2} = \frac{\partial T}{\partial y}_{y=0} = 0 \quad \left(\text{Insulated Boundary Condition}\right) \qquad \text{Eqn (3)}$$

$$T\left(x, y, z, t=0\right) = T_0$$

The transient temperature distribution was determined using a Green's function approach

$$T\left(x,y,z,t\right) = \int_0^t \int_0^{yb} \int_{-xa}^{xa} q\left(x_0, y_0, t_0, I_h, I_c\right)\theta\left(x, x_0, y, y_0, z, t, t_0\right)\, dx_0\; dy_0\; dt_0 + T_0 \qquad \text{Eqn (4)}$$

where $\theta(x, x_0, y, y_0, z, t, t_0)$ is the solution to the associated problem with similar boundary conditions,

$$c_p\rho\frac{\partial\theta}{dt} = k\nabla^2\theta + \delta\left(x - x_0\right)\delta\left(y - y_0\right)\delta\left(z - \frac{d}{2}\right)\delta\left(t - t_0\right) . \qquad \text{Eqn (5)}$$

Eigen function expansions along x, y, z coordinates were utilized to determine the series representation of Green's function θ.

$$\theta\left(x, x_0, y, y_0, z, t, t_0\right) = \frac{\kappa}{k}\sum_{n=1}^{\infty} exp\left(-\kappa\omega_n^2\left(t - t_0\right)\right)cos\left(\omega_n x\right)cos\left(\omega_n x_0\right)\cdot$$

$$\sum_{m=1}^{\infty} exp\left(-\kappa\xi_m^2\left(t - t_0\right)\right)cos\left(\xi_m y\right)cos\left(\xi_m y_0\right)\cdot \qquad \text{Eqn (6)}$$

$$\sum_{l=1}^{\infty} exp\left(-\kappa\psi_l^2\left(t - t_0\right)\right)cos\left(\psi_l d\right)cos\left(\psi_l\left(z + d/2\right)\right)\cdot \mathsf{H}\left(t - t_0\right)$$

4.3.1.2. Determination of thermal stresses

Non-uniform heating and cooling leads to development of thermal stresses in the specimen [16]. As the thickness of the workpiece was small in comparison to its length and width, uncoupled quasistatic thin plate analysis was used to determine the resulting displacements and thermal stress fields. Stress function and out-of-plane displacement fields need to satisfy the following differential equations and stress free boundary conditions.

$$\nabla^4 \Phi = -\nabla^2 N_T \qquad \text{Eqn (7)}$$

$$D\nabla^4 w_d = -\frac{1}{(1-\upsilon)}\nabla^2 M_T \qquad \text{Eqn (8)}$$

where the bending rigidity per unit length is $D = \frac{1}{12(1-\upsilon^2)} Ed^3$ Eqn (9)

Temperature distribution across the thickness determines the forcing terms in the above equations:

$$N_T = \alpha E \int_{-d/2}^{d/2} T \, dz \qquad \text{Eqn (10)}$$

$$M_T = \alpha E \int_{-d/2}^{d/2} z \, T \, dz \qquad \text{Eqn (11)}$$

Stress function and out-of-plane displacement fields were also expressed as an Eigen function expansion. When the heat source and cooling zone were at sufficient distance from the workpiece boundaries, the stress free boundary conditions were exactly satisfied because the temperature field was localized near the processing zone and insignificantly small near the boundaries. Hence, the solutions for stress function and out-of-plane displacements are given by:

$$\Phi = \alpha E \frac{1}{\omega_m^2 + \xi_n^2} \int_{-d/2}^{d/2} T \, dz \qquad \text{Eqn (12)}$$

$$w_d = \alpha E \frac{\omega_m^2 + \nu \xi_n^2}{\omega_m^2 + \xi_n^2} \int_{-d/2}^{d/2} z \, T \, dz \qquad \text{Eqn (13)}$$

The stress component (σ_{xx}) along the x axis that results in opening or closing of cracks is given in Eqn (14). Similar analysis may be utilized to calculate the other components of stress.

$$\sigma_{xx} = \frac{1}{1-\upsilon}\left(-\alpha E T + \frac{1}{d}\left((1-\upsilon) N_x + N_T\right)\right) - \frac{12 z D}{d^3}\left(\frac{\partial^2 w_d}{\partial x^2} + \frac{\partial^2 w_d}{\partial y^2}\right) \qquad \text{Eqn (14)}$$

The in-plane forces per unit lengths in the above expressions were determined from the stress function as follows:

$$N_x = \frac{\partial^2 \Phi}{\partial y^2}; \; N_{xy} = -\frac{\partial^2 \Phi}{\partial x \partial y}; \; N_y = \frac{\partial^2 \Phi}{\partial x^2} \qquad \text{Eqn (15)}$$

It is important to note that this solution for stress distribution is only valid for the cases when laser and waterjet spots are away from the workpiece boundaries and in this paper, it has only been used to determine the driving forces for cracks away from the boundaries. Further, the temperature and stress distributions were determined under the assumption that only the surface layers of material under the laser spot undergo melting, vaporization, and solidification and the localized material change does not influence the stress and temperature fields in the rest of the workpiece.

4.3.2. Prediction of Cutting Parameters

4.3.2.1. Crack Configurations considered for material separation

During LWJ machining, points along the cutting path were first irradiated by laser and subsequently quenched by the waterjet. Laser irradiation not only heats the surface but it also causes localized damage that results in crack nucleation and propagation during the waterjet quenching. During waterjet

quenching, laser induced damage can result into two possible crack configurations – edge crack towards center of plate or channeling crack along the surface – schematically represented in Figure 4.2. Crack propagation analysis depends on whether the LWJ cutting is initiated at the edge of the workpiece or in the middle of the workpiece. At the beginning of a through-cut, laser radiation is incident over the specimen boundary resulting in damage and subsequent cracking across the whole thickness during waterjet quenching. Therefore, equilibrium depth of a channeling crack is most appropriate for approximating the LWJ induced cut depth in thin through-cut specimens. However in the cases where cut starts away from the boundary, LWJ machining may be represented through a two step analysis: at the beginning of the cut when there are no pre-existing cracks in the workpiece, plain strain analysis of edge crack may be utilized to approximate the initial cut depth and subsequently, analysis of the channeling crack may be utilized to approximate the propagation of the initiated cut along the laser path. In the present paper, the case of through-cut thin Y-PSZ workpieces was considered and the energy release rates for channeling cracks were computed similar to previous studies [17-19].

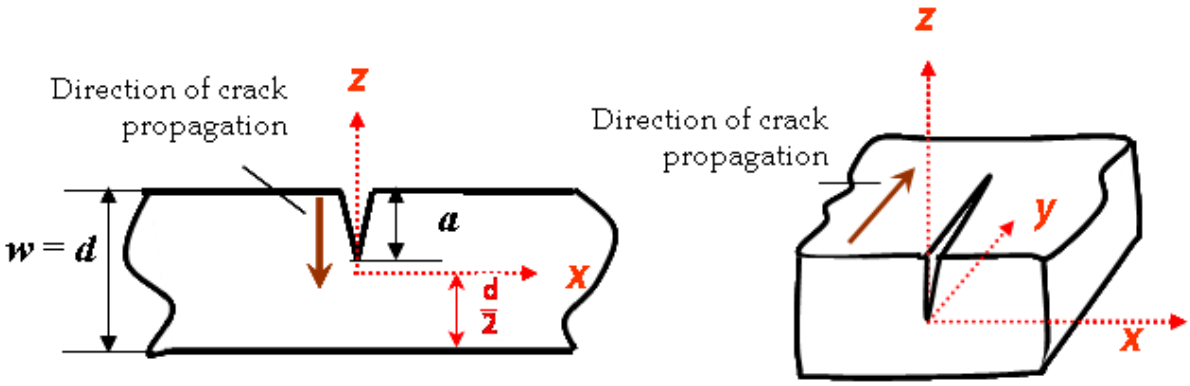

Figure 4. 2 (a): Plane strain cracking **(b): Crack Channeling**

4.3.2.2. Griffith Energy predictions for different crack lengths

The channeling of an edge crack is a three dimensional process and for steady state crack extension, it is assumed that edge crack will channel at fixed depth, with a constant tip shape and constant release rate. Hence, driving force for a steady state crack growth is determined from average energy release rate over the depth of the channeling crack front. The Griffith Energy release rate is calculated from stress intensity

factor corresponding to channeling cracks of different crack depths according to the following procedure: first, the stress intensity factors are computed using the weight function method for Mode I loading of crack in the *x*-*z* plane [18]. The weight functions for different crack lengths were computed using commercial finite element package ABAQUS (Providence, RI). Subsequently, the Griffith Energy release rate for crack channeling (G_t) is computed as:

$$G_t = \frac{1}{a}\int_0^a \frac{\left(K_I(a')\right)^2}{E}\,da' \qquad \text{Eqn (16)}$$

Computed energy release rates are compared to the critical energy release rate for Y-PSZ to determine the equilibrium depth of channeling crack propagated during LWJ machining.

4.4. MATERIALS AND EXPERIMENTAL PROCEDURES

4.4.1. Material and Optical Characterization

Y-PSZ samples of 25 mm x 25 mm x 1 mm thickness were procured from Coorstek, USA. The reflectance and transmittivity were characterized to determine the absorptivity of the material at the machining laser wavelength. The optical characterization of the samples were performed by Bruker make IFS 66 v/s Fourier Transform - Infra red (FT-IR) Spectrophotometer over wavelengths ranging from 2.5 µm to 25 µm.

4.4.2. LWJ Cutting Experiments

Cutting experiments were performed using a continuous wave CO_2 laser (Spectra Physics 800) of 10.6 µm wavelength with a CNC controlled worktable. The laser head was modified to accommodate waterjet (will be referred as LWJ cutting head, hereafter) to focus both laser beam and waterjet on the workpiece fixed on a CNC controlled work table. The design has been discussed in detailed in a previous publication [15]. A waterjet pressure of 3.5 MPa (500 psi) was used in the experiment. An air pressure of 35 kPa (5 psi) was maintained through the laser head to protect the lens from spatter. The experiment was conducted for two laser powers of 400 W and 600 W. The velocity of the laser cutting head was varied from 21.17 mm/s (50 inch/min) to 46.67 mm/s (110 inch/min).

4.4.3. Chemical and Structural Analysis

Cut surfaces and heat affected zones of machined workpieces was studied by Joel JSM 606LV Scanning Electron Microscopy at an acceleration voltage of 2-5 kV. Crystal lattices were analyzed with the help of Siemens D-500 X-ray diffractometer (Siemens, Madison, WI) operated with monochromatized Cu *K*α radiation at 50 kV and 20 mA. The measurements were made in reflection mode. Chemical compositions of the surface layers in the machined workpiece were analyzed by X-ray Photoelectron Spectroscopy (a multitechnique chamber Perkin-Elmer Model 5500) with PHI-ACCESS software. During the XPS analysis, the base pressures of the chamber was maintained at or lower than 1.03 x 10^{-7} Pa (8 × 10^{-10} Torr). An X-ray source of monochromatized Al *K* α radiation at a power of 250 W and take-off angle of 45 ° was used in these experiments.

4.5. RESULTS AND DISCUSSION

Numerical analysis was used to identify processing parameters that correspond to controlled separation of Y-PSZ workpieces. Transient temperature and stress distributions were evaluated for a range of process parameters. In the analytical model, quantities such as specimen dimensions, cutting velocity, laser spot size, water-jet area, separation between laser beam and water-jet were chosen to exactly match the experimental conditions. Material properties used for Y-PSZ specimens are given in Table 4.1 and are assumed to be temperature independent. Intensity of the heat flux incident over laser spot was determined from Eqn (2b). The value of absorptivity in the Eqn (2b) was calculated to be a_s = 0.70 i.e. 70% of the laser incident energy is absorbed in the sample based on approximating various losses during machining namely 5% losses in laser optics [15], 5% losses for reflectivity (as shown in Figure 4.3 corresponding to the CO_2 laser wavelength of 10.6 μm), 4% losses for emissivity [20] and 20% losses due to the absorption of laser light by water vapor [13, 15].

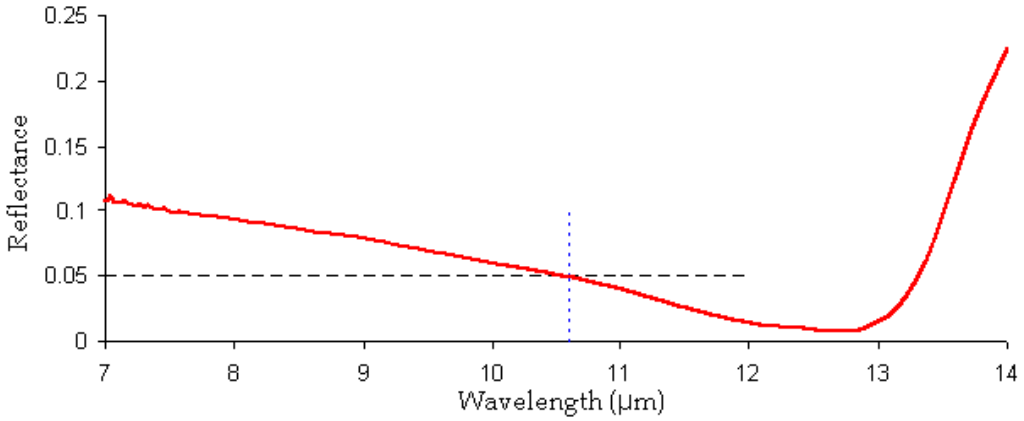

Figure 4.3: Reflectance spectrum of Y-PSZ

In the numerical model, waterjet quenching of the laser heated area is approximated using a heat sink along with convective cooling over the top surface because the large temperature variation over the sample generates non-uniform convection involving both forced convection due to water flow as well as pool boiling over the cutting path (water vapor/mist formation was observed during the experiments). The cooling intensity of heat sink and convection heat transfer coefficient were estimated using the following two assumptions: 1) waterjet quenching will rapidly reduce the temperature of laser heated area to room temperature; and 2) flow of water over the sample will result in forced convection (with coefficient value of 10,000 W/m^{2}K [21]).

Stress distribution was computed for the specimen size and stress free boundary conditions using 50 Eigen values along x and z axis and 400 Eigen values along y axis. Number of Eigen values along each direction was chosen on the basis of numerical convergence studies to ensure that increase in the number of Eigen values produces an insignificant change in the predictions of maximum tensile stress on the surface during waterjet quenching. The stress profiles at three different depths (top, center, and bottom) are plotted with respect to time for laser power of 600 W and cutting velocity of 29.6 mm/s (70 inch/min) in Figure 4.4. Arrival of laser spot on the top surface leads to rapid heating and development of compressive stresses. Quenching of the laser heated area with the waterjet results in development of large tensile stresses on the top surface while the middle and bottom surface are relatively unstressed. Through-

the-thickness stress distribution at the instance of maximum tensile stress on top surface is plotted in the inset shown in Figure 4.4(b). This large in-plane tensile stress will result in propagation of cracks that lead to scribing or splitting of the specimen.

Our solution approach for both temperature and stress calculation relies on summation of Eigen functions for temperature and stress computations. Number of Eigen values along each direction was chosen on the basis of numerical convergence studies to ensure that increase in the number of Eigen values produces an insignificant change in the predictions of maximum tensile stress on the surface during waterjet quenching. Eigen function expansion provides a simple form for the temperature and stresses but suffers from very slow convergence in resolving large gradients associated with changes in sign of surface heat flux from laser heating to waterjet cooling. The slow rate of convergence leads to wavy profile for the stress between the laser heating and subsequent cooling. Increasing the number of Eigen functions in the temperature and stress calculations lead to smoother curves but leads to extremely large computational times. However, the increase in Eigen values has no effect on the magnitude of maximum tensile stress that occurs away from this undulating profile. Since the focus of this paper was to determine the crack propagation driven by the maximum tensile stress, convergence studies were based on the magnitude of maximum tensile stress rather than the shape of overall stress variations.

Table 4.1: Properties of Y-PSZ considered in the analysis

Density	Thermal Conductivity	Specific Heat Capacity	Young's Modulus of Elasticity	Thermal diffusivity	Fracture Toughness	Thermal expansion coefficient
6050 kg/m³ (Coorstek 2008)	2.2 W/mK (Coorstek 2008)	650 J/kgK (Taylor et al. 1999)	210 GPa (Coorstek 2008)	5.594 x 10^{-7} m²/s	13 MPa√m (Coorstek 2008)	10.3 x 10^{-6} /K (Coorstek 2008)

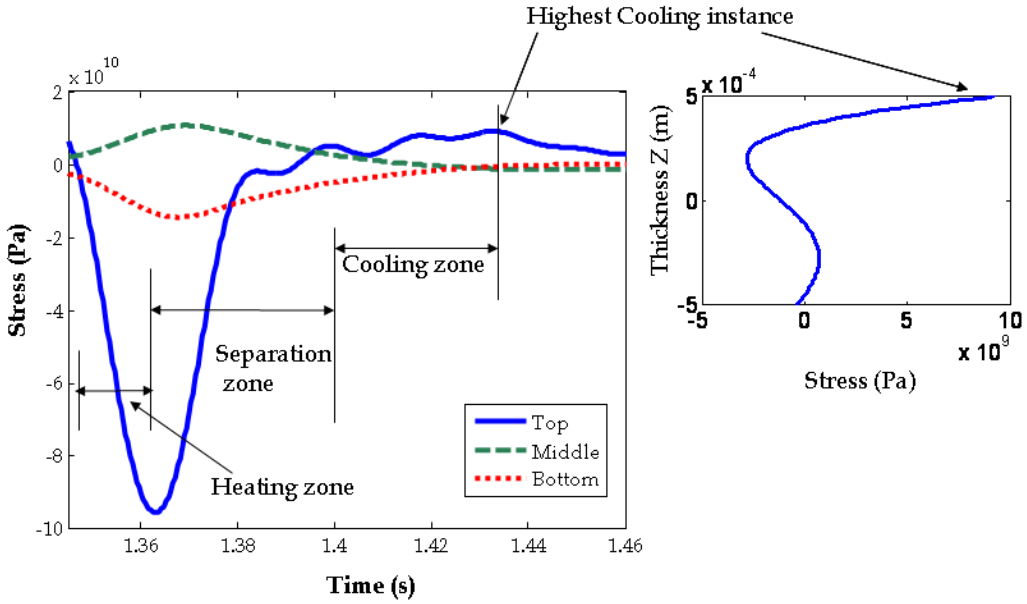

Figure 4.4: (a) Uncoupled quasi-static thermal stress plot at three different depths z = d/2, 0 & -d/2) at x = 0 and y = 0.04 m with respect to time with the inset (b) showing the stress plot across the thickness at the highest stress instance.

Ratio of the two prime machining parameters i.e laser power and velocity is cumulatively represented as line energy (expressed in J/mm) for laser machining. Comparison of numerical predictions for different combinations of laser power and cutting velocity showed that the predicted temperature and thermal stresses were approximately same for a fixed line energy value. Our previous investigations on alumina specimens have also shown that similar material separation pattern or fracture behavior was observed for a fixed line energy value [15, 22, 23]. Hence for the sake of brevity, all the results are presented as a function of line energy rather than different laser power and cutting velocity values.

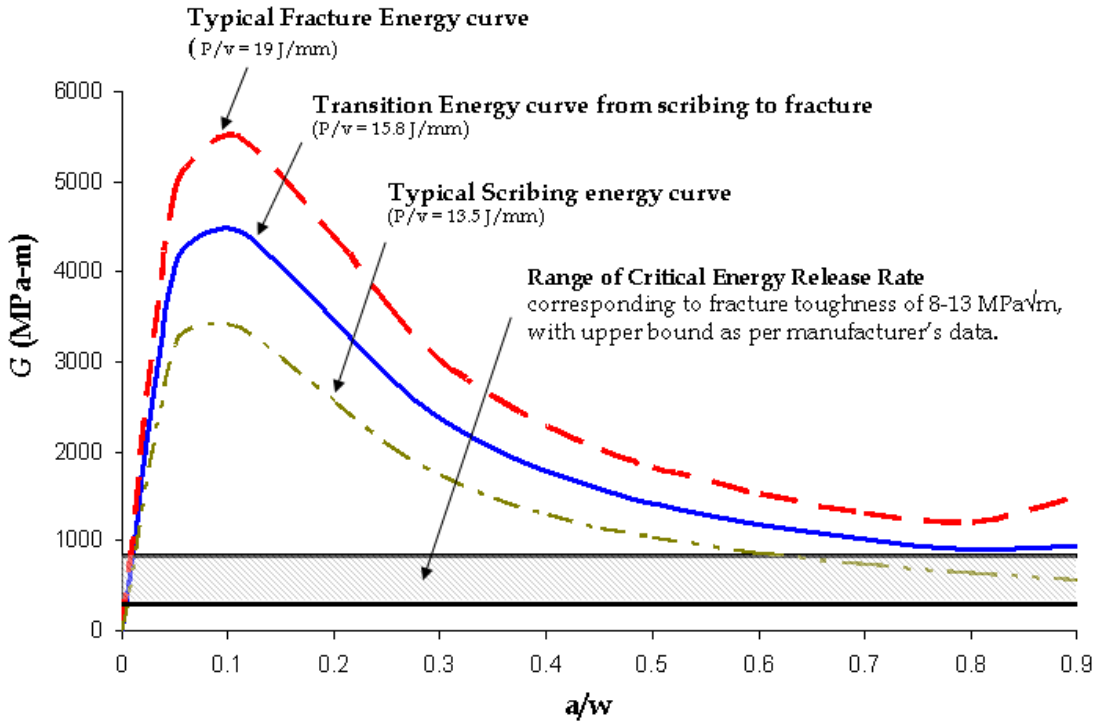

Figure 4.5: Plot of G (Griffith Energy) Vs. a/w graph for various line energies

Predicted stress histories shown in Figure 4.4 were used to calculate the driving forces for plane strain and channeling crack configurations. Crack driving forces reach the maximum at the instant when the top surface was subjected to maximum tensile stress during waterjet quenching (shown in Figure 4.4 (b)). The computed energy release rates for channeling cracks at this maximum tensile stress instant are plotted as a function of crack length for three different processing parameters in Figure 4.5. In all the cases, energy release rates were highest for cracks that are approximately 0.1 times the thickness due to the large tensile stresses induced on the top surface during quenching. Energy release rates decreases as the cracks becomes longer and reach a minimum for cracks that were roughly 0.6 to 0.7 times the thickness due to the compressive stresses induced in the middle portion of material (Figure 4.4 (b)). In addition, increase in line energy leads to increase in computed values of energy release rates.

Numerical predictions of energy release rates were also compared to Y-PSZ's critical energy release rate (G_c) (Figure 4.5) to estimate the equilibrium depth of the channeling crack. For line energy values below 15.8 J/mm, G_t for short cracks was greater than G_c but for cracks approximately 0.6- 0.7 times the thickness

G_t was lower than G_c and as a result, scribing with different crack depths was expected for line energy lower than 15.8 J/mm. As the line energy values are further increased, the G_t value for all crack lengths becomes greater than G_c resulting in channeling of through-the-thickness cracks. Therefore, line energy greater than 15.8 J/mm are expected to result in material separation through controlled crack propagation.

4.5.1. Cutting Experiment Results

The laser/waterjet cutting experiments were performed for a range of processing parameters and the samples were categorized into two machining modes - scribing and material separation. The modes of machining observed at different line energies are plotted in Figure 4.6. LWJ machining resulted in scribing over a wide range of line energy values and a transition from scribing to controlled separation at line energy values between 18 and 20 J/mm was observed. The lowest line energy which yielded material separation was 18.9 J/mm.

SEM images of the top view of the scribed sample and the cut cross section of the through-cut separated sample are presented in Figure 4.7 (a) and (b), respectively. Both images show localized recast zones along the laser path. In the top view, a number of small lateral cracks can be observed in the recast zone. As shown in Figure 4.7(b), two distinct zones were observed in all the cut surfaces: a recast zone near the top surface and a fracture zone through the rest of the thickness. Surface damage and size of the heat affected zones are primarily influenced by laser surface density (ratio of laser power by the product of spot size and cutting velocity). Hence the optimization of line energy and surface energy density can minimize the size of the recast zone and achieve material separation as shown in our earlier work on LWJ machining of alumina [15]. Conventional machining processes for Y-PSZ such as high speed deep grinding (HSDG)[24] result in formation of pits (during dry grinding) and sharp marks/cracks (during wet grinding) over the whole machined surface. In contrast, LWJ machining only results in localized recast zone at the top surface and can also achieve significantly higher cutting speeds than reported in grinding processes [24, 25] as well in other machining processes such as ultrasonic machining [26].

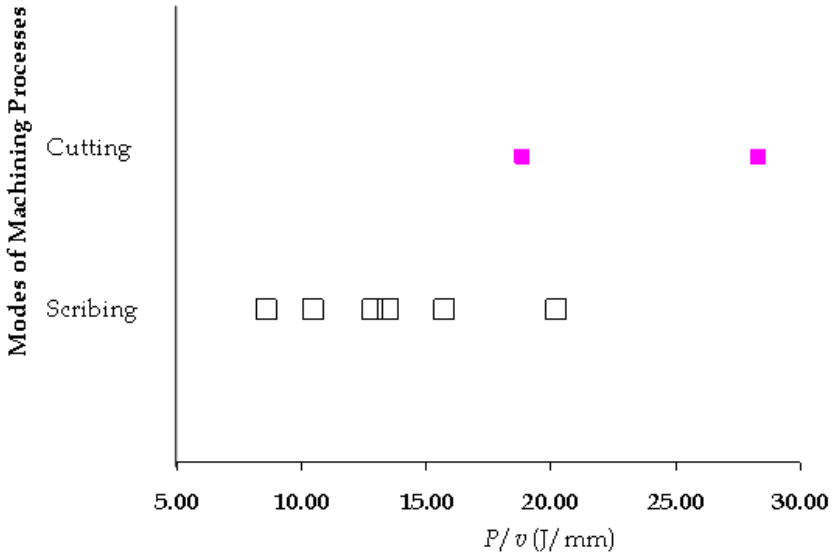

Figure 4.6: Observed fracture behavior as a function of line energy

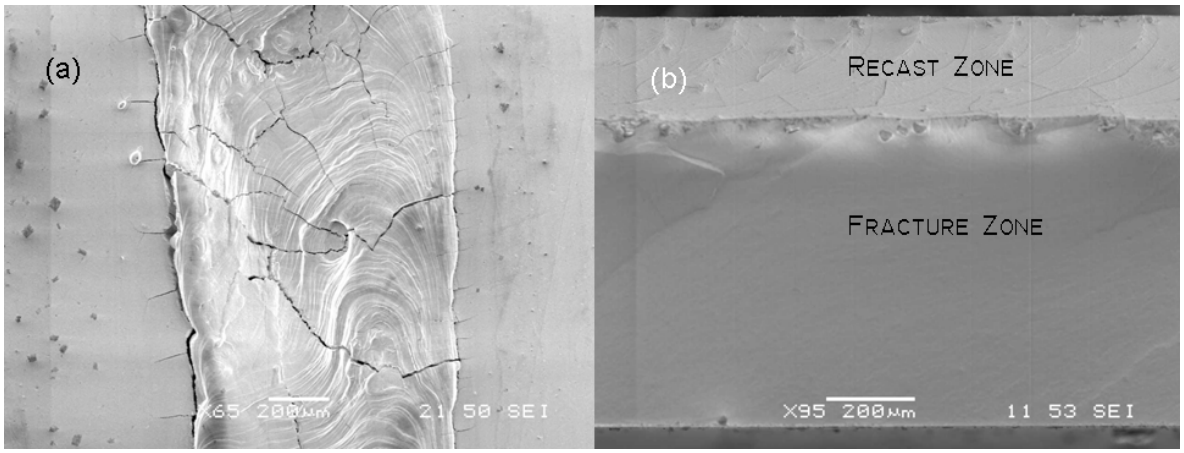

Figure 4.7 (a): SEM Image of laser/waterjet scribed sample (Top view). (b) SEM image of the cross-section of the LWJ cut surface

4.5.2. Structural and Chemical Analysis

Y-PSZ has a metastable tetragonal phase at ambient temperatures. In the mechanism of transformation toughening, the stresses at the crack tip transform the metastable tetragonal phase to monoclinic phase resulting in increase in volume of about 4-5% [1]. Volume increase leads to compressive stresses in the vicinity of the crack tip and thereby arresting crack propagation. X-ray diffraction (XRD) analyses of both the recast zone and substrate material were performed to identify the contribution of transformation toughening to crack propagation during LWJ machining. The XRD plot of the cut and as-received surfaces

are shown in Figure 4.8. The subscripts 't', '*m*' and '*c*' correspond to tetragonal, monoclinic, and cubic phases respectively. As shown in the XRD plot of the as-received surface, the Y-PSZ substrates were mainly composed of tetragonal lattice structure with little percentage of monoclinic and cubic forms [27]. No distinct changes were noticed between the XRD plot of the as-received and cut surfaces. Therefore it can be concluded that no significant lattice or phase transformation occurred during LWJ machining of Y-PSZ.

IIavsky et al [4] performed neutron diffraction studies on the phase transformation of PSZ during annealing and observed that the phase transformation occurs over significantly larger time intervals in the order of hours. Since LWJ machining of the workpiece takes place in less than a minute, phase transformation may not have taken place. In addition, the heating/cooling rates (on the order of 100's of K/sec) during the LWJ machining are in the "no transformation zones" of the time-temperature-transformation (TTT) curves for tetragonal-to-monoclinic martensitic transformation in Y-PSZ [28].

X-ray photoelectron spectroscopy spectra obtained on both recast as well as as-received surfaces are plotted in Figure 4.9 (a) and (b), respectively. The relative counts of all the constituent atoms - zirconium, oxygen and yttrium - are nearly identical at both the locations indicating that Y-PSZ substrates did not undergo any chemical transformation during the LWJ machining.

The metastability of zirconia in stress-generating surface treatments such as grinding and sand-blasting can trigger tetragonal to monoclinic transformation resulting not only in volume increase but also increasing the susceptibility for aging and altering the phase integrity [29]. Therefore LWJ machining processes that precludes phase and chemical transformation of Y-PSZ is advantageous in maintaining the integrity and strength of machined workpieces.

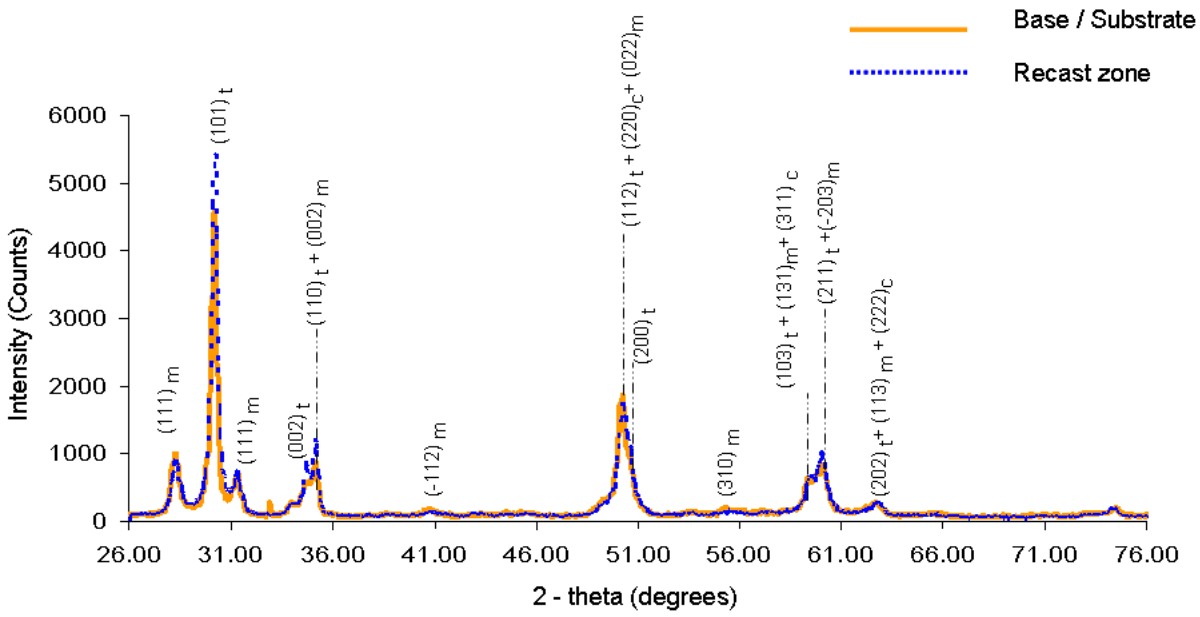

Figure 4.8: X-ray diffraction of the melt zone and substrate material

4.5.3. Comparison of LWJ machining predictions and observations

SEM, XRD and XPS analysis of cut surfaces clearly validates the modeling assumptions underlying the fracture mechanics of Y-PSZ machining that relates processing parameters to material separation. SEM images of the cut surfaces show characteristic fracture zones validating that material separation has taken place through crack propagation along the cutting path. Results of XRD and XPS analysis shows that Y-PSZ specimens do not undergo phase or chemical transformations during LWJ machining respectively. Consequently, stress fields associated chemical or phase transformation [30] do not contribute to LWJ machining of Y-PSZ. Stress field generated during thermal shock are primarily responsible for crack propagation associated with material separation.

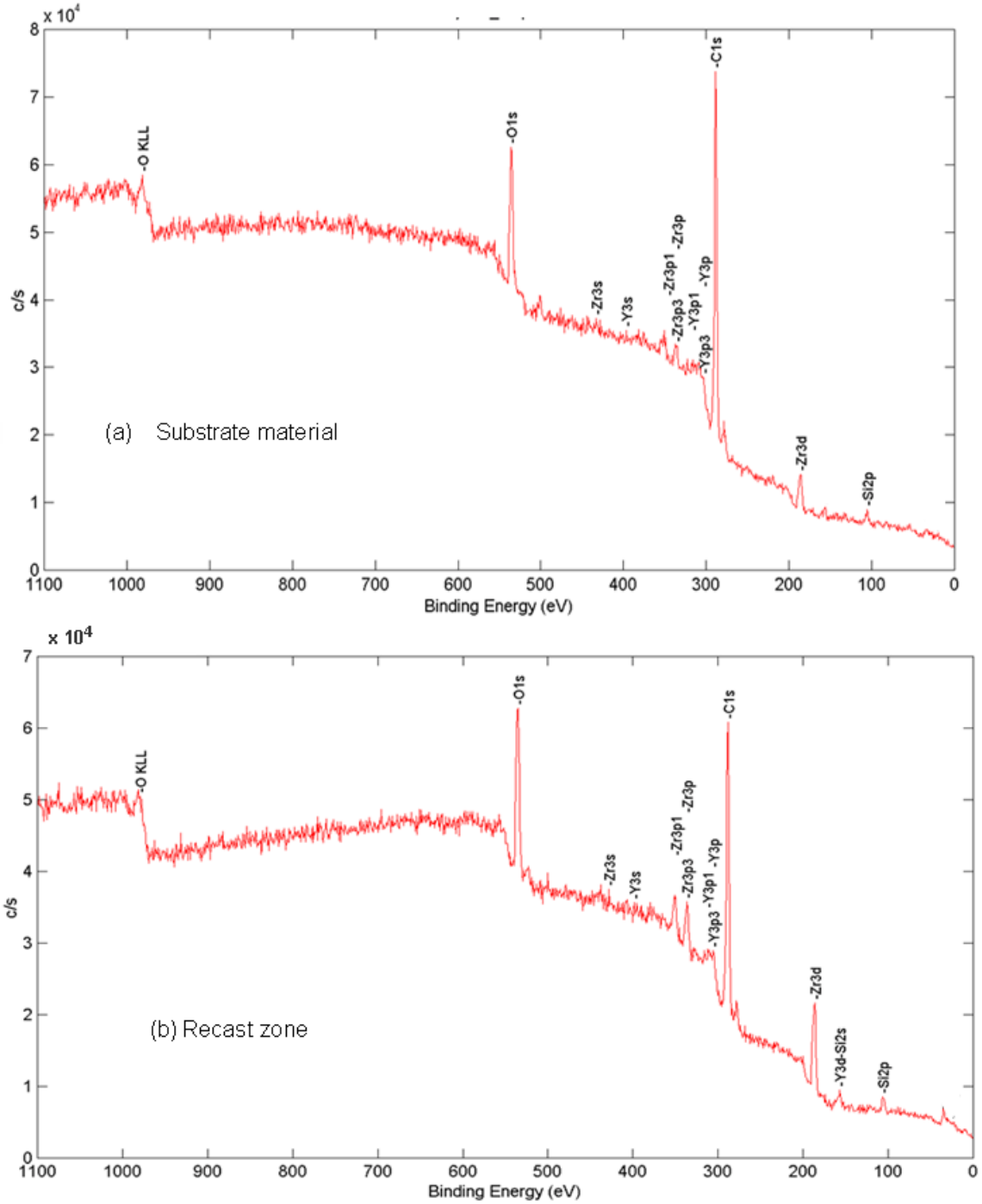

Figure 4.9: X-ray photoelectron spectrum of the substrate and melt zone

Results of the cutting experiments agree well with model prediction that increase in line energy will result in transition from scribing to material separation but the theoretical predictions for the exact value for

transition are slightly lower than that observed in cutting experiments. In the cutting experiments, transition from scribing to material separation was first observed at line energy of approximately 19 J/mm.

The analysis of channeling crack predicted that line energy equal to or higher than 16 J/mm would yield material separation. The small discrepancy between theoretical predictions and experimental observations may be attributed to two main sources: firstly, the temperature predictions are based on the assumption that localized melting of surface layers under the laser spot has no influence on heat conduction; and secondly, material properties are assumed to be temperature independent.

Localized melting of the surface layers (as observed in the experiments) may consume a small fraction of the incident laser energy and thus reduce the amount of energy conducted away from the heated area. As a result, higher magnitudes of incident power may be required for achieving the temperature and stress fields corresponding to crack propagation. The influence of localized melting may be incorporated into the temperature prediction through an empirical loss factor that reduces the amount of incident laser power. However, we have not included this into our theoretical analysis as the value of the loss of incident energy will depend on the magnitude of melting and can only be estimated through comparison between theoretical predictions and experimental observations. More importantly, the localized melting during the LWJ machining is not desirable and optimization of machining parameters is required such that localized melting can be minimized or eliminated.

The temperature, stress and crack propagation predictions are based on material properties reported in manufacturers' datasheets [31] and material handbooks [32]. In order to obtain analytical solutions of governing equations, the material properties are assumed to be temperature independent. The influence of this assumption is evident by considering the influence of changing the numerical value for the coefficient of thermal expansion (CTE). Theoretical predictions are based on Y-PSZ CTE value of 10.3×10^{-6} / K as reported in manufacturer's datasheet. However, the CTE of Y-PSZ is temperature dependent and its value ranges from 6 to 10.5×10^{-6} / K for temperatures between 200 and 1000 K as reported by Hayashi

et al. [33]. The predicted line energy values for transition from scribing to material separation would coincide with experimental observations if an average thermal coefficient of expansion of 8.25 x 10^{-6} / K was used in the calculations. Incorporating the temperature dependence of material properties into temperature and stress predictions will overcome this limitation but will require numerical approaches such as finite element analysis for solution of the governing equations [34]. In the current work, we have assumed temperature independent properties to obtain analytical solutions so that the influence of different processing parameters on the LWJ machining can be investigated rapidly without large computational expenses.

4.6. CONCLUSIONS

A combined theoretical and experimental investigation of single line LWJ cutting was performed to relate the processing parameters to the different modes of machining of Y-PSZ workpiece. Theoretical analysis of crack propagation suggested that LWJ machining of Y-PSZ substrate would result in different modes of machining that transition from scribing to material separation with increase in line energy values. Critical value of laser line energy corresponding to transition from scribing to cracking agreed well with experimental observations. Analysis of the Y-PSZ cut surfaces validated the modeling assumptions that thermal shock stresses are primarily responsible for crack propagation and material separation during LWJ machining. LWJ machining results in cut surfaces that are free from phase or chemically transformed materials. The validation of the modeling assumptions and close agreement between predicted and measured line energy values clearly indicates that analytical stress analysis of crack propagation captures the essential mechanisms underlying material separation during LWJ machining of Y-PSZ and can be effectively used to predict the different modes of machining for other processing parameters.

Acknowledgements

The authors gratefully acknowledge the financial support for this research provided by the U.S. National Science Foundation under the grant DMI – 0522788. The authors would also like to thank: Mr. James

Anderegg, Ames Laboratory, DOE, Ames, IA for XPS measurement, Mr. Seo In-seok, Department of Material Science, Iowa State University, Ames, IA for optical characterization and Mr. Scott Schlorholtz, Materials Analysis Research Lab, Iowa State University, Ames, IA for XRD measurement.

4.7. REFERENCES

[1] I. Denry and J. R. Kelly, "State of the art of zirconia for dental applications," Dental Materials, vol. 24, pp. 299-307, 2008.

[2] R. C. Garvie and P. S. Nicholson, "Phase Analysis in Zirconia Systems," Journal of the American Ceramic Society, vol. 55, pp. 303-305, 1972.

[3] A. G. Evans, D. R. Mumm, J. W. Hutchinson, G. H. Meier, and F. S. Pettit, "Mechanisms controlling the durability of thermal barrier coatings," Progress in Materials Science, vol. 46, pp. 505-553, 2001.

[4] J. Ilavsky, J. K. Stalick, and J. Wallace, "Thermal spray yttria-stabilized zirconia phase changes during annealing," Journal of Thermal Spray Technology, vol. 10, pp. 497-501, 2001.

[5] C. C. Wei and K. Li, "Yttria-stabilized zirconia (YSZ)-based hollow fiber solid oxide fuel cells," Industrial & Engineering Chemistry Research, vol. 47, pp. 1506-1512, 2008.

[6] Y. Zhou, N. Kojima, and K. Sasaki, "Growth and dielectric properties of tetragonal ZrO2 films by limited reaction sputtering," Journal of Physics D-Applied Physics, vol. 41, 2008.

[7] S. Malkin and T. W. Hwang, "Grinding Mechanisms for Ceramics," CIRP Annals - Manufacturing Technology, vol. 45, pp. 569-580, 1996.

[8] T. Kosmac, C. Oblak, P. Jevnikar, N. Funduk, and L. Marion, "Strength and reliability of surface treated Y-TZP dental ceramics," Journal of Biomedical Materials Research, vol. 53, pp. 304-313, 2000.

[9] F. E. Pfefferkorn, Y. G. Shin, Y. G. Tian, and F. P. Incropera, "Laser-assisted machining of magnesia-partially-stabilized zirconia," Journal of Manufacturing Science and Engineering-Transactions of the ASME, vol. 126, pp. 42-51, 2004.

[10] A. S. Kuar, B. Doloi, and B. Bhattacharyya, "Modelling and analysis of pulsed Nd : YAG laser machining characteristics during micro-drilling of zirconia (ZrO2)," International Journal of Machine Tools & Manufacture, vol. 46, pp. 1301-1310, 2006.

[11] A. Gilbert, K. Kokini, and S. Sankarasubramanian, "Thermal fracture of zirconia-mullite composite thermal barrier coatings under thermal shock: An experimental study," Surface & Coatings Technology, vol. 202, pp. 2152-2161, 2008.

[12] T. J. Lu and N. A. Fleck, "The thermal shock resistance of solids," Acta Materialia, vol. 46, pp. 4755-4768, 1998.

[13] C. Barnes, P. Shrotriya, and P. Molian, "Water-assisted laser thermal shock machining of alumina," International Journal of Machine Tools & Manufacture, vol. 47, pp. 1864-1874, 2007.

[14] C. Barnes, P. Shrotriya, and P. Molian, "A Hybrid Laser/Water-Jet Cutting Process for Brittle Materials," presented at ASME, NAMRC-34, 2006.

[15] D. Kalyanasundaram, G. Shehata, C. Neumann, P. Shrotriya, and P. Molian, "Design and validation of a hybrid laser/water-jet machining system for brittle materials," Journal of Laser Applications, vol. 20, pp. 127-134, 2008.

[16] B. A. Boley and J. H. Weiner, Theory of Thermal Stresses. Mineola, New York: Dover Publications, Inc., 1997.

[17] D. Kalyanasundaram, P. Shrotriya, and P. Molian, "Obtaining a relationship between Process parameters and Fracture energy for CO2 Laser/Waterjet Machining of Ceramics," Journal of Engineering Materials and Technology, vol. 131, pp. 011005-10, 2009.

[18] H. Tada, Paris, P.C., and Irwin, G.R., Stress Analysis of Cracks Handbook. St, Louis: Del Research, MI, 1985.

[19] L. G. Zhao, T. J. Lu, and N. A. Fleck, "Crack channelling and spalling in a plate due to thermal shock loading," Journal of the Mechanics and Physics of Solids, vol. 48, pp. 867-897, 2000.

[20] F. E. Pfefferkorn, "Laser-Assisted Machining of Zirconia Ceramics," in Mechanical Engineering, vol. PhD. West Lafayette: Purdue University, 2002, pp. 414.

[21] M. F. Ashby, Materials Selection in Mechanical Design. Oxford, England: Butterworth-Heinemann, 2001.

[22] D. Kalyanasundaram, J. Wille, P. Shrotriya, and P. Molian, "CO2 Laser/Waterjet machining of Polycrystalline Cubic Boron Nitride," presented at ASME, NAMRC -36 2008.

[23] W. Steen, Laser Materials Processing, 3rd Edition ed: Springer, 2003.

[24] G. Z. Xie and H. Huang, "An experimental investigation of temperature in high speed deep grinding of partially stabilized zirconia," International Journal of Machine Tools and Manufacture, vol. 48, pp. 1562-1568, 2008.

[25] H. Huang and Y. C. Liu, "Experimental investigations of machining characteristics and removal mechanisms of advanced ceramics in high speed deep grinding," International Journal of Machine Tools & Manufacture, vol. 43, pp. 811-823, 2003.

[26] P. L. Guzzo, A. H. Shinohara, and A. A. Raslan, "A comparative study on ultrasonic machining of hard and brittle materials," Journal of the Brazilian Society of Mechanical Sciences and Engineering, vol. 26, pp. 56-61, 2004.

[27] J. Ilavsky and J. K. Stalick, "Phase composition and its changes during annealing of plasma-sprayed YSZ," Surface & Coatings Technology, vol. 127, pp. 120-129, 2000.

[28] H. Tsubakino and N. Matsuura, "Relationship between transformation temperature and time-temperature-transformation curves of tetragonal-to-monoclinic martensitic transformation in zirconia-yttria system," Journal of the American Ceramic Society, vol. 85, pp. 2102-2106, 2002.

[29] S. Deville, J. Chevalier, and L. Gremillard, "Influence of surface finish and residual stresses on the ageing sensitivity of biomedical grade zirconia," Biomaterials, vol. 27, pp. 2186-2192, 2006.

[30] R. Molian, P. Shrotriya, and P. Molian, "Thermal stress fracture mode of CO2 laser cutting of aluminum nitride " International Journal of Advanced Manufacturing Technology, 2007.

[31] Coorstek, "Zirconia - YTZP," 2008.

[32] M. M. Gauthier, ASM Handbook Volume 02: Properties and Selection: Nonferrous Alloys and Special-Purpose Materials. Materials Park, OH: ASM International, 1995.

[33] H. Hayashi, T. Saitou, N. Maruyama, H. Inaba, K. Kawamura, and M. Mori, "Thermal expansion coefficient of yttria stabilized zirconia for various yttria contents," Solid State Ionics, vol. 176, pp. 613-619, 2005.

[34] K. Li and P. Sheng, "Plane-Stress Model for Fracture of Ceramics During Laser Cutting," International Journal of Machine Tools & Manufacture, vol. 35, pp. 1493-1506, 1995.

Appendix - A

Weight Function Method

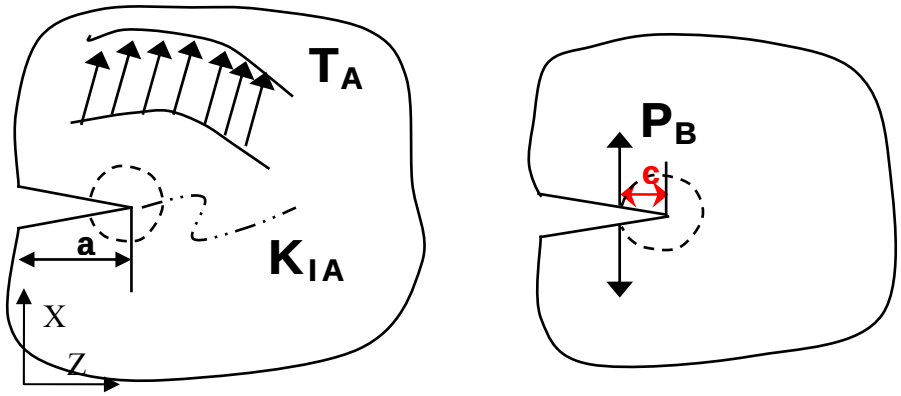

FigureA: Given state of stress and the reciprocal state of stress

The approach is based on reciprocal theorem, wherein the given state of far field traction forces T_A acting on the body yielding a displacement u_A is evaluated against a point load P_B acting on the crack face and producing a displacement u_B. According to the theorem, the ratio of load to displacement would remain constant. On the assumption that the distance 'c' (distance between the point of action of load P_B and the crack tip) in the latter case is very small (i.e., approaching zero compared with other dimensions), the displacement u_A will be well within the crack-tip stress field and is given by

$$u_A = \left(\frac{4\sqrt{2}}{\sqrt{\pi} E'} K_{IA} \sqrt{c} \right) \quad \text{-- Eqn (1)}$$

Rearranging them to get stress intensity factor

$$K_{IA} = \frac{E'\sqrt{\pi}}{4\sqrt{2} P_B \sqrt{c}} \int T_A u_B ds \quad \text{-- Eqn (2)}$$

As the value of 'c' approaches zero (i.e towards the crack tip), $P_B\sqrt{c}$ approaches a constant value, say πB_I. The near tip Bueckner's displacement fields for plane strain [17] for Mode I loading are given below.

$$u_z = \frac{B_I}{G\sqrt{r}} \cos\left(\frac{\theta}{2}\right)\left[2\upsilon - 1 + \sin\left(\frac{\theta}{2}\right)\sin\left(\frac{3\theta}{2}\right)\right] \quad \text{-- Eqn (3-a)}$$

$$u_x = \frac{B_I}{G\sqrt{r}} \sin\left(\frac{\theta}{2}\right)\left[2 - 2\upsilon - \cos\left(\frac{\theta}{2}\right)\cos\left(\frac{3\theta}{2}\right)\right] \quad \text{-- Eqn (3-b)}$$

For a small radii of singularity considered, the displacements in the region at various angles can be computed. Given Bueckner's displacements in the circle of singularity, the displacements u_B on the crack face at various depths can be computed by finite element technique and hence K_{IA} be computed.

CHAPTER 5. UNDERSTANDING THERMO-CHEMICAL MACHINING OF POLYCRYSTALLINE DIAMOND BY HYBRID LASER/WATERJET SYSTEM

(A paper for submission to Acta Materialia)

Dinesh Kalyanasundaram, Andea Schmidt, Pranav Shrotriya, and Pal Molian

Department of Mechanical Engineering

Laboratory for Lasers, MEMS, and Nanotechnology

Iowa State University, Ames, IA 50011

5.1. ABSTRACT

A model has been developed to understand and estimate the fracture mechanism during laser/waterjet machining of polycrystalline diamond (PCD). Cobalt, the binder material in PCD helps in the phase transformation of diamond to diamond-like carbon and graphite during laser heating. This transformation results in an increase of volume that imitates a wedge effect. The controlled fracture of the substrate observed during machining is a result of tensile stresses due to quenching of laser heated zone by waterjet combined with the wedge effect due to phase transformation. Raman microspectroscopy of the cut surfaces was performed to confirm the transformation of diamond. The model has been devised to estimate both the phase transformation stress intensity factor of diamond and the thermal stresses. Also, the experimental results indicate that LWJ machining system can accomplish cutting of PCD substrates with good quality of cut and at higher cutting speeds in comparison to other machining processes.

Key words: Thermo-chemical machining, Crack propagation, Polycrystalline diamond (PCD), Laser/Waterjet Machining (LWJ), diamond to graphite transformation, Griffith Energy, Cut quality

5.2. INTRODUCTION

PCD is an excellent tool material due to its high strength (~400 MPa), high hardness (~70 GPa), and high scratch and wear resistance (~ 10 in Mohls scale). Polycrystalline diamond (PCD) tools are widely used to machine engineering materials like ceramics, graphite epoxy composites, wood and plastics with capabilities of achieving high machining rates and finer surface finishes [1]. They are also used in oil field and geological applications [2]. PCD tools are available in two forms: a supported or composite tool in form of thin layers of PCD backed on a cemented carbide substrate [1] and the other is unsupported or self-supported tool consisting of polycrystalline diamond [3].

PCD compacts are produced by consolidation of diamond powders at high pressures and temperatures with cobalt as sintering aid/binder phase [3]. Other binder phases include nickel [4] and magnesium carbonate [5, 6]. PCD has a typical mean grain size from 4 to 25 μm depending on the binder and sintering temperature [7]. Typically, PCD is stable up to about 700°C [7] and removing the metal binder will extend the stability up to 1200°C [7].

The excellent property of high strength and high wear resistance constrains machining or shaping of PCD substrates. Tool inserts are cut from the compact blanks by electric discharge machining (EDM) [4, 8-10] and Nd:YAG laser cutting [1] and are finished either by chemo-mechanical etching [11] or by high temperature lapping [12] or by dynamic friction polishing [13, 14]. The main requirements of a manufacturing process in cutting the desired geometry of tool inserts are: capabilities to generate a smooth surface, minimal heat affected zone and higher cutting speed.

In the cutting processes discussed above, material removal is accomplished by erosion of material either under electrical discharge or laser heating. The binder material cobalt facilitates both the processes. In EDM machining cobalt enhances the electrical conductivity of PCD [8] while in laser machining cobalt increases

the absorptivity of the laser light in the infrared regime [15]. The presence of cobalt not only facilitates machining through erosion but also enhances the graphitization of diamond [6]. In the current work, we investigate a novel material removal mechanism for controlled fracture of PCD. Laser/waterjet machining (LWJ) [16-19] system is used in the cutting process that exploits the phase transformation of diamond. Material separation is achieved by a three step process: (i) Localized heating by laser results in transformation of diamond (ii) Localized cooling by waterjet induces thermal stresses of tensile nature (iii) Tensile stresses along with the volume increase due to transformation (causing a wedge effect) results in material separation.

The rate of machining is one of the important manufacturing aspects. Harrison *et al* [1] has investigated laser machining of PCD composite (thin layer of PCD on WC substrate) using Q-switched Nd:YAG laser at an average power of 420 W at repetition rates of 3-50 kHz and pulse durations of 20 to 200 ns. The highest machining speed obtained was 36 mm/min. "Melt, Burn and Blow" type of cutting mechanism was reported. While the tungsten carbide (WC) substrate is capable of melting, the diamond layer underwent phase transformation to graphite [20]. Laser-microjet® [21] developed by Swiss Federal Institute of Technology allows precise cutting of PCD materials by employing a Q-switched pulsed laser at an average power of 300 W at 532 nm wavelength and water pressure of 2-10 MPa. However, the process suffers from slow cutting speeds of 72 mm/min for 0.5 mm thick PCD substrate. The material removal rate by EDG and EDM is much slower than the laser based techniques. Typical values of material removal rate reported for EDM and EDG are 9 mm^3/hr [9] and 2 mm^3/min [8] respectively. Higher rates of machinability can be achieved by LWJ system and are discussed in the paper.

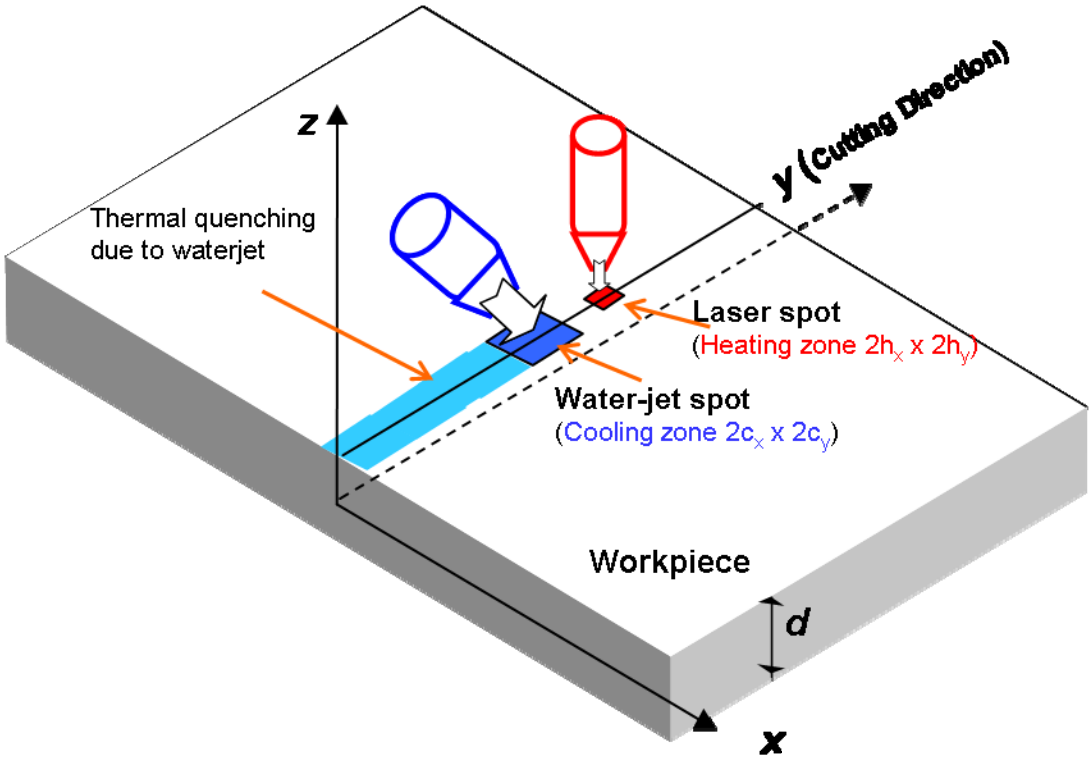

Figure 5.1: Schematic of the LWJ system

A hybrid machining process of CO_2 laser/waterjet (LWJ) machining that has been developed and applied in the machining of electronic ceramics such as aluminum oxide [17, 18], polycrystalline cubic boron nitride (PCBN) [16], and aluminum nitride [19]. In this hybrid process, the laser head has been modified to accommodate the low-pressure water jet (< 7 MPa (1000psi)). The design and fabrication of CO_2 – LWJ has been explained in detail elsewhere [17] and for the sake of brevity, the schematic of the process is presented in Figure 5.1Figure 5.. PCD machining by both CO_2 laser and CO_2 laser/waterjet (LWJ) system has been attempted in this work. Based on our previous results for PCBN [16] we hypothesize that localized heating of PCD will lead to transformation of diamond to graphite or diamond-like carbon. Volume expansion associated with this transformation will lead to wedge effect and subsequent crack propagation leading to fracture of the workpiece. A model has been developed to relate the processing parameters, fracture characteristics and thermo-chemical transformation of PCD substrates. Finally, a process map relating laser parameters (laser power and cutting velocity) and fracture characteristics is presented.

5.3. EXPERIMENTAL METHODS AND CUTTING PARAMETERS

PCD blanks with 8% cobalt as a binder of mean grain size of 4-5 µm were procured from Diamond Innovations, Worthington, Ohio, USA for the experiments. The blanks were 0.5 mm thick wafer of 3" diameter. The surface roughness of the received samples was 1.0 µm Ra and 1.3 µm RMS.

A continuous wave CO_2 Laser (Model 820 Spectra Physics) of 10.6 µm wavelength and 1.5 kW rated power was used for all the experiments. The laser beam was focused to a spot size of 0.2 mm diameter on the sample surface. Air flow at a pressure of 69 kPa (10 psi) was maintained during experiments to protect the lens from damage due to spatter. For the laser/waterjet experiments, the water jet trailed the laser beam with a spacing of a about 2-4 mm to avoid the absorption of laser power by direct contact with water [17, 22].

Two sets of straight-line cutting experiments were conducted. The first set of experiments were carried with laser alone and the second set of experiments were carried out with laser/waterjet system. In the first set of experiments, the objective was to find the threshold power and velocity required to machine the 0.5 mm thick disc of PCD. Experiments were performed for different powers ranging from 200 W to 1000 W in steps of 200 W. Nitrogen was used as assist gas to prevent oxidation. The velocity was varied from 21.16 mm/s (50 inch/min) to 1083 mm/s (250 inch/min). In the second set of experiments single-pass cutting with Laser/Waterjet (LWJ) was carried out. The laser power was maintained at 1000 W and the velocity of cutting was varied between 21.16 mm/s (50 inch/min) and 63.48 mm/s (150 inch/min) to determine the threshold velocity of cutting for LWJ experiments. The waterjet was maintained at a pressure of 3.5 MPa (500 psi) and the distance between the laser spot and the waterjet spot was maintained at approximately 3.4 mm.

The cut surfaces were examined by Raman microspectroscopy (at a wavelength of 488 nm), and optical profilometery to identify the chemical transformation and measure roughness respectively. Cut surfaces

and heat affected zones of machined workpieces were studied by Joel JSM 606LV Scanning Electron Microscopy at an acceleration voltage of 2-5 kV.

5.4. FRACTURE ANALYSIS

The calculation of temperature distribution and the corresponding thermoelastic stresses that occur during machining are discussed in this section. A relationship between the calculated Griffith Energy and the modes of crack propagation to effect material separation has been developed in this section.

5.4.1. Temperature distribution

Green's function based approach was used to predict the temperature fields during both laser and laser/water-jet machining operations. Temperature distribution, $T(x,y,z,t)$, in the workpiece was determined by modeling the laser and water-jet as rectangular source and sink [23], respectively as shown schematically in Figure 5.1. Transient temperature distributions were obtained by the solution of following diffusion equations

$$c_p \rho \frac{\partial T}{dt} = k\nabla^2 T + q\left(x,y,t,I_h,I_c\right) \qquad \text{Eqn (1)}$$

where c_p is the specific heat, ρ is the density of the material, T is the temperature field and $q(x, y, t, I_h, I_c)$ is the net heat input to the workpiece. The transient temperature distribution was determined using a Green's function approach as given by Eqn (2)

$$T(x,y,z,t) = \int_0^{\infty}\int_{-\infty}^{\infty}\int_0^{\infty} q\left(x_0,y_0,t_0,I_h,I_c\right)\theta\left(x,x_0,y,y_0,z,t,t_0\right).dy_0.dx_0.dt_0 + T_0 \qquad \text{Eqn (2)}$$

where $\theta\left(x,x_0,y,y_0,z,t,t_0\right)$ is the solution to the associated problem given by

$$c_p \rho \frac{\partial T}{dt} = k\nabla^2 T + \delta\left(x-x_0\right)\delta\left(y-y_0\right)\delta\left(z-\frac{d}{2}\right)\delta\left(t-t_0\right) \qquad \text{Eqn (3)}$$

where d is the thickness of the workpiece material, I_h is the heating intensity (W/m^2), and I_c is the cooling intensity (W/m^2) . Convective boundary conditions were used on the top surface where both laser heating

and cooling takes place as well as on the workpiece edges (x = ± xa and y = yb). Insulated boundary conditions were assumed on the bottom surface (z = -d/2) and on the starting edge (y = 0).

It is important to note that Green's function for this problem can be represented as a series of error functions or trigonometric functions. The error function representation accurately captures the steep gradients associated with transient heat source and sink for short time intervals but has slow convergence in matching the boundary conditions. On the other hand Eigen or the trigonometric function representation matches the boundary condition exactly, but has slow convergence in capturing the steep gradients associated with short duration transient response. We have utilized an hybrid approach for determining thermal solutions: error function representation for short duration and trigonometric series based Eigen function expansion for long duration when the gradients are not steep and can be captured with reasonable number of terms (<500). Error function representation of the solution is given by

$$T(x,y,z,t)=\frac{1}{4kd}\int_0^t\sum_{i=1}^{n}(Q_h\text{-}Q_c)\,A_i Cos\,\xi_i\;Cos\left(\xi_i\left(\frac{1}{2}+\frac{z}{d}\right)\right)exp\left(\frac{-\xi_i^2\sqrt{\kappa(t\text{-}t_0)}}{d^2}\right)dt_0\;+T_0$$

Eqn (4)

where Q_h, Q_c, A_i, a, ξ_i *and* T_0 are given by

$$Q_h=\frac{I_h\kappa}{4}\left\{erf\left[\frac{x+h_x}{2\sqrt{\kappa(t-t_0)}}\right]-erf\left[\frac{x-h_x}{2\sqrt{\kappa(t-t_0)}}\right]\right\}\left\{erf\left[\frac{y+vt_0}{2\sqrt{\kappa(t-t_0)}}\right]-erf\left[\frac{y-vt_0}{2\sqrt{\kappa(t-t_0)}}\right]\right\}$$

Eqn (5a)

$$Q_c=\frac{I_c\kappa}{4}\left\{erf\left[\frac{x+c_x}{2\sqrt{\kappa(t-t_0)}}\right]-erf\left[\frac{x-c_x}{2\sqrt{\kappa(t-t_0)}}\right]\right\}\ldots$$

$$\ldots\ldots\left\{erf\left[\frac{y+vt_0-2h_y-l_0}{2\sqrt{\kappa(t-t_0)}}\right]-erf\left[\frac{y-vt_0-2h_y-l_0-2c_y}{2\sqrt{\kappa(t-t_0)}}\right]\right\}$$

Eqn (5b)

Here κ represents thermal diffusivity and ξ_i represents Eigen values of the characteristic equation, $\xi_i\ tan\xi_i = Bi$ where Bi represents Biot number.

The value of the coefficients

$$A_i = 2\left(\frac{\xi_i^2 + Bi^2}{\xi_i^2 + Bi^2 + Bi}\right) \quad \text{Eqn (6)}$$

and heating intensity

$$I_h = a_s \frac{4P}{\pi b^2} \quad \text{Eqn (7)}$$

where P and b are the laser power (W) and laser spot size (m) respectively. The cooling intensity I_c of the waterjet is the maximum intensity that would cool the workpiece to near room temperature [18]. The Eigen function solution of the associated problem has already been discussed in detail elsewhere [18]. The temperature modeling described above is based on heat diffusion and does not take into account of melting, evaporation, and its related effects.

5.4.2. Calculation of Thermal Stresses

Non-uniform heating and cooling of the specimen leads to development of thermal stresses in the specimen [24]. Uncoupled quasistatic thin plate analysis was used to determine the resulting thermal stress fields. Since the thickness of the wafer is thin in comparison to its length and width, a plane stress assumption was used in the mathematical model.

$$\sigma_{zz} = 0 = \sigma_{xz} = \sigma_{yz} \quad \text{Eqn (8)}$$

Stress function Φ and out-of-plane displacement fields wd satisfy the following differential equations and associated boundary conditions of stress free boundaries of the workpiece.

$$\nabla^4 \Phi = -\nabla^2 N_T \quad \text{Eqn (9)}$$

$$D\nabla^4 w_d = -\frac{1}{1-\upsilon}\nabla^2 M_T \quad \text{Eqn (10)}$$

where the bending rigidity per unit length,

$$D = \frac{1}{12\left(1 - \upsilon^2\right)} E d^3 \qquad \text{Eqn (11)}$$

Temperature distribution across the thickness determines the forcing terms in the above equations:

$$N_T = \alpha E \int_{-d/2}^{d/2} T \, dz \qquad \text{Eqn (12)}$$

$$M_T = \alpha E \int_{-d/2}^{d/2} z \, T \, dz \qquad \text{Eqn (13)}$$

Stress function and out-of-plane displacement fields are also expressed as an Eigen function expansion and the partial differential equations are reduced to algebraic equations and hence easily solved. When the heat source and cooling zone are at sufficient distance from the workpiece boundaries, the stress free boundary conditions are exactly satisfied because the temperature field is localized near the processing zone and insignificantly small near the boundaries. Hence, the solutions for stress function and out-of-plane displacements are given by:

$$\Phi = \alpha E \frac{1}{\omega_m^2 + \xi_n^2} \int_{-d/2}^{d/2} T \, dz \qquad \text{Eqn (14)}$$

$$w_d = \alpha E \frac{\omega_m^2 + \nu \xi_n^2}{\omega_m^2 + \xi_n^2} \int_{-d/2}^{d/2} z \, T \, dz \qquad \text{Eqn (15)}$$

The stress component (σxx) along the x axis that results in opening or closing of cracks is given in Eqn (16). Similar analysis may be utilized to calculate the other components of stress.

$$\sigma_{xx} = \frac{1}{1-\upsilon}\left(-\alpha E T + \frac{1}{d}\left(\left(1-\upsilon\right) N_x + N_T\right)\right) - \frac{12 z D}{d^3}\left(\frac{\partial^2 w_d}{\partial x^2} + \frac{\partial^2 w_d}{\partial y^2}\right) \qquad \text{Eqn (16)}$$

The in-plane forces per unit lengths in the above expressions are determined from the stress function as follows:

$$N_x = \frac{\partial^2 \Phi}{\partial y^2};\ N_{xy} = -\frac{\partial^2 \Phi}{\partial x \partial y};\ \ N_y = \frac{\partial^2 \Phi}{\partial x^2} \qquad \text{Eqn (17)}$$

It is important to note that this solution is only valid for the cases when laser and waterjet spots are away from the workpiece boundaries and in this paper, it has only been used to determine the driving forces for cracks away from the boundaries. Further, the temperature and stress distributions are determined under the assumption that only the surface layers of material under the laser spot undergo melting, vaporization, and solidification and the localized material change does not influence the stress and temperature fields in the rest of the workpiece.

5.4.3. Modes of Fracture and calculation of crack driving forces

Two different modes of crack propagation can result in material separation of the workpiece by thermal fracture [25, 26] namely plane strain cracking and channeling. In the plane strain crack propagation, Mode I edge crack travels towards the center of the plate while in channeling crack propagation, a stable Mode I crack travels along the length/width of the specimen as shown in Figure 5.2. These crack propagation modes are discussed in detail elsewhere [25, 26].

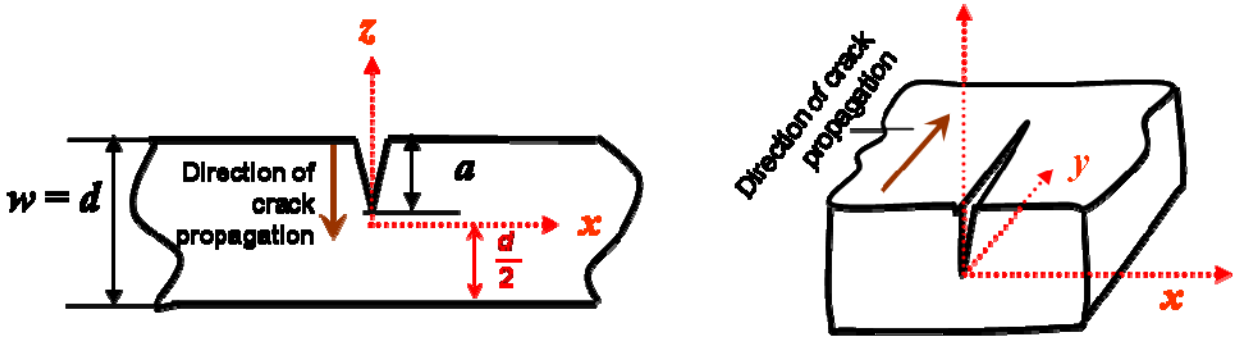

Figure 5.2: (a) Plane strain cracking **(b) Crack Channeling**

Machining can either start before/at the edge of the workpiece or inside the edge of the workpiece. And crack propagation analysis is dependent on the position of start of machining. In case of the former, the laser radiation is incident over the specimen boundary resulting in damage and subsequent cracking across the whole thickness during waterjet quenching. Therefore, equilibrium depth of a channeling crack is most appropriate for approximating the LWJ induced cut depth in thin through-cut specimens. However in the cases where cut starts away from the free edge or boundary, crack propagation analysis is represented by a two step process: plain strain analysis of edge crack is utilized to approximate the initial cut depth at the beginning of the cut (when there are no pre-existing cracks in the workpiece), and subsequently, channeling crack analysis is utilized to approximate the propagation of the initiated cut along the laser path. In the present paper, the case of through-cut thin PCD workpieces was considered and the stress intensity factor and energy release rates for channeling cracks are computed using weight-functions [18, 27]. The plane strain energy release rate G_p was calculated from the stress intensity factor K_I for mode I for different crack depths "a." The channeling energy release rate G_{ct} for an edge crack is obtained from the average energy release rate over the depth of the channeling front [25]. For a steady state crack extension, it is assumed that the crack will channel at fixed depth, with a constant tip shape and constant release rate. The Griffith Energy release rates for plain strain and channeling cracks are given by

$$G_{ct} = \frac{1}{a}\int_0^a \frac{\left(K_I(a')\right)^2}{E/\left(1-\upsilon^2\right)}da' \qquad \textbf{Eqn (18)}$$

where E is the young's modulus of PCD substrate, υ is the poisson's ratio and K_I is the intensity factor.

5.4.4. Effect of Transformation on crack propagation

The chemical transformation of the constituent compounds takes place during laser or laser/waterjet machining. This produces a wedge effect [28-30], if the transformed product has a higher volume than the substrate material. Therefore the chemical transformation will in turn help propagate cracks to yield material separation. We hypothesize that an increase in stress intensity factor due to transformation has aided the crack channeling energy to exceed the critical energy and the minimum transformational stress intensity factor can be calculated by iteration. Also, the stress intensity factor ahead of the crack tip can be

expressed as a function of material property (Young's modulus & poisson's ratio) and crack/material configuration (a– length of crack, w – thickness of the specimen and δ_l – crack mouth opening displacement). The relationship between crack mouth opening displacement (CMOD) (see Figure 5.3) and the stress intensity factor is given by Eqns (19) [31] and (20) [32] . Eqn (19) is a simplified form and has been used in the calculation of stress intensity factor for wedge induced cracking [31]. A detailed form of the relationship relating K_I, P (load) and δ_l (CMOD) is given by Eqn (20). The following assumptions were made in the calculation of the additional stress intensity factor K_I due to transformation: (i) CMOD increases proportionally by a factor $(a/w+0.64)^2$ for $0 \le a/w \le d_t$ (depth of transformation) or K_I is a constant and (ii) K_I decreases proportionally by a factor of $(a/w+0.64)^2$ for $d_t < a/w \le 0.9$.

$$K_I = \frac{\delta_l \sqrt{3} E/\left(1-v^2\right)}{2\sqrt{w}\left(a/w+0.64\right)^2} \qquad \text{------- Eqn (19)}$$

$$K_I = \frac{\delta_l V_1(a/w) E/\left(1-v^2\right)}{\sqrt{w} V_2(a/w)} \qquad \text{------ Eqn (20)}$$

where $V_1(\alpha) = (2+\alpha)(1-\alpha)^{-3/2}\left(0.886+4.64\alpha-13.32\alpha^2+14.72\alpha^3-5.6\alpha^4\right)$ -----Eqn (21a)

and $V_2(\alpha) = (1+\alpha)^2(1-\alpha)^{-2}\left(2.1630+12.219\alpha-20.065\alpha^2-0.9925\alpha^3+20.609\alpha^4-9.9314\alpha^5\right)$

------- Eqn (21b)

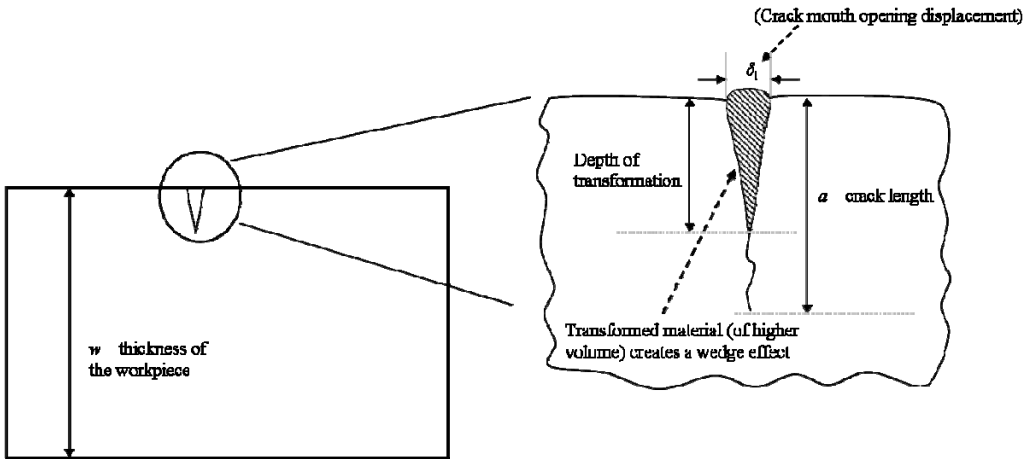

Figure 5.3: Transformational effect and CMOD

5.5. RESULTS AND DISCUSSION

5.5.1. Thermo-chemical Machining

In the first set of experiments, machining of PCD substrates were carried out with laser alone. It was found that the minimum laser power required to machine the material was 1000 W. It was shown previously that the different modes of laser/LWJ machining of alumina [17, 18] was a function of line energy (ratio of laser power to velocity of machining table). However, in the present case similar material separation was not noticed for the same line energy for laser powers less than 1000 W i.e. powers lower than 1000 W resulted in scribing while powers higher than 1000 W resulted in material separation. Hence an investigation for the actual cause of fracture was done. SEM images of the cut cross-section by laser and laser/waterjet is shown in Figure 5.4. Two distinct regions can be noticed from both the figures namely, a top zone resembling recast layer and the bottom zone resembling fractured zone. The depth of the transformed zone was measured to be 218 µm and 150 µm for laser and laser/waterjet cutting respectively.

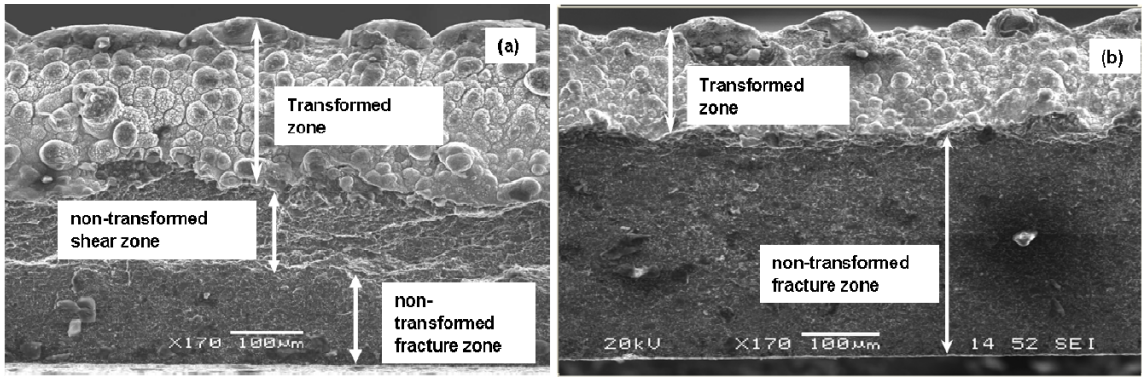

Figure 5.4: SEM image of the cross-section by (a) Laser cutting (b) LWJ cutting at 1000 W and at a velocity of 42.32 mm/s (100 inch/min)

Raman spectroscopy (Figure 5.4) of the cross section revealed diamond-like carbon and graphite on the top zone. Laser heating has thus transformed diamond to graphite and this transformation has helped in the material separation process (will be mathematically proven later). In other words, a thermal induced chemical transformation has helped in the material separation process, which is termed as thermo-chemical machining. It is reported that the metal binder (Co) also assists in the transformation of diamond to graphite [6]. In some cases it is believed that the carbon is dissolved in the metal binder and re-precipitated

as graphite while in other cases the metal particles may simply act as templates for the epitaxial growth of carbon [33]. A volume expansion is associated with the transformation of diamond to graphite. The lattice spacing of the two phases are 2.0 Å and 3.5 Å respectively [34] which corresponds to a maximum volume increase of diamond by 75% after complete graphitization.

5.5.2. Cut Quality Analysis

The cross-section of the laser and LWJ cut samples were analyzed using optical and scanning electron microscopes. As observed in the Figure 5.6, laser cutting produces three noticeable regions. The top layer is the graphite/diamond-like carbon layer as seen in the SEM image in Figure 5.6(a). The globules like structures are recast cobalt (binder). The middle layer shown in Figure 5.6(b) is a transition layer and depicts sheared surfaces. The bottom layer shown in Figure 5.6(c) is the fracture zone. However these sheared surfaces are often not present in the LWJ cutting compared to laser cutting.

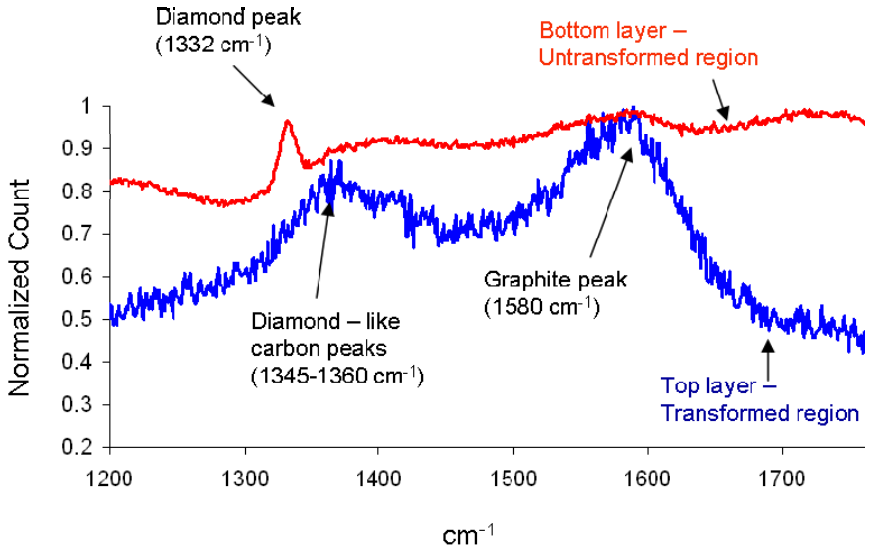

Figure 5.5: Raman spectroscopy of laser cutting of PCD

Surface roughness data of the different zones across the cross section are shown in the Table 5.1 & 5.2. The top zone became rougher with increasing cutting velocities. Higher percentage of graphitization has occurred at lower cutting velocity resulting in a smoother cut. However, the overall surface roughness

improved at higher cutting speeds since the transformed zone depth decreased (see Table 5.1). Similarly in LWJ cutting the net heat input is lower due to the presence of mist/water vapor in the air which is also confirmed by the lower absorptivity coefficient determined in the analysis as shown in section 3. Hence the top layer was rougher than laser cutting (see Table 5.2). For the same reason that the depth of transformed region was lower in LWJ, the overall surface roughness is better in LWJ machining than in laser machining. The surface roughness obtained in laser /LWJ processes is comparable to the surface roughness of 2 to 4 μm obtained in electrical discharge machining processes [8].

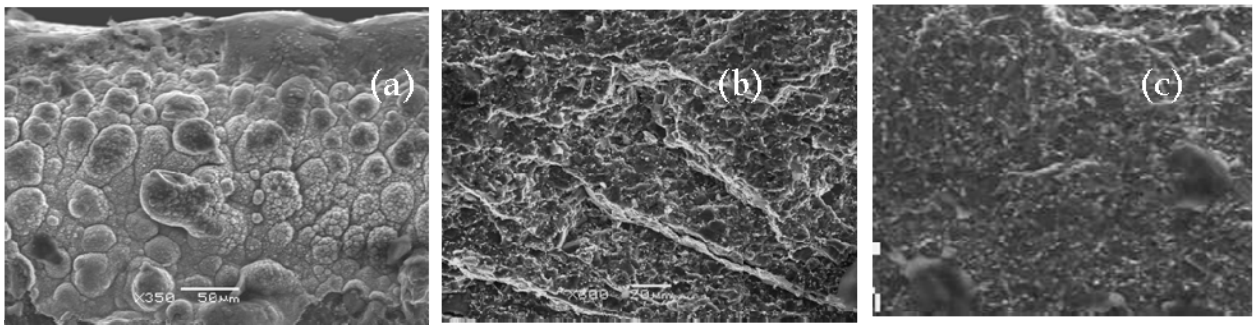

Figure 5.6: Analysis of the cut cross section by laser cutting at 1000 W and 42.32 mm/s (100 inch/min) (a) Top/graphitized zone (b) middle/transition zone and (c) bottom/fracture zone

Table 1: Surface Roughness Measurement of cut cross section by laser machining at different cutting speeds

Cutting Speed mm/s (inch/min)	Surface Roughness (Ra) Laser Cutting		
	Top Layer	Bottom Layer	Overall
42.43 (100)	5 μm	2 μm	12 μm
63.64 (150)	12 μm	2 μm	5 μm

Table 2: Surface Roughness Measurement of cut cross section by both laser and LWJ machining at a cutting speed of 42.32 mm/s (100 inch/min)

Surface Roughness (Ra) Laser Cutting			Surface Roughness (Ra) LWJ Cutting		
Top Layer	Bottom Layer	Overall	Top Layer	Bottom Layer	Overall
5 μm	2 μm	12 μm	7 μm	2 μm	7 μm

The maximum cutting speed reported previously by Nd:YAG laser cutting of PCD was 12.5 mm/min [1] at 420 W average powers while we have achieved maximum cutting speeds of 86.64 mm/s (2 m/min) and 43.32 mm/s (2.6 m/min) by CO_2 laser cutting and CO_2 laser/waterjet cutting respectively at 1000 W.

5.5.3. Modeling the effective absorptivity

Experimental observations of both laser and LWJ machining have led us to expect a poor absorptivity of the material at infrared regime. Graphitization of diamond which takes place during laser heating causes increased absorption of IR radiation. Modeling of this process complicates due to change (drastic increase) in the absorptivity during diamond graphitization. To model this effect, an effective absorptivity to represent the cumulative effect during the machining process was calculated by matching the temperature field at the transformed depth to the diamond-graphite transition temperature. The transition temperature has been reported to be affected by the presence of binder (Cobalt) [6]. Various temperatures ranging from 600°C – 700°C [6], 900°C [35], to 1200°C [36] have been reported as the diamond to graphite transition temperature. For the purpose of analysis we had considered 900°C as the transition temperature.

The temperatures at the transformed depth are matched to predict the absorptivity that can be used in the modeling. The depths of the transformed zone were measured from the SEM images. The temperature distribution across the thickness was plotted at the highest heating instance for both laser and LWJ machining (Figure 5.7) using the error function solution of the mathematical model. The material properties considered for the analysis are given in Table 5.3. The heating intensity was calculated from Eqn 6(b) for laser power of 1000 W and spot size of 0.2 mm. The cooling intensity for waterjet was chosen as the maximum intensity that can completely absorb all the heat from the material. In other words it is the intensity which can force the temperature on the surface of the material to near room temperature. The value of cooling intensity chosen for LWJ machining was 9.0×10^7 W/m^2. A maximum convective coefficient of 1×10^4 W/m^2 was used in the calculations [37]. The values of absorptivity for laser machining and LWJ machining are iterated to match the partial onset of diamond to graphite transition temperature with the transformed depth. The absorptivity for laser and LWJ machining were found to be 0.35 and 0.326 respectively. The low absorptivity and efficiency in LWJ machining is due to the presence of water vapor [17].

Table 3: Properties of PCD and Graphite Considered in the Analysis

Density	Thermal Conductivity	Specific Heat Capacity	Young's modulus		Thermal diffusivity	Thermal expansion coefficient		Fracture Toughness
			PCD	Graphite		PCD	Graphite	
4000 kg/m^3 [7]	600 W/mK [1]	500 J/kgK [38]	872.3 GPa	10 Gpa	3.0 x 10^{-4} m^2/s	8.86 x 10^{-6} (/K)[7]	4.5 x 10^{-6} (/K)	3-6 Mpa √m [39]

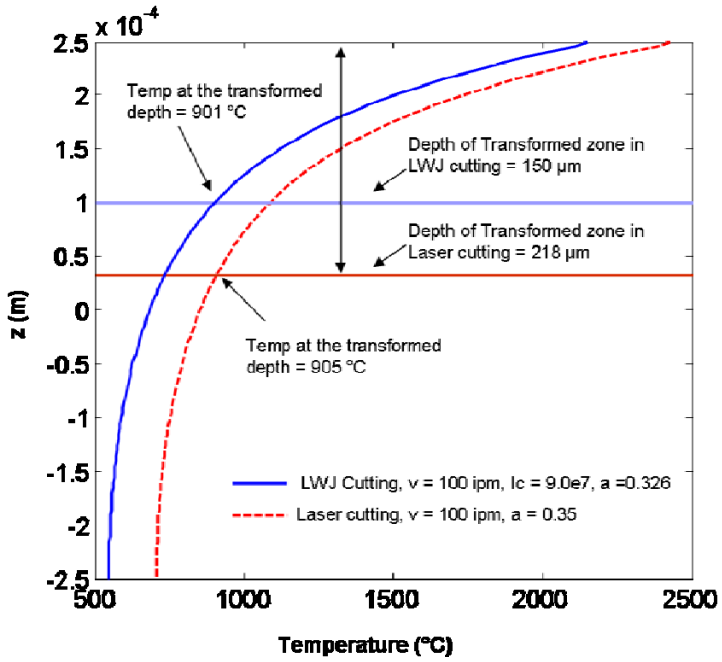

Figure 5.7: Temperature across thickness for different machining methods for the determination of respective absorptivity.

The LWJ temperature curve on the surface (z= d/2) and at x = 0 m and y = 0.04 m is shown in Figure 5.8 with respect to time. The temperature curve increases during heating and attains a maximum value at the end of the heating zone and drops sharply there afterwards. The curve shows a small dip (shown by a circle) and then a gradual increase before converging to room temperature or 0°C. The relatively sharp downward slope of the LWJ curve is caused due to water quenching and the rise in the curve is caused when the heat flows from neighboring regions. This leads to the dipping effect seen in the Figure 5.8. Such effects might not be seen in temperature plots of low thermal conductive materials like alumina [17, 18]. It is worthy to note that the temperature rise takes place even when the cooling zone has not completely crossed the point of interest. Heat from the neighboring regions raises the temperature before it drops

down to zero. The cooling part of the curve is simulated by Eigen function series solution for the temperature model. The number of Eigen functions used in the mathematical model along *x*, *y*, and *z* axes were 50, 400, and 50 respectively. The Eigen function expansion provides a simple form of the temperature and stress solution but suffers from very slow convergence in resolving large gradients. The slow rate of convergence leads to a wavy profile. Increasing the number of Eigen functions leads to smoother curves but results in extremely large computational times. However, increase in number of Eigen functions has no effect on the maximum tensile stress developed at the highest cooling point.

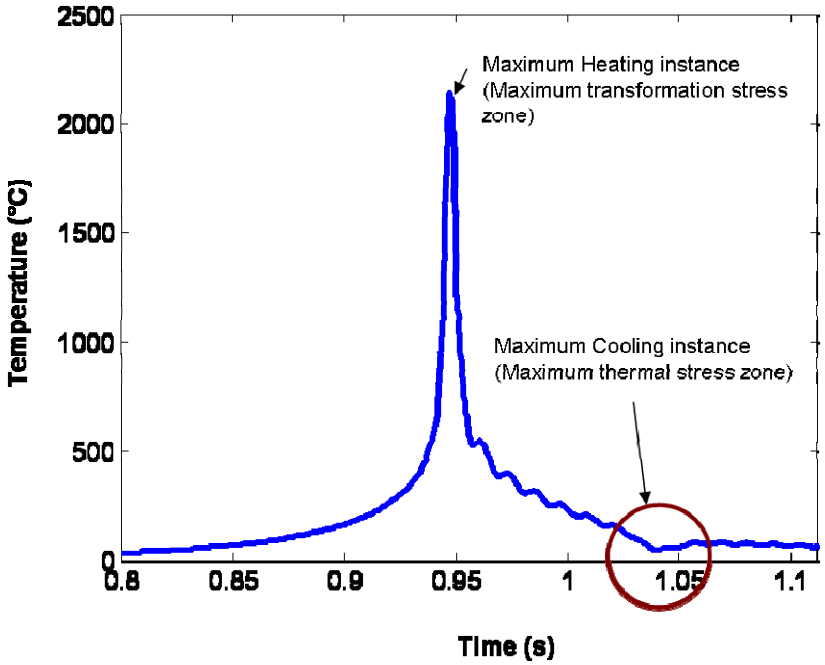

Figure 5.8: Temperature plot at an arbitrary point on the surface at different time intervals

5.5.4. Computation of stress intensity factor and Griffith Energy

LWJ cutting of polycrystalline diamond is a thermo-chemical mode of machining involving both thermal and transformation stresses. The highest thermal stresses (tensile) occur during cooling while highest transformation stresses are encountered during heating. Thermal stresses were calculated from the temperature distributions across the workpiece. The tensile thermal stresses during cooling for LWJ and laser machining are on the order of 100 MPa. The peak tensile thermal stresses across the thickness are plotted in Figure 5.9.

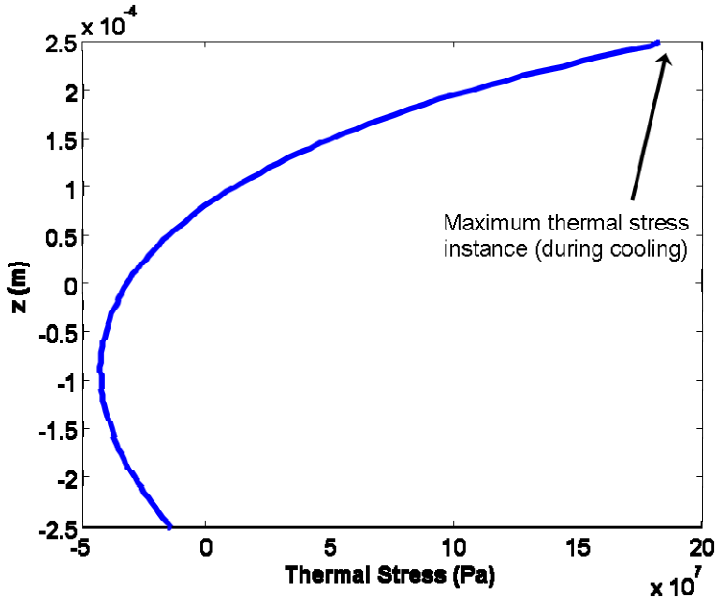

Figure 5.9: Stress distribution across the thickness for laser and LWJ machining

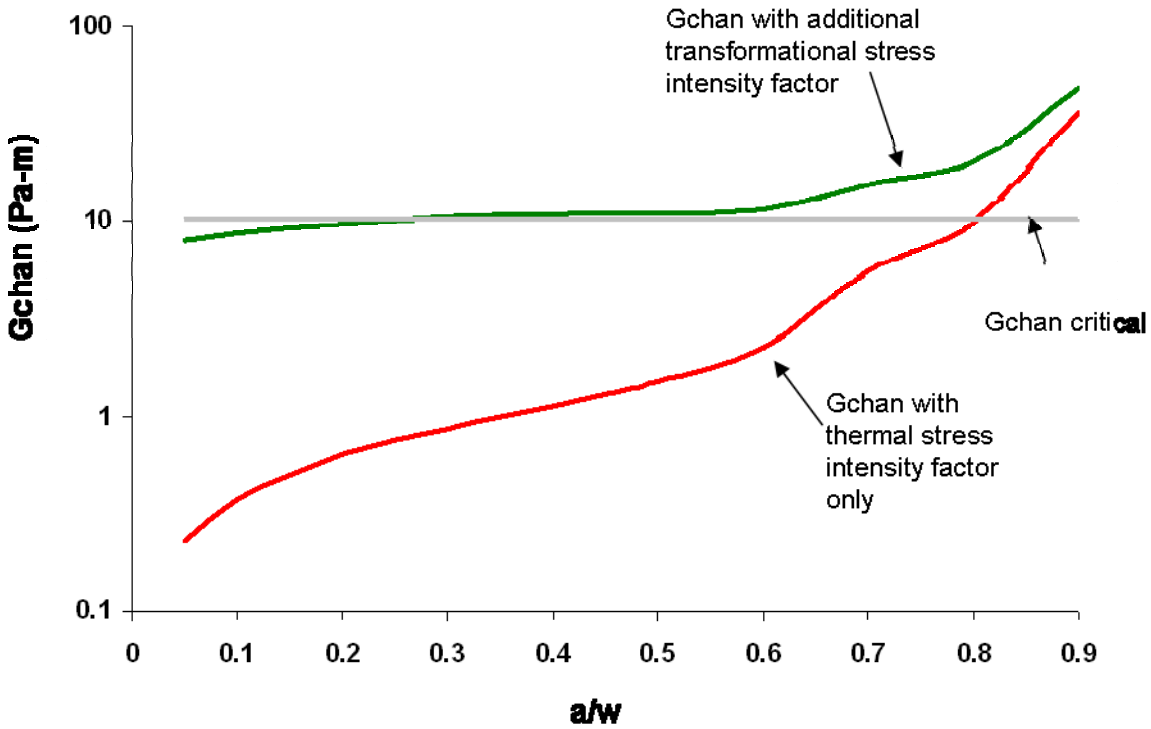

Figure 5.10: Griffith Energy Vs a/w. Griffith Energy calculated for thermal stress only

The stress intensity factor for the plane strain edge cracks (see Figure 5.2 (a)) are calculated using weight function method for Mode I loading of crack (in the *x*-*z* plane) [27] and the weight functions for different crack lengths are calculated using finite element package, ABAQUS (Providence, RI). The Griffith Energy for crack channeling was calculated as a function of a/w and is plotted in Figure 5.10. It can be seen that the

G_{ct} curve for thermal stresses are lower than the G_c (critical energy release rate) at the crack depth of 0.3 *w* (and well extends upto 0.8 *w*) corresponding to the depth of the diamond to graphite transformation zone.

According to our hypothesis, a stress intensity factor due to transformation has aided the crack channeling energy to exceed the critical energy. The calculated minimum value of the additional transformational stress intensity factor required for fracture was 2.2 MPa√m for 0≤a/w≤0.3. This corresponds to a crack mouth opening displacement of 51 nm. The Griffith Energy curve representing the combined effect thermo-mechanical stress and the chemical transformation is shown in Figure 5.10. For a/w ranging from 0.3 to 0.9, the K_I values calculated by either of the formulae (Eqn (20) or Eqn (21)) are nearly equal and hence only one set of values were considered in the calculation of Griffith Energy. Hence, the effect of the chemical transformation has resulted in a wedge which has played a significant part in crack propagation. It is to be noted that even earth worms use this mode of wedge opening technique to open up tougher soil layers [28]. Diamond has a lattice spacing of 2.0 Å and graphite has a lattice spacing of 3.5 Å, which approximately amounts to a strain of 75% [34]. The transformed material acts as a wedge due to its higher volume and produces a splitting effect resulting in opening up the crack [29, 30]. This type of wedge induced crack propagation is also seen in the burrowing pattern of worms in sands of higher toughness [28].

The process map for laser/LWJ cutting of PCD substrates is shown in Figure 5.11. The process map relates the experimentally observed fracture behavior with laser machining parameters. The process map helps to understand the different regimes in the material separation of PCD substrates. The threshold CO_2 laser power to initiate transformation for 0.5 mm thick substrates was found to be 1000 W. Line energy (ratio of laser power to velocity in J/mm) greater than 23.1 J/mm yields material separation in both laser and LWJ cutting while line energy in between 23.1 J/mm and 11.41 J/mm yields scribing for LWJ cutting and material separation for laser cutting. Line energy lower than 11.41 J/mm yields scribing.

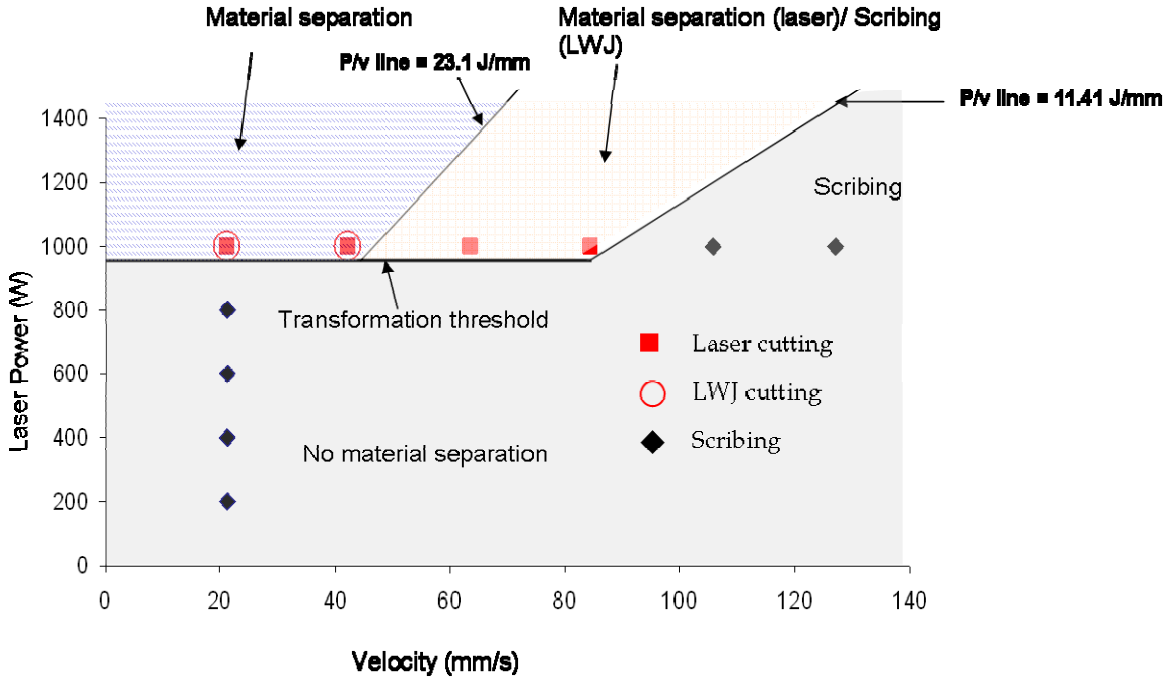

Figure 5.11: Process Map for machining of PCD substrates

5.6. CONCLUSION

Machining of PCD substrates were accomplished using novel thermochemical material removal mechanism in which localized heating of PCD leads to phase transformation. Both thermal stresses during waterjet cooling and the expansion associated with the phase transformation leads to localized loading and controlled crack propagation. The mathematical model was useful in obtaining transformational stress intensity factor and process maps relating laser machining parameters to the observed fracture behavior. Experimental and numerical results demonstrate that PCD substrates can be machined along one dimension at high cutting velocity using both CO_2 laser and CO_2 laser/waterjet. The maximum cutting speeds experimentally determined (86.64 mm/s by laser cutting and 43.32 mm/s by CO_2 LWJ cutting) are much higher than the cutting speeds previously reported by Nd:YAG laser.

Acknowledgements

The authors gratefully acknowledge the financial support for this research provided by the U.S. National Science Foundation under the grant DMI – 0522788. The authors would also like to thank Mr. Seo In-seok, Department of Material Science, Iowa State University, Ames, IA for optical characterization.

5.7. REFERENCES

[1] P. M. Harrison, M. Henry, and M. Brownell, "Laser processing of polycrystalline diamond, tungsten carbide, and a related composite material," *Journal of Laser Applications*, vol. 18, pp. 117-126, 2006.

[2] S. B. Aronsson and M. G. Waldenstrom, "Diamond tools for rock drilling and machining ". Sweden, 1988.

[3] H. Katzman and W. F. Libby, "Sintered Diamond Compacts with a Cobalt Binder," *Science*, vol. 172, pp. 1132-&, 1971.

[4] X. L. Liu, Y. F. Li, F. G. Yan, Y. Wang, J. S. Hu, and Y. J. Wang, "Study on precision grinding technique of PCD tool's cutting edge," in *Advances in Grinding and Abrasive Technology Xiii*, vol. 304-305, *Key Engineering Materials*, 2006, pp. 186-190.

[5] M. Akaishi and S. Yamaoka, "Physical and chemical properties of the heat resistant diamond compacts from diamond-magnesium carbonate system," *Materials Science and Engineering a-Structural Materials Properties Microstructure and Processing*, vol. 209, pp. 54-59, 1996.

[6] T. Irifune, A. Kurio, S. Sakamoto, T. Inoue, and H. Sumiya, "Materials - Ultrahard polycrystalline diamond from graphite," *Nature*, vol. 421, pp. 599-600, 2003.

[7] C. A. Harper, *Handbook of Ceramics, Glasses and Diamonds*: Mc Graw Hill, 2001.

[8] Y. H. Liu, Y. F. Guo, and J. C. Liu, "Electric discharge milling of polycrystalline diamond," *Proceedings of the Institution of Mechanical Engineers Part B-Journal of Engineering Manufacture*, vol. 211, pp. 643-647, 1997.

[9] J. Y. Pei, C. N. Guo, and D. J. Hu, "Electrical discharge grinding of polycrystalline diamond," in *Advances in Materials Manufacturing Science and Technology*, vol. 471-472, *Materials Science Forum*, 2004, pp. 457-461.

[10] P. L. Tso and Y. G. Liu, "Study on PCD machining," *International Journal of Machine Tools & Manufacture*, vol. 42, pp. 331-334, 2002.

[11] B. Bhushan, V. V. Subramaniam, A. Malshe, B. K. Gupta, and J. Ruan, "Tribological Properties of Polished Diamond Films," *Journal of Applied Physics*, vol. 74, pp. 4174-4180, 1993.

[12] A. B. Harker, J. F. Flintoff, and J. F. DeNatale, "Polishing of polycrystalline diamond films," presented at SPIE Proceedings - Diamond Optics III San Diego, CA, 1990.

[13] Y. Chen, L. C. Zhang, and J. A. Arsecularatne, "Polishing of polycrystalline diamond by the technique of dynamic friction. Part 2: Material removal mechanism," *International Journal of Machine Tools & Manufacture*, vol. 47, pp. 1615-1624, 2007.

[14] Y. Chen, L. C. Zhanga, J. A. Arsecularatne, and C. Montross, "Polishing of polycrystalline diamond by the technique of dynamic friction, part 1: Prediction of the interface temperature rise," *International Journal of Machine Tools & Manufacture*, vol. 46, pp. 580-587, 2006.

[15] A. M. Zaitsev, *Optical properties of diamond: a data handbook*: Springer, 2001.

[16] D. Kalyanasundaram, J. Wille, P. Shrotriya, and P. Molian, "CO_2 Laser/Waterjet machining of Polycrystalline Cubic Boron Nitride," presented at 36th North American Manufacturing Research Conference (NAMRC), Tecnologico de Monterrey, Monterrey, Mexico, 2008.

[17] D. Kalyanasundaram, G. Shehata, C. Neumann, P. Shrotriya, and P. Molian, "Design and validation of a hybrid laser/water-jet machining system for brittle materials," *Journal of Laser Applications*, vol. 20, pp. 127-134, 2008.

[18] D. Kalyanasundaram, P. Shrotriya, and P. Molian, "Obtaining a Relationship Between Process Parameters and Fracture Characteristics for Hybrid CO2 Laser/Waterjet Machining of Ceramics," *Journal of Engineering Materials and Technology*, vol. 131, pp. 011005-10, 2009.

[19] R. Molian, Shrotriya, P., Molian, P., "Thermal stress fracture mode of CO2 laser cutting of aluminum nitride," *International Journal of Advanced Manufacturing Technology*, 2007.

[20] F. P. Bundy, H. T. Hall, H. M. Strong, and R. H. Wentorf, "Man-Made Diamonds," *Nature*, vol. 176, pp. 51-55, 1955.

[21] O. D. Sibailly, F. R. Wagner, L. Mayor, and B. Richerzhagen, "High precision laser processing of sensitive materials by Microjet," presented at Fourth International Symposium on Laser Precision Microfabrication, 2003.

[22] B. P. Payne, N. S. Nishioka, B. B. Mikic, and V. Venugopalan, "Comparison of pulsed CO2 laser ablation at 10.6 mu m and 9.5 mu m," *Lasers in Surgery and Medicine*, vol. 23, pp. 1-6, 1998.

[23] T. Elperin and G. Rudin, "Thermal stresses in functionally graded materials caused by a laser thermal shock," *Heat and Mass Transfer*, vol. 38, pp. 625-630, 2002.

[24] B. A. Boley and J. H. Weiner, *Theory of Thermal Stresses*. Mineola, New York: Dover Publications, Inc., 1997.

[25] L. G. Zhao, T. J. Lu, and N. A. Fleck, "Crack channelling and spalling in a plate due to thermal shock loading," *Journal of the Mechanics and Physics of Solids*, vol. 48, pp. 867-897, 2000.

[26] J. W. Hutchinson and Z. Suo, "Mixed-Mode Cracking in Layered Materials," in *Advances in Applied Mechanics, Vol 29*, vol. 29, *Advances in Applied Mechanics*, 1992, pp. 63-191.

[27] H. Tada, P. C. Paris, and G. R. Irwin, *Stress Analysis of Cracks Handbook*. St, Louis: Del Research, MI, 1985.

[28] K. M. Dorgan, S. R. Arwade, and P. A. Jumars, "Worms as wedges: Effects of sediment mechanics on burrowing behavior," *Journal of Marine Research*, vol. 66, pp. 219-254, 2008.

[29] R. Walter, L. Ostergaard, J. F. Olesen, and H. Stang, "Wedge splitting test for a steel-concrete interface," *Engineering Fracture Mechanics*, vol. 72, pp. 2565-2583, 2005.

[30] J. Xiao, H. Schneider, C. Dönnecke, and G. König, "Wedge splitting test on fracture behaviour of ultra high strength concrete," *Construction and Building Materials*, vol. 18, pp. 359-365, 2004.

[31] A. Forderreuther, G. Thurn, A. Zimmermann, and F. Aldinger, "R-curve effect, influence of electric field and process zone in BaTiO3 ceramics," *Journal of the European Ceramic Society*, vol. 22, pp. PII S0955-2219(01)00516-7, 2002.

[32] Y. Murakami, *The Stress Intensity factor handbook*. Oxford: Pergamon, 1987.

[33] P. J. F. Harris and S. C. Tsang, "A simple technique for the synthesis of filled carbon nanoparticles," *Chemical Physics Letters*, vol. 293, pp. 53-58, 1998.

[34] C. Z. Wang, K. M. Ho, M. D. Shirk, and P. A. Molian, "Laser-induced graphitization on a diamond (111) surface," *Physical Review Letters*, vol. 85, pp. 4092-4095, 2000.

[35] G. Jungnickel, C. D. Latham, M. I. Heggie, and T. Frauenheim, "On the graphitization of diamond surfaces: The importance of twins," *Diamond and Related Materials*, vol. 5, pp. 102-112, 1996.

[36] F. S. Phinney, "Graphitization of Diamond," *Science*, vol. 120, pp. 393-394, 1954.

[37] M. F. Ashby, *Materials Selection in Mechanical Design*. Oxford, England: Butterworth-Heinemann, 2001.

[38] C. Moelle, M. Werner, F. Szucs, D. Wittorf, M. Sellschopp, J. von Borany, H. J. Fecht, and C. Johnston, "Specific heat of single-, poly- and nanocrystalline diamond," *Diamond and Related Materials*, vol. 7, pp. 499-503, 1998.

[39] D. Miess and G. Rai, "Fracture toughness and thermal resistance of polycrystalline diamond compacts," *Materials Science and Engineering a-Structural Materials Properties Microstructure and Processing*, vol. 209, pp. 270-276, 1996.

CHAPTER 6. ANALYSIS OF THE THERMO-CHEMICAL MACHINING OF POLYCRYSTALLINE CUBIC BORON NITRIDE

Dinesh Kalyanasundaram[1], James Anderegg[2], Jeff Wille[1], Pranav Shrotriya[1], and Pal Molian[1]

[1]**Laboratory for Lasers, MEMS, and Nanotechnology**

Department of Mechanical Engineering

[2]**Ames Laboratory**

Iowa State University

Ames, IA, 50011

6.1. ABSTRACT

The significance of polycrystalline cubic boron nitride (PCBN) as a tip tool material for machining high strength alloys/steels emphasizes the demanding need for a faster and a cost effective machining system for precise fabrication of these tools. We have discussed a hybrid Laser/Waterjet (LWJ) machining system for this purpose, its underlying mechanism of machining, and the process parameters in the cutting of 1.6 mm thick PCBN. While LWJ cutting of low thermal conductive materials like alumina, zirconia etc was completely based on thermal shock induced fracture, it was found that the cutting of cubic boron nitride has been greatly assisted by the thermo-chemical transformation process. We have attempted to calculate the stress intensity factors due to chemical transformation and thermo-mechanical stresses using a mathematical model discussed in this paper. Also better cut quality in terms of kerf width, recast layer, presence of micro-cracks, surface roughness, and flexural strength has also been discussed in this paper.

Keywords: polycrystalline cubic boron nitride (PCBN), Laser/waterjet machining (LWJ), thermal shock machining, thermo-chemical machining, transformation, cut quality

6.2. INTRODUCTION

Polycrystalline cubic boron nitride (PCBN) has a proven performance in the machining of high strength steels/alloys as well as metal matrix composites [1]. However, PCBN is a difficult-to-machine ceramic material due to its ultra-high hardness and good chemical and thermal stability. Laser machining of ceramics has been increasingly gaining acceptance as an alternative to traditional machining methods [2-5]. Swiss Federal Institute of Technology in Lausanne, Switzerland has developed Laser-Microjet® [6], a hybrid technology based on waterjet-guided Nd:YAG laser for machining of PCBN. In this laser based cutting technique, a free laminar waterjet is used as an optical waveguide to direct the Nd:YAG laser beam onto the sample. The Laser-Microjet® allows precise cutting of PCBN materials with small kerf and good surface finish. Q-switched pulse laser (up to 300 W) of 532 nm wavelength and water pressure of 2-10 MPa was employed for the process. Though this process helped to obtain a taper-free, narrow kerf features and smaller tolerances (than those obtained with conventional laser and EDM processes), it suffers from very slow cutting speeds as it reports 60 passes with each pass at a speed of 6 mm/min to cut 3.25 mm thick PCBN sample.

A non-traditional hybrid CO_2-Laser/Waterjet (LWJ) machining process has been developed by our group and has been applied in the machining of electronic ceramics such as aluminum oxide and aluminum nitride [3, 7]. Details of the design and working principles of LWJ system are described in Kalyanasundaram, D, *et al*. [3]. During the localized laser heating of the PCBN blank in an oxygen-rich environment, both the binder phase and the substrate material undergoes chemical transitions resulting in a build-up of tensile stresses in the surface layers which lead to crack formation and subsequent separation of PCBN wafers along the laser path. Unlike other machining techniques which uses a harder tool to machine PCBN, we exploit a given property (chemical transformation) of the material to achieve material separation. In this work, we have explained the mechanism of fracture with both the thermo-mechanical analysis and thermo-chemical analysis . We have calculated the Griffith Energy from stress intensity factors for both chemical transformation and thermo mechanical stresses.

6.3. MATERIALS AND EXPERIMENTAL PROCEDURE

6.3.1 Material composition and dimension

Experiments were conducted on commercial grade, electrically insulating Polycrystalline Cubic Boron Nitride samples of 66mm dia x 1.6 mm thick from Diamond Innovations, Inc. (Worthington, Ohio). PCBN is a part of BZN 6000 series with a composition of 82% CBN (particle size of 8-12 μm) and 18% of AlN binder and other impurities.

6.3.2 LWJ Experimental setup and procedure

A continuous wave CO_2 Laser (Model 820 Spectra Physics) of 10.6 μm wavelength and 1.5 kW rated power was used for the experiments. The laser head has been modified to accommodate the low-pressure Waterjet (< 1000psi or < 8MPa). The design of the LWJ system and working mechanism has been discussed elsewhere [2]. The beam from the laser was sent through a circular polarizer and then directed into a focusing lens in a gas-jet cutting assembly. The 126-mm focal length lens produced a theoretical focal spot diameter of 0.2 mm at the sample surface. The samples are placed on *x-y* positioning table controlled by a computer numerical (CNC) controller.

Two sets of experiments were conducted. The first set of experiments were conducted with laser alone and the second set of experiments were conducted with laser/waterjet (LWJ). The results from these two sets would help us in understanding the mechanisms of fracture and the relative advantages of each of the individual process.

The first set of cutting experiments were carried out with the laser alone and oxygen as an assist gas. The laser powers were varied between 400 and 600 W. The machining was performed at different laser head velocities from 2.11 mm/s (5 inch/min) to 6.35 mm/s (15 inch/min). Oxygen with a pressure of 69 kPa (10 psi) was delivered through a coaxial nozzle with a diameter of 2 mm. The laser beam was focused to a spot size of 0.2 mm diameter on the sample surface and air pressure in the coaxial nozzle was held at 35 kPa (5

psi) to protect the lens from spatter. The nozzle was maintained at a standoff distance of 2-3 mm from the surface of the substrate.

The second sets of experiments were conducted with LWJ at laser power of 800 W. The machining was performed at different laser head velocities of 2.11 mm/s (5 inch/min), 4.23 mm/s (10 inch/min) and 6.35 mm/s (15 inch/min). The waterjet pressure was made constant at 3445 kPa (500 psi). The waterjet trailed the laser beam on the workpiece surface with a spacing of 3.1 mm between their centers. The aim of the experiment was to find the threshold line energy (ratio of laser power to cutting velocity) for material separation.

6.3.3 Topography and Chemical Analysis

Optical microscope equipped with an image acquisition system and scanning electron microscope (Joel 6600) were used to characterize the cut quality features such as the kerf width, width of heat affected zone, and taper of cut surface etc. Surface roughness measurements were performed using a Zygo model 5000 series optical profilometer of vertical resolution of 0.1 nm. This instrument utilizes a white light optical interference technique and offers a non-contact, rapid method of characterizing and quantifying 3-D surface data including surface roughness, step heights, critical dimensions, and other topographical features with excellent precision and accuracy. Chemical compositions of the substrate and cut surface were analyzed by X-ray Photoelectron Spectroscopy (a multitechnique chamber Perkin-Elmer Model 5500) with PHI-ACCESS software. The base pressure of the chamber was 1.03 x 10^{-7} Pa (8 × 10^{-10} Torr) or less. The X-ray source provides monochromatized Al *K* α radiation at a power of 250 W. The take-off angle used in these experiments was 45 °.

6.4. MATHEMATICAL MODELING

To quantity the fracture behavior i.e to obtain a relationship between the observed fracture behavior and the laser machining parameters, a mathematical model had been devised. Determination of the temperature distribution along the laser cutting path forms the first task. Green's method of solution of the Heat

Conduction model helps in the determination of required temperature field. Evaluation of quasi-static stresses [8] from the temperature distribution was the next step/ task before estimation of the stress intensity factors/Griffith Energy release rates for different crack configurations and relating them to the corresponding cutting parameters.

6.4.1 Determination of Temperature distribution

The temperature distributions at different points on the workpiece were determined by solving the Fourier's Heat conduction equation stated by Eqn (1a).

$$c_p \rho \frac{\partial T}{dt} = k\nabla^2 T + q\left(x, y, t, I_h, I_c\right) \qquad \text{Eqn (1a)}$$

where

$$q\left(x, y, t, I_h, I_c\right) = I_h \mathrm{H}\left(h_x - |x|\right)\left[\mathrm{H}\left(vt - y\right) - \mathrm{H}\left(vt - y - 2h_y\right)\right] \qquad \text{Eqn (1b)}$$
$$- I_c \mathrm{H}\left(c_x - |x|\right)\left[\mathrm{H}\left(vt - 2h_y - l_0 - y\right) - \mathrm{H}\left(vt - 2h_y - l_0 - 2c_y - y\right)\right]$$

Here c_p is the specific heat of the material, ρ is the density of the material, k is the conductivity of the material, $q\ (x,y,t,I_h,I_c)$ is the total heat input, I_h is the heating intensity of the laser beam and I_c is the cooling intensity of the waterjet, H is the Heaviside function, v is the velocity of the cutting head, h_x, c_x, h_y, c_y are the half lengths of the heating and cooling zones along x and y direction respectively and l_0 is the separation distance between the laser spot and the waterjet cooling zone on the surface of the workpiece. The boundary conditions depicting the LWJ cutting experiment are given in Eqn (2). The top layer was modeled as a convective layer where both laser heating and waterjet cooling takes place (Figure 6.1). The bottom layer was modeled as an insulated layer due to the absence of any physical contact of the fixture with the lower part of the workpiece (directly below the laser cutting path) and also due to minimal possible flow of air through the channel covering the lower part. The assumption would also enable us to choose a simpler mathematical function which satisfies the given boundary conditions.

$$k\frac{\partial T}{\partial z}_{z=d/2} = k\frac{\partial T}{\partial x}_{x=\pm xa} = k\frac{\partial T}{\partial y}_{y=yb} = -h\left(T - T_A\right)$$

$$\frac{\partial T}{\partial z}_{z=-d/2} = \frac{\partial T}{\partial y}_{y=0} = 0 \quad \left(\text{Insulated Boundary Condition}\right) \qquad \text{Eqn (2)}$$

$$T\left(x, y, z, t=0\right) = T_0$$

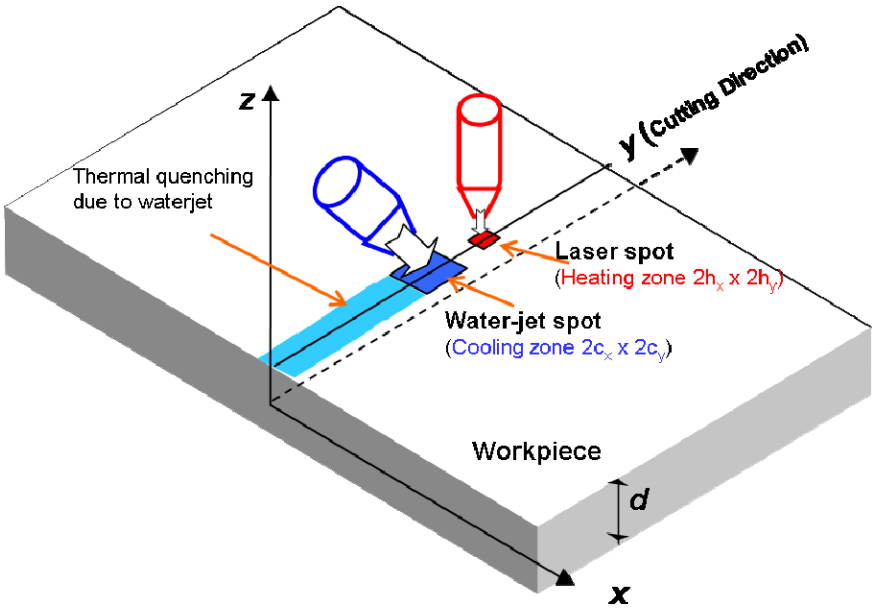

Figure 6.1: Orientation of the workpiece and the different axes

The temperature solution can be obtained either by error function approach or by Eigen function approach. While the former has been used to capture the steep temperature gradients during heating, the latter has been used during the cooling instance as it helps in obtaining a simplified solution for solving stress fields.. Maximum tensile stresses occur during cooling where there are no steep gradients and the temperature drops down to ambient temperature. The mechanical and thermal properties of PCBN considered in the analysis are given in Table 6.1.

Table 6.1: Properties of PCBN considered in the Analysis

Density	Thermal Conductivity	Specific Heat Capacity	Poisson 's Ratio	Young's modulus PCBN	Thermal expansion coefficient		Fracture Toughness
					PCBN	AlN	
3400 kg/m^3 [9]	200 [10] W/mK	900 [10] - 960 [11] J/kgK	0.15[9]	710 GPa[9]	5.6 x 10^{-6} [10]	4.5 x 10^{-6} (/K)[7]	4.5-5.5 MPa √m [12]

$$T(x,y,z,t)=\int_0^{\infty}\int_{-\infty}^{\infty}\int_0^{\infty} q\left(x_0,y_0,t_0,I_h,I_c\right)\theta\left(x,x_0,y,y_0,z,t,t_0\right)dy_0.dx_0.dt_0+T_0 \qquad \text{Eqn (3)}$$

where $\theta\left(x,x_0,y,y_0,z,t,t_0\right)$ is the solution to the associated problem given by

$$c_p\rho\frac{\partial T}{dt}=k\nabla^2T+\delta\left(x-x_0\right)\delta\left(y-y_0\right)\delta\left(z-\frac{d}{2}\right)\delta\left(t-t_0\right) \qquad \text{Eqn (4)}$$

The temperature solution in error function approach can be written as

$$T\left(x,y,z,t\right)=\frac{1}{4kd}\int_0^t\sum_{i=1}^{n}\left(Q_h-Q_c\right)A_i Cos\,\xi_i\;Cos\left(\xi_i\left(\frac{1}{2}+\frac{z}{d}\right)\right)exp\left(\frac{-\xi_i^2\sqrt{\kappa(t-t_0)}}{d^2}\right)dt_0\;+T_0$$

Eqn (5)

where Q_h, Q_c, A_i, a, ξ_i *and* T_0 are given by

$$Q_h=\frac{I_h\kappa}{4}\left\{erf\left[\frac{x+h_x}{2\sqrt{\kappa(t-t_0)}}\right]-erf\left[\frac{x-h_x}{2\sqrt{\kappa(t-t_0)}}\right]\right\}\left\{erf\left[\frac{y+vt_0}{2\sqrt{\kappa(t-t_0)}}\right]-erf\left[\frac{y-vt_0}{2\sqrt{\kappa(t-t_0)}}\right]\right\}$$

Eqn (6a)

$$Q_c=\frac{I_c\kappa}{4}\left\{erf\left[\frac{x+c_x}{2\sqrt{\kappa(t-t_0)}}\right]-erf\left[\frac{x-c_x}{2\sqrt{\kappa(t-t_0)}}\right]\right\}\ldots$$

$$\ldots..\left\{erf\left[\frac{y+vt_0-2h_y-l_0}{2\sqrt{\kappa(t-t_0)}}\right]-erf\left[\frac{y-vt_0-2h_y-l_0-2c_y}{2\sqrt{\kappa(t-t_0)}}\right]\right\} \qquad \text{Eqn (6b)}$$

Here κ represents thermal diffusivity and ξ_i represents Eigen values of the characteristic equation, $\xi_i\ tan\xi_i = Bi$ where Bi represents Biot number.

The value of the coefficient

$$A_i=2\left(\frac{\xi_i^2+Bi^2}{\xi_i^2+Bi^2+Bi}\right) \qquad \text{Eqn (7a)}$$

and heating intensity

$$I_h = a_s \frac{4P}{\pi b^2} \qquad \text{Eqn (7b)}$$

where P and b are the laser power (W) and laser spot size (m) respectively. The cooling intensity I_c of the waterjet is the maximum intensity that would cool the workpiece to near room temperature [13]. The Eigen function solution has been discussed in detail by Kalyanasundaram *et al*. [13]. The Eigen solutions are more appropriate for zones sufficiently away from the boundary of the workpiece.

6.4.2 Determination of Thermal stresses

Non-uniform heating and cooling of the specimen leads to development of thermal stresses in the specimen [8]. Uncoupled quasistatic thin plate analysis was used to determine the resulting thermal stress fields. Since the thickness of the wafer is thin in comparison to its length and width, a plane stress assumption was used in the mathematical model.

$$\sigma_{zz} = 0 = \sigma_{xz} = \sigma_{yz} \qquad \text{Eqn (8)}$$

Stress function Φ and out-of-plane displacement fields w_d satisfy the following differential equations and associated boundary conditions of stress free boundaries of the workpiece.

$$\nabla^4 \Phi = -\nabla^2 N_T \qquad \text{Eqn (9)}$$

$$D\nabla^4 w_d = -\frac{1}{1-\upsilon}\nabla^2 M_T \qquad \text{Eqn (10)}$$

where the bending rigidity per unit length, $D = \frac{1}{12\left(1-\upsilon^2\right)} Ed^3$ Eqn (11)

Temperature distribution across the thickness determines the forcing terms in the above equations:

$$N_T = \alpha E \int_{-d/2}^{d/2} T \, dz \qquad \text{Eqn (12)}$$

$$M_T = \alpha E \int_{-d/2}^{d/2} z \, T \, dz \qquad \text{Eqn (13)}$$

Stress function and out-of-plane displacement fields are also expressed as an Eigen function expansion and the partial differential equations are reduced to algebraic equations and hence easily solved. When the heat source and cooling zone are at sufficient distance from the workpiece boundaries, the stress free boundary conditions are exactly satisfied because the temperature field is localized near the processing zone and insignificantly small near the boundaries. Hence, the solutions for stress function and out-of-plane displacements are given by:

$$\Phi = \alpha E \frac{1}{\omega_m^2 + \xi_n^2} \int_{-d/2}^{d/2} T \, dz \qquad \text{Eqn (14)}$$

$$w_d = \alpha E \frac{\omega_m^2 + \nu \xi_n^2}{\omega_m^2 + \xi_n^2} \int_{-d/2}^{d/2} z \, T \, dz \qquad \text{Eqn (15)}$$

The stress component (σ_{xx}) along the x axis that results in opening or closing of cracks is given in Eqn (16). Similar analysis may be utilized to calculate the other components of stress.

$$\sigma_{xx} = \frac{1}{1-\upsilon}\left(-\alpha E T + \frac{1}{d}\left((1-\upsilon) N_x + N_T\right)\right) - \frac{12 z D}{d^3}\left(\frac{\partial^2 w_d}{\partial x^2} + \frac{\partial^2 w_d}{\partial y^2}\right) \qquad \text{Eqn (16)}$$

The in-plane forces per unit lengths in the above expressions are determined from the stress function as follows:

$$N_x = \frac{\partial^2 \Phi}{\partial y^2}; \; N_{xy} = -\frac{\partial^2 \Phi}{\partial x \partial y}; \; N_y = \frac{\partial^2 \Phi}{\partial x^2} \qquad \text{Eqn (17)}$$

It is important to note that this solution is only valid for the cases when laser and waterjet spots are away from the workpiece boundaries and in this paper, it has only been used to determine the driving forces for cracks away from the boundaries. Further, the temperature and stress distributions are determined under the assumption that only the surface layers of material under the laser spot undergo melting, vaporization, and solidification and the localized material change does not influence the stress and temperature fields in the rest of the workpiece.

6.4.3 Crack Configurations and Energy Release Rates

Two modes of crack growth [14] can result in material separation namely plain strain cracking and crack channeling as shown in Figure 6.2. Machining can either start before/at the edge of the workpiece or inside the edge of the workpiece. And crack propagation analysis is dependent on the position of start of machining. At the beginning of a through-cut, laser radiation is incident over the specimen boundary resulting in damage and subsequent cracking across the whole thickness during waterjet quenching. Therefore, equilibrium depth of a channeling crack is most appropriate for approximating the LWJ induced cut depth in thin through-cut specimens. However in the cases where cut starts away from the free edge or boundary, crack propagation analysis is represented by a two step process: plain strain analysis of edge crack is utilized to approximate the initial cut depth at the beginning of the cut (when there are no pre-existing cracks in the workpiece), and subsequently, channeling crack analysis is utilized to approximate the propagation of the initiated cut along the laser path.

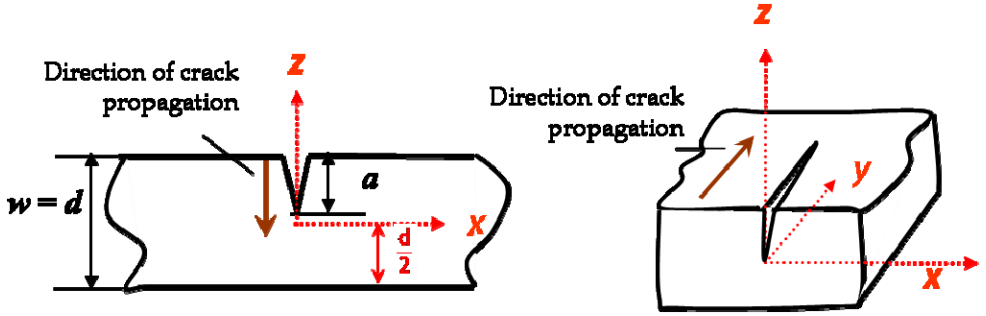

Figure 6.2 (a): Plain strain cracking **(b): Crack Channeling**

In the present paper, the case of through-cut thin PCBN workpieces was considered and the stress intensity factor and energy release rates for channeling cracks are computed using weight-functions [13, 15]. The

plane strain energy release rate G_p was calculated from the stress intensity factor K_I for mode I for different crack depths "a." The channeling energy release rate G_t for an edge crack is obtained from the average energy release rate over the depth of the channeling front [14]. For a steady state crack extension, it is assumed that the crack will channel at fixed depth, with a constant tip shape and constant release rate. The Griffith Energy release rates for plain strain cracking is given by Zhao et al [14] as in Eqn (18).

$$G_{ps} = \frac{K_I^2}{E'} \qquad \text{-- Eqn (18)}$$

where K_I is the stress intensity factor in Mode I crack loading and E' is the Young's Modulus for plane stress condition. The energy release rate for crack channeling is given by the sum of plain strain energy from integrated between 0 to the crack length as shown in Eqn (19).

$$G_{chan} = \frac{1}{a}\int_0^a G_{ps}(a')\, da' \qquad \text{-- Eqn (19)}$$

6.4.4 Effect of Transformation on Crack Propagation

The chemical transformation of the constituent compounds can take place during laser or laser/waterjet machining. This produces a wedge effect (see Figure 6.3) [16-18], if the transformed compound has a higher volume than the substrate material. Therefore the chemical transformation will in turn help propagate cracks to yield material separation. The stress intensity factor due to transformation can be related to crack mouth opening displacement. The stress intensity factor ahead of the crack tip can be expressed as a function of material property (Young's modulus & poisson's ratio) and crack/material configuration (a– length of crack, w – thickness of the specimen and δ_l – crack mouth opening displacement). The relationship between crack mouth opening displacement (CMOD) and the stress intensity factor is given by Eqns (20) and (21-a) [19, 20]. Eqn 20 is a simplified form and has been used in the calculation of stress intensity factor for wedge induced cracking [20]. A detailed form of the relationship relating K_I, P (load) and δ_l (CMOD) is given by Eqn 21. The following assumptions were made in the calculation of the additional stress intensity factor K_I due to transformation: (i) CMOD increases proportionally by a factor $(a/w+0.64)^2$ for $0 \le a/w \le d_t$

(depth of transformation) or K_I is a constant and (ii) K_I decreases proportionally by a factor of $(a/w+0.64)^2$ for $d_t<a/w\leq 0.9$.

$$K_I = \frac{\delta_l \sqrt{3} E/\left(1-v^2\right)}{2\sqrt{w}\left(a/w+0.64\right)^2} \quad \text{--- Eqn (20)}$$

$$K_I = \frac{\delta_l V_1(a/w) E/\left(1-v^2\right)}{\sqrt{w} V_2(a/w)} \quad \text{------ Eqn (21 a)}$$

where $V_1(\alpha) = (2+\alpha)(1-\alpha)^{-3/2}\left(0.886+4.64\alpha-13.32\alpha^2+14.72\alpha^3-5.6\alpha^4\right)$ ------ Eqn (21 b)

and $V_2(\alpha) = (1+\alpha)^2(1-\alpha)^{-2}\left(2.1630+12.219\alpha-20.065\alpha^2-0.9925\alpha^3+20.609\alpha^4-9.9314\alpha^5\right)$ ------- Eqn (21 c)

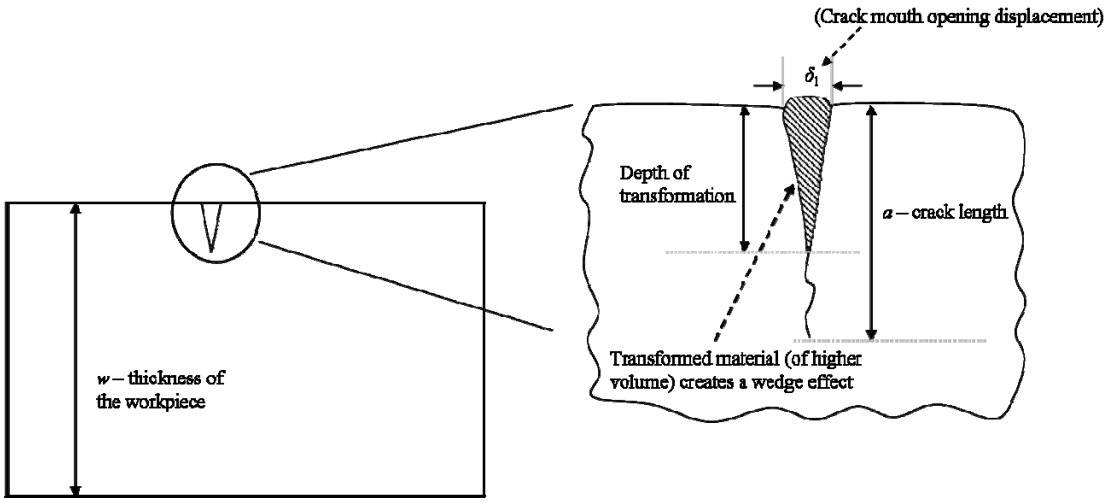

Figure 6.3: Transformational effect and CMOD

The additional stress intensity factor required to explain the cause of the (experimentally) observed fracture is the transformational stress intensity factor. The crack mouth opening displacement can be calculated from the value of the transformational stress intensity factor.

6.5. RESULTS AND DISCUSSION

6.5.1 Cut Quality and Line energy of LWJ system in comparison to Laser Machining

Cut samples by thermal fracture using CO_2 laser were compared with LWJ cut samples to evaluate the cut quality obtained in LWJ machining. Observations of the cut surfaces clearly show two distinct regions namely the oxidized zone and the fracture zone as shown in Figure 6.4 and Figure 6.5. The cut quality

obtained in LWJ cutting of both the zones are better in terms of surface roughness than that obtained in laser cutting as shown in the Table 6.. However, LWJ results in higher power consumption partly due to the cooling of workpiece by water and partly due to the absorption of laser light by water at 10.6 μm [21]. For the same reason, LWJ results in smaller and shallower heat affected zone and smaller kerf width. Crack propagation is quite controlled in LWJ cutting while in laser cutting, tapering effect is noticed at the starting edge.

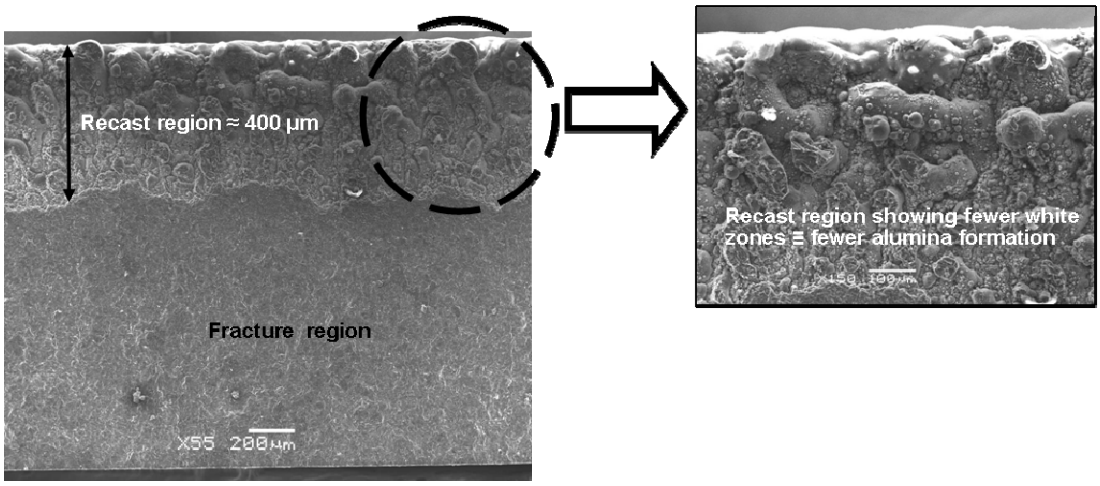

Figure 6.4: Single pass Laser cut of 1.6 mm thick CBN

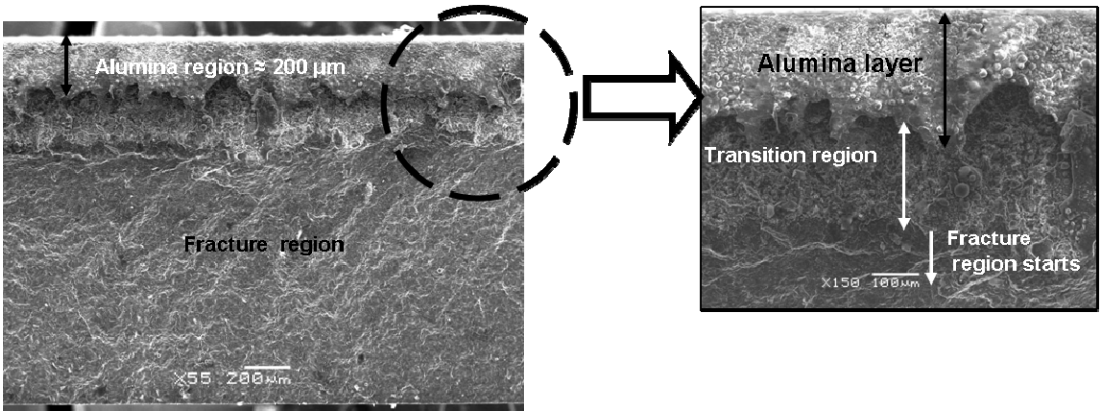

Figure 6.5: Single pass LWJ cut of 1.6mm thick CBN

6.5.2 Chemical analysis of the cut surfaces

The thermal stresses developed are inversely proportional to thermal diffusivity and therefore lower stresses are induced in high thermal conductive ceramics such as cubic boron nitride. And given its higher strength, material separation observed in the machining of PCBN can be explained by the induction of

transformational stresses. Upon investigation by X-ray photoelectron spectroscopy (XPS) it was found that there was an increase in the amount of oxygen content on the cut surface as compared to the virgin material. This increase in oxygen indicates that one or many of the several oxidation/reduction transformations may have taken place in the whiter regions in Figure 6.6, such as oxidation of boron nitride to boron trioxide, oxidation of aluminum nitride (binder) to aluminum oxide and formation of traces of aluminum boride.

Table 6.2: LWJ Vs. laser cutting of 1.6 mm PCBN blank

	Surface Roughness		Minimum Line energy	Kerf Width	HAZ*	Remarks
	Ra	RMS				
LWJ	8.6 µm	10.36 µm	368 J/mm	148 µm	630 µm	Tapering noticed [3]
Laser Cutting	10.96 µm	12.8 µm	62.3 J/mm	216 µm	1560 µm	Higher power consumption

* HAZ – Heat Affected Zone

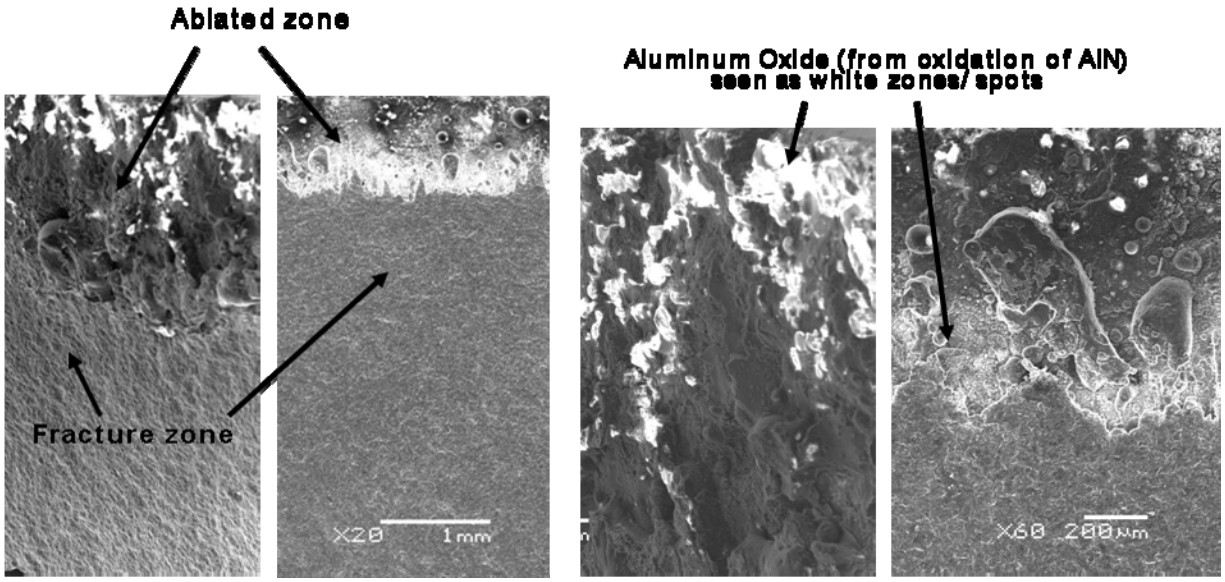

Figure 6.6: SEM image of the cross-section by (a) Laser (b) LWJ and higher magnified view (c) Laser cut (d) LWJ cut

The XPS spectrum of the individual elements on both the substrate and the oxidized material are shown in the Figure 6.7 and Figure 6.8. There is a shift in the binding energy peak of boron roughly from 193 eV (Figure 6.8 (a)) to 196 eV (Figure 6.8 (b)). This confirms the presence of boron nitride (190.4 eV [22], 190.5 eV [23], 190.6 eV [24], 192.1 eV [25], and 192.2 eV [25]) in the substrate material transforming to a mixture of boron oxide (192 eV [26], 192.4 eV [27], 193.1 eV [28], 193.3 eV [29], and 193.6 eV [30]), aluminum boride (188.5 eV [31]) and boron nitride

in the transformed region. Similarly an increase in the binding energy can be noticed for aluminum also. This confirms the formation of aluminum oxide (74.3 eV [32], 74.3 eV [33], and 74.6 eV [34]) and aluminum boride (119.8 eV [35]) from aluminum nitride (73.9 eV [36], 74.4 eV [35], and 119.4 eV[35]).

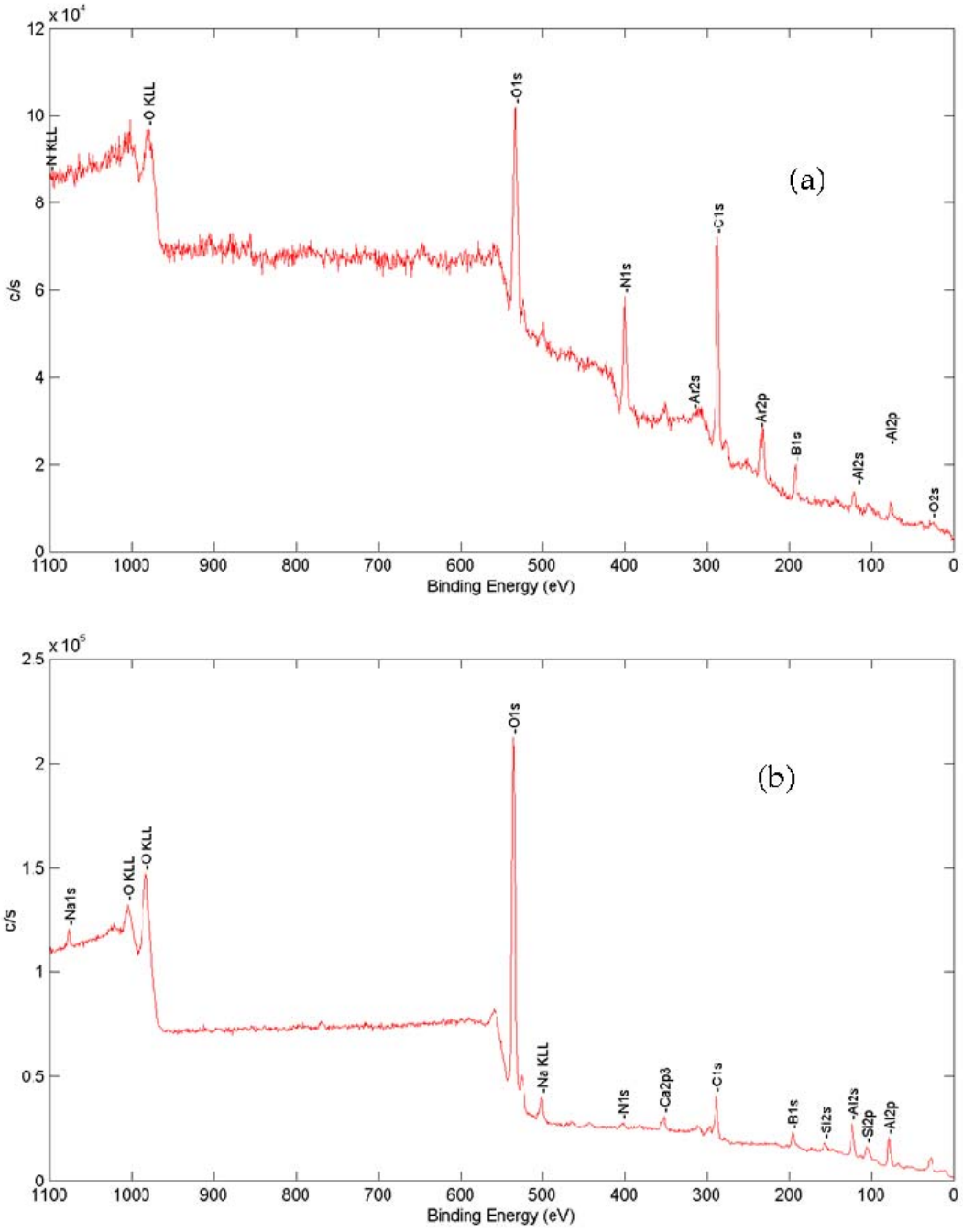

Figure 6.7: (a) XPS spectrum of bulk substrate (b) XPS spectrum of the transformed/oxidized region (white region)

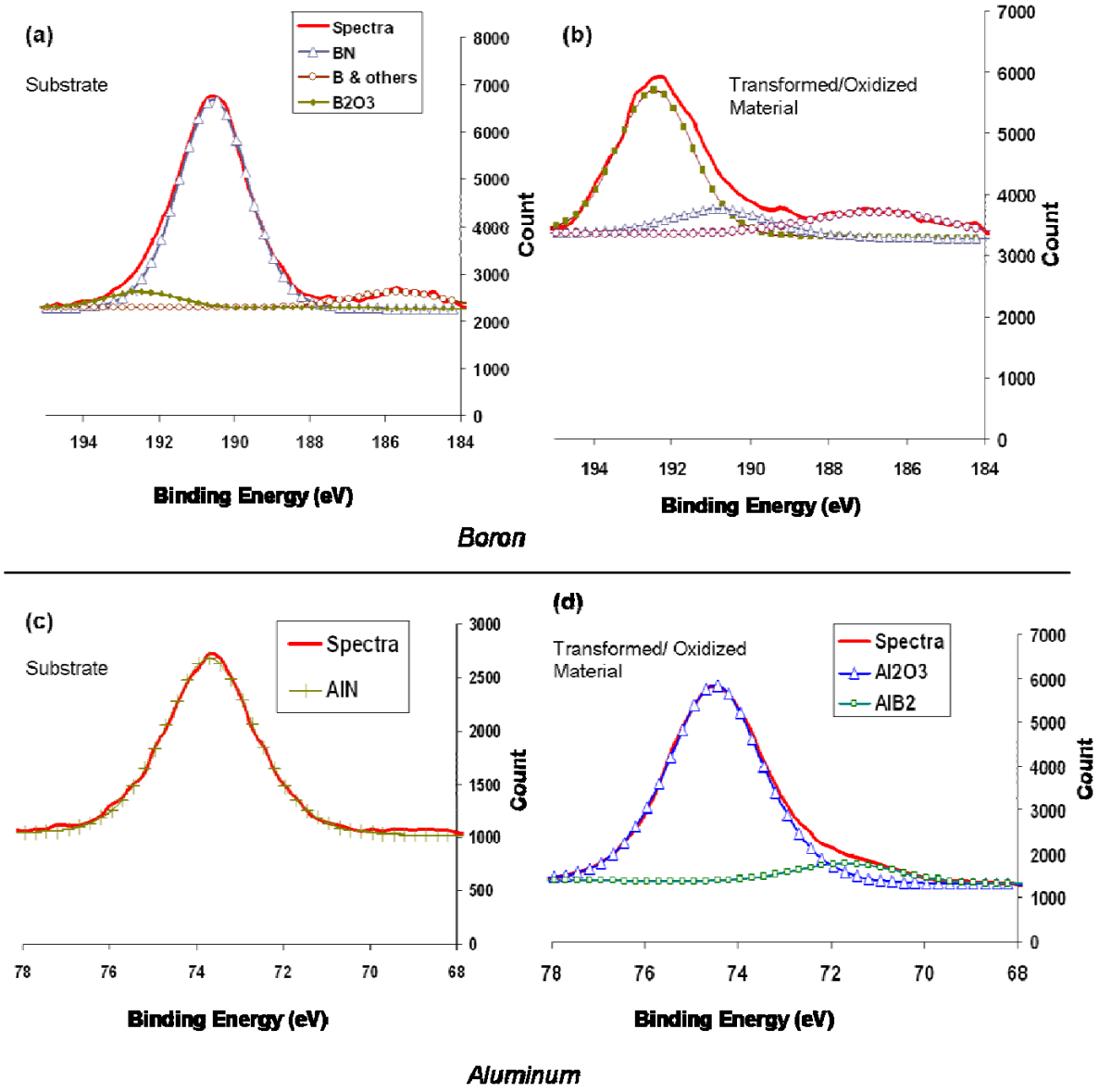

Figure 6.8 (a): XPS spectrum of boron in the substrate and (b) in the transformed region; (c) XPS spectrum of aluminum in the substrate material and (d) in the transformed region

6.5.3 Determination of Effective Absorption coefficient

The mathematical model for temperature is dependent on a number of variable factors such as the Input power Intensity or heating intensity (I_h), cooling intensity (I_c), net energy absorption coefficient (a) and convective coefficient (h). The input heat intensity for laser cutting was calculated from Eqn (7b) for a laser power of 800 W and laser spot size of 0.2 mm. In the case of LWJ cutting the laser power was 1000 W for the same spot size. The maximum intensity of cooling that will force the temperature of the workpiece to the

room temperature was chosen. For LWJ cutting, the cooling intensity used was 2.8 x 10^7 W/m^2. A maximum convective coefficient of 1 x 10^4 W/m^2 was used in the calculations [37]. The net energy absorption coefficient (a_s) was modeled to account for the losses in the laser optics, losses due to the presence of water vapor/mist in the machining zone, and the losses due to reflection and transmission of PCBN at 10.6 μm. The net absorption coefficient for laser and LWJ machining was determined by matching the temperature at the transformed depth to the onset of the oxidation of aluminum nitride of 900°C [38] and the onset of oxidation of boron nitride of 900°C [39]. The formation of aluminum borides takes place around 1363 K [40].

Experimental observation of during LWJ machining has lead us to expect a poor absorptivity of the material due to the presence of water vapor and lower cutting velocity. We iterate the value of absorptivities in the analytical model to match the temperature at the transformed depth to the oxidation temperature of aluminum nitride and boron nitride i.e 900°C [38, 39]. It was found from analysis that the effective absorptivity during laser and laser/waterjet (LWJ) machining was 0.8 and 0.233 respectively as shown in the Figure 6.9. LWJ machining at velocity of 2 mm/s (5 inch/minute) results in laser radiation being absorbed by water to a greater extent. This effect can be clearly seen in the Figure 6.9. The temperature and stress distribution can be determined given the values of the absorptivity.

A typical temperature plot at a point of the surface in the laser path with respect to time is plotted in Figure 6.10. Error function based solution is used to capture the peak temperatures while Eigen function based solution is used during cooling. It should be noted that the modeling does not take into account of melting, vaporization, and solidification. This assumption does not affect our model as the focus would be the calculation of maximum tensile thermal stresses which occur during cooling and hence the peak temperatures would not affect our model. The number of Eigen functions used along x, y, and z axes were 50, 400, and 50 respectively. The waviness of the plot was due to the poor rate of convergence in solving large gradients associated with cooling and heating. The undulations can be minimized by using large number of Eigen values and at the expense of large computational times. As the maximum tensile stress

generated during cooling does not vary significantly during cooling, we have performed this analysis at moderate number of Eigen values.

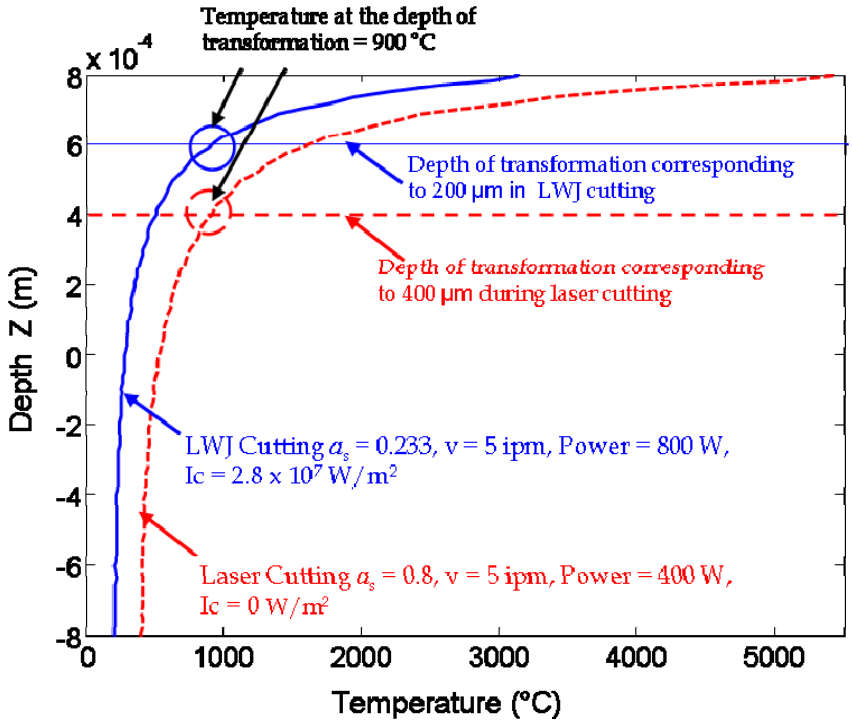

Figure 6.9: Temperature plot across the thickness at the maximum heating instance for both laser and LWJ cutting

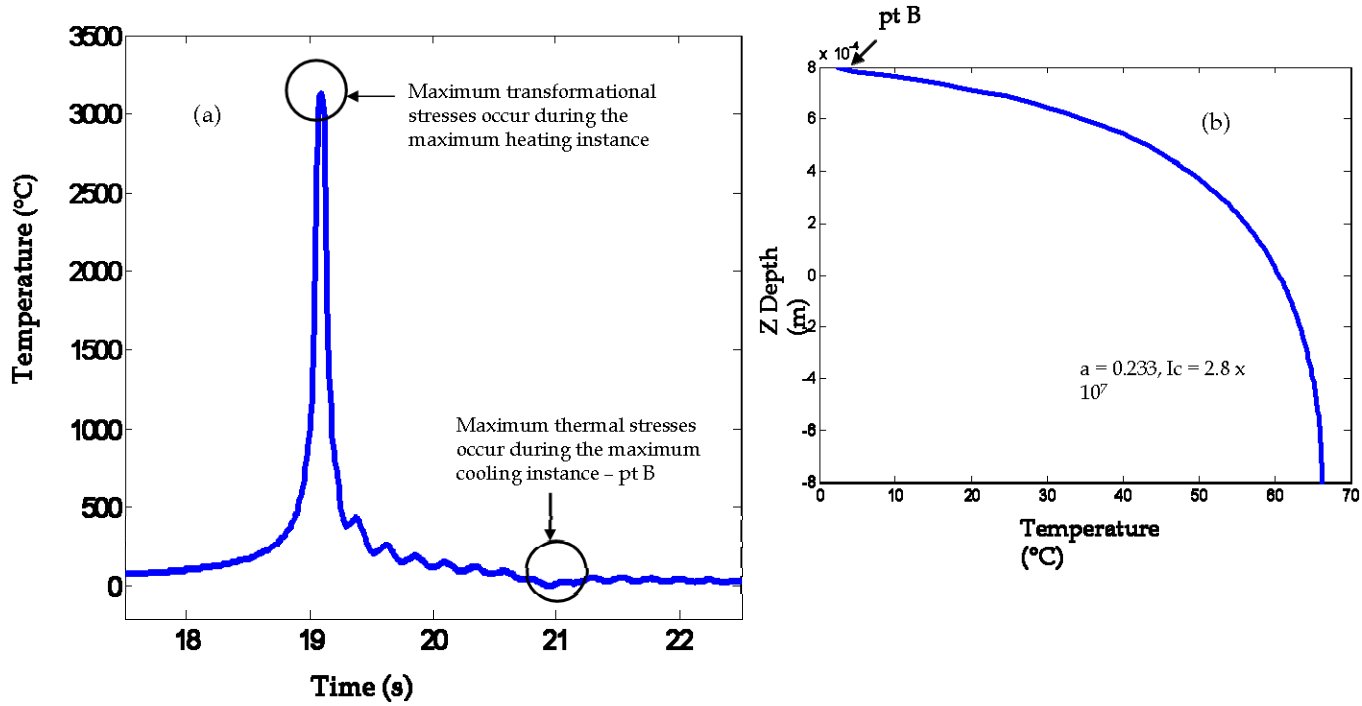

Figure 6.10: (a) A typical temperature profile with respect to time at a point on the surface (b): A typical temperature profile across thickness during maximum cooling instance

6.5.4 Determination of thermal stress intensity factor and transformation stress intensity factor

The thermal stress distributions at three different depths (top, center, and bottom) are plotted with respect to time in Figure 6.11 for line energy of 368 J/mm. It can be noticed that the stresses on the top reach a maximum of 180 MPa while in the case of low conductive ceramics such as alumina (see Ref [41]) the stresses are in the order of few GPa, an order of magnitude higher than the high conductive ceramics. Thermo-mechanical stresses can explain the fracture mechanisms in low conductive ceramics while both thermo-mechanical and thermo-chemical stresses are required to explain the fracture mechanism in high conductive ceramics. The Griffith Energy for crack channeling due to thermal stresses is plotted in Figure 6.12 as a function of normalized crack depths (a/w). The plot confirms that the thermal Griffith Energy is quite low in comparison to the threshold energy level. Hence, chemical transformation should contribute to the driving energy for material separation.

The volume expansion caused by the oxidation of nitrides could result in the additional driving forces. The substrate's cubic boron nitride has a lattice spacing of 3.616 Å [42]. The binder aluminum nitride is either has a cubic structure of lattice spacing of 4.38 Å or a wurtzite structure of lattice spacing a = 3.11 Å and c = 4.979 Å [42]. The oxidized products namely hexagonal boron oxide and hexagonal aluminum oxide have higher volume than the nitrides. The lattice constants of boron oxide are a = 4.336 Å and c = 8.340 Å [43] while the lattice spacing of aluminum oxide are a = 4.76 Å and c = 12.99 Å [44]. This roughly corresponds to a volume increase of a minimum of 240% up to a maximum of 310% depending on whether the substrate's AlN has a wurtzite structure or a cubic structure. This difference in the lattice volume can be calculated from the lattice volume of the substrate and the oxidized material as shown in the Table 6.3. The large increase in volume of the oxidized material will create a wedge effect that will drive cracks to yield material separation. The properties of the oxidized products are given in Table 6.4.

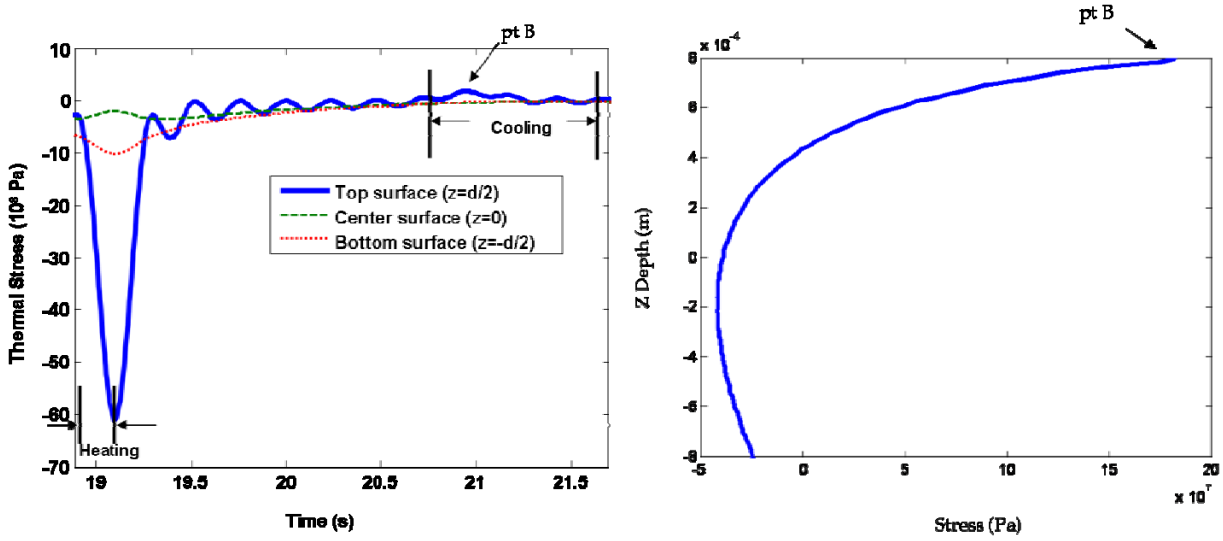

Figure 6.11: (a) Uncoupled quasi-static thermal stress plot at three different depths with respect to time (b): Thermal stress plot across thickness at the maximum cooling instance

Table 6.3: Analysis of various chemical compounds during LWJ machining

Substrate material						
Compounds	Lattice Structure	Lattice Parameters (Å)		Lattice Volume (Å^3)	Percentage	Net Volume (Å^3)
BN	Cubic	3.616		47.28	68.88	32.57
B2O3	Cubic	4.336	8.34	156.80	5.74	9.00
AlN	Cubic or	4.38		84.03	18	15.12
	Wurtzite	3.11	4.979	41.71	18	7.51
				Total Volume (Å^3) (If AlN is Cubic)		56.69
				Total Volume(Å^3) (If AlN has Wurtzite structure)		49.07

Oxidized material						
Compounds	Lattice Structure	Lattice Parameters		Lattice Volume	Percentage	Net Volume
BN	Cubic	3.616		47.28	12.3	5.82
B2O3	Cubic	4.336	8.34	156.80	52.48	82.29
Al2O3	Hexagon	4.76	12.99	764.67	16.38	125.25
AlB2	-					
				Total Volume (Å^3)		213.36

Table 6.4: Properties of oxidized compounds

Compounds	Young's Modulus (GPa)	$Temp_{trans}$ (°C)
Al_2O_3	365 [45]	900 [38]
B_2O_3	324 [46]	900 [39]
AlB_2	-	1100 [40]

To explain the cause of fracture observed during experimentation, we hypothesize that an increase in stress intensity factor due to transformation has aided the crack channeling energy to exceed the critical energy. The calculated minimum and the maximum values of the additional transformational stress intensity factor required for fracture was 4.4 MPa√m and 5.9 MPa√m for 0≤a/w≤0.13. This corresponds to a minimum and a maximum crack mouth opening displacement of 179 nm and 234 nm respectively for a/w of 0.13. The Griffith Energy curve representing the combined effect thermo-mechanical stress and the chemical transformation is shown in Figure 6.12. For a/w ranging from 0.13 to 0.9, the K_I values calculated by either of the formulae (Eqn (20) or Eqn (21)) are nearly equal and hence only one set of values were considered in the calculation of Griffith Energy. Hence, the effect of the chemical transformation has resulted in a wedge which has played a significant part in crack propagation. It is to be noted that even earth worms use this mode of wedge opening technique to open up tougher soil layers [16].

6.6. CONCLUSIONS

The chemical transformation assisted laser machining of the tip-tool material poly crystalline cubic boron nitride has been explained in detail in this work. A mathematical model previously devised has been used to relate laser machining parameters and Griffith Energy for material separation, with the effect of

additional stress intensity factor due to transformation. This wedge based driving of cracks can also be extended to other materials undergoing chemical transformation during machining.

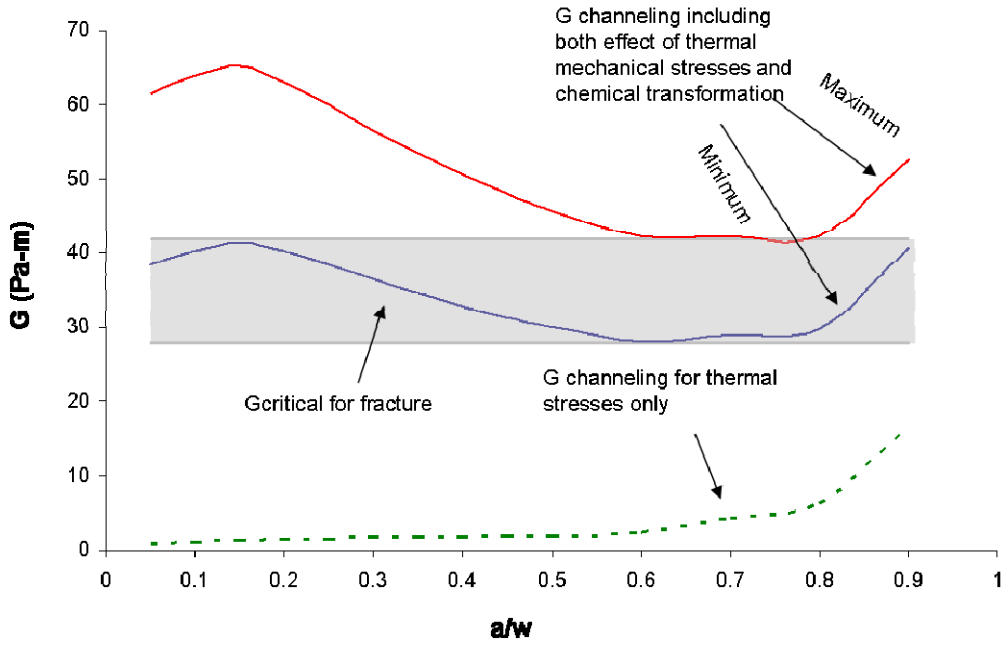

Figure 6.12: Griffith Energy curve for thermal stress and cumulative tensile stresses at various crack depths

ACKNOWLEDGEMENTS

The authors would like to express their gratitude to National Science Foundation for the financial support extended to this work under grant # 0522788.

6.7. REFERENCES

[1] X. Ding, W. Y. H. Liew, and X. D. Liu, "Evaluation of machining performance of MMC with PCBN and PCD tools," *Wear*, vol. 259, pp. 1225-1234, 2005.

[2] D. Kalyanasundaram, G. Shehata, C. Neumann, P. Shrotriya, and P. Molian, "Design and validation of a hybrid laser/water-jet machining system for brittle materials," *Journal of Laser Applications*, vol. 20, pp. 127-134, 2008.

[3] D. Kalyana-sundaram, J. Wille, P. Shrotriya, and P. Molian, "CO_2 Laser/Waterjet machining of Polycrystalline Cubic Boron Nitride," in *Transactions of the North American Manufacturing Research Institute*, vol. 36: Society of Manufacturing Engineers, 2008, pp. 517-524.

[4] V. Pereles-Santiago, M. Washington, P. Brugan, G. Cai, R. Akarapu, S. Pulford, and A. E. Segall, "Faster and damage-reduced laser cutting of thick ceramics using a simultaneous prescore approach," *Journal of Laser Applications*, vol. 17, pp. 219-224, 2005.

[5] C. H. Tsai and C. S. Liou, "Fracture mechanism of laser cutting with controlled fracture," *Journal of Manufacturing Science and Engineering-Transactions of the Asme*, vol. 125, pp. 519-528, 2003.

[6] O. D. Sibailly, F. R. Wagner, L. Mayor, and B. Richerzhagen, "High precision laser processing of sensitive materials by Microjet," presented at Fourth International Symposium on Laser Precision Microfabrication, 2003.

[7] R. Molian, Shrotriya, P., Molian, P.,, "Thermal stress fracture mode of CO2 laser cutting of aluminum nitride " *International Journal of Advanced Manufacturing Technology*, 2007.

[8] B. A. Boley and J. H. Weiner, *Theory of Thermal Stresses*. Mineola, New York: Dover Publications, Inc., 1997.

[9] C. A. Harper, *Handbook of Ceramics, Glasses and Diamonds*: Mc Graw Hill, 2001.

[10] G. Leichtfried, Sauthoff, G., Spriggs, G.E., *Refractory, Hard and Intermetallic Materials*, vol. 2A2, XIII ed: Springer-Verlag, 2002.

[11] E. G. Ng, D. K. Aspinwall, D. Brazil, and J. Monaghan, "Modelling of temperature and forces when orthogonally machining hardened steel," *International Journal of Machine Tools and Manufacture*, vol. 39, pp. 885-903, 1999.

[12] M. A. S. Y. Takashi Taniguchi, "Mechanical Properties of Polycrystalline Translucent Cubic Boron Nitride as Characterized by the Vickers Indentation Method," *Journal of the American Ceramic Society*, vol. 79, pp. 547-549, 1996.

[13] D. Kalyanasundaram, P. Shrotriya, and P. Molian, "Obtaining a relationship between Process parameters and Fracture energy for CO2 Laser/Waterjet Machining of Ceramics," *Journal of Engineering Materials and Technology*, vol. 131, pp. 011005-10, 2009.

[14] L. G. Zhao, T. J. Lu, and N. A. Fleck, "Crack channelling and spalling in a plate due to thermal shock loading," *Journal of the Mechanics and Physics of Solids*, vol. 48, pp. 867-897, 2000.

[15] H. Tada, Paris, P.C., and Irwin, G.R., *Stress Analysis of Cracks Handbook*. St, Louis: Del Research, MI, 1985.

[16] K. M. Dorgan, S. R. Arwade, and P. A. Jumars, "Worms as wedges: Effects of sediment mechanics on burrowing behavior," *Journal of Marine Research*, vol. 66, pp. 219-254, 2008.

[17] R. Walter, L. Ostergaard, J. F. Olesen, and H. Stang, "Wedge splitting test for a steel-concrete interface," *Engineering Fracture Mechanics*, vol. 72, pp. 2565-2583, 2005.

[18] J. Xiao, H. Schneider, C. Dönnecke, and G. König, "Wedge splitting test on fracture behaviour of ultra high strength concrete," *Construction and Building Materials*, vol. 18, pp. 359-365, 2004.

[19] Y. Murakami, *The Stress Intensity factor handbook*. Oxford: Pergamon, 1987.

[20] A. Forderreuther, G. Thurn, A. Zimmermann, and F. Aldinger, "R-curve effect, influence of electric field and process zone in BaTiO3 ceramics," *Journal of the European Ceramic Society*, vol. 22, pp. PII S0955-2219(01)00516-7, 2002.

[21] B. P. Payne, N. S. Nishioka, B. B. Mikic, and V. Venugopalan, "Comparison of pulsed CO2 laser ablation at 10.6 mu m and 9.5 mu m," *Lasers in Surgery and Medicine*, vol. 23, pp. 1-6, 1998.

[22] K. Hamrin, G. Johansson, U. Gelius, A. Fahlman, C. Nordllng, and K. Siegbahn, "Ionization energies in methane and ethane measured by means of ESCA," *Chemical Physics Letters*, vol. 1, pp. 613-615, 1968.

[23] C. D. Wagner, W. M. Riggs, L. E. Davis, J. F. Moulder, and G. E. Muilenberg, *Handbook of X-ray photoelectron spectroscopy*. Eden Prairie, Minnesota: Perkin-Elmer Corporation, Physical Electronics Division, 1979.

[24] G. Soto, W. de la Cruz, and M. H. Farías, "XPS, AES, and EELS characterization of nitrogen-containing thin films," *Journal of Electron Spectroscopy and Related Phenomena*, vol. 135, pp. 27-39, 2004.

[25] C. Guimon, D. Gonbeau, G. Pfisterguillouzo, O. Dugne, A. Guette, R. Naslain, and M. Lahaye, "Xps Study of Bn Thin-Films Deposited by Cvd on Sic Plane Substrates," *Surface and Interface Analysis*, vol. 16, pp. 440-445, 1990.

[26] W. A. Brainard and D. R. Wheeler, "Xps Study of the Adherence of Refractory Carbide, Silicide, and Boride Rf-Sputtered Wear-Resistant Coatings," *Journal of Vacuum Science & Technology*, vol. 15, pp. 1800-1805, 1978.

[27] A. R. Burke, C. R. Brown, W. C. Bowling, J. E. Glaub, D. Kapsch, C. M. Love, R. B. Whitaker, and W. E. Moddeman, "Ignition Mechanism of the Titanium Boron Pyrotechnic Mixture," *Surface and Interface Analysis*, vol. 11, pp. 353-358, 1988.

[28] J. A. Schreifels, P. C. Maybury, and W. E. Swartz, "X-Ray Photoelectron-Spectroscopy of Nickel Boride Catalysts - Correlation of Surface-States with Reaction-Products in the Hydrogenation of Acrylonitrile," *Journal of Catalysis*, vol. 65, pp. 195-206, 1980.

[29] V. I. Nefedov, D. Gati, B. F. Dzhurinskii, N. P. Sergushin, and Y. V. Salyn, "X-Ray Electron Study of Oxides of Elements," *Zhurnal Neorganicheskoi Khimii*, vol. 20, pp. 2307-2314, 1975.

[30] D. J. Joyner and D. M. Hercules, "Chemical Bonding and Electronic-Structure of B2o3, H3bo3, and Bn - Esca, Auger, Sims, and Sxs Study," *Journal of Chemical Physics*, vol. 72, pp. 1095-1108, 1980.

[31] G. Mavel, J. Escard, P. Costa, and J. Castaing, "Esca Surface Study of Metal Borides," *Surface Science*, vol. 35, pp. 109-116, 1973.

[32] J. A. Taylor, "An Xps Study of the Oxidation of Alas Thin-Films Grown by Mbe," *Journal of Vacuum Science & Technology*, vol. 20, pp. 751-755, 1982.

[33] E. Paparazzo, "Xps Analysis of Iron Aluminum-Oxide Systems," *Applied Surface Science*, vol. 25, pp. 1-12, 1986.

[34] K. Arata and M. Hino, "Solid Catalyst Treated with Anion .18. Benzoylation of Toluene with Benzoyl Chloride and Benzoic Anhydride Catalyzed by Solid Superacid of Sulfate-Supported Alumina," *Applied Catalysis*, vol. 59, pp. 197-204, 1990.

[35] G. E. McGuire, Schweitz.Gk, and T. A. Carlson, "Study of Core Electron Binding-Energies in Some Group Iiia, Vb, and Vib Compounds," *Inorganic Chemistry*, vol. 12, pp. 2450-2453, 1973.

[36] J. A. Taylor and J. W. Rabalais, "Reaction of N2-(+) Beams with Aluminum Surfaces," *Journal of Chemical Physics*, vol. 75, pp. 1735-1745, 1981.

[37] M. F. Ashby, *Materials Selection in Mechanical Design*. Oxford, England: Butterworth-Heinemann, 2001.

[38] Y. J. Geng and M. G. Norton, "Early stages of oxidation of aluminum nitride," *Journal of Materials Research*, vol. 14, pp. 2708-2711, 1999.

[39] A. Nechepurenko and S. Samuni, "Oxidation protection of graphite by BN coatings," *Journal of Solid State Chemistry*, vol. 154, pp. 162-164, 2000.

[40] J. M. Mota, M. A. Martinez, F. Velasco, and A. J. Criado, "Preparation of aluminium boride by powder technology," *Ceramics International*, vol. 30, pp. 301-306, 2004.

[41] D. Kalyanasundaram, P. Shrotriya, and P. Molian, "Obtaining a relationship between Process parameters and Fracture energy for CO2 Laser/Waterjet Machining of Ceramics," *Journal of Engineering Materials and Technology - Transactions of the ASME*, Accepted for publication.

[42] K. Lawniczak-Jablonska, T. Suski, I. Gorczyca, N. E. Christensen, K. E. Attenkofer, R. C. C. Perera, E. M. Gullikson, J. H. Underwood, D. L. Ederer, and Z. Liliental Weber, "Electronic states in valence and conduction bands of group-III nitrides: Experiment and theory," *Physical Review B*, vol. 61, pp. 16623, 2000.

[43] G. E. Gurr, P. W. Montgomery, C. D. Knutson, and B. T. Gorres, "The crystal structure of trigonal diboron trioxide," *Acta Crystallographica Section B*, vol. 26, pp. 906-915, 1970.

[44] T. Ishii, M. Gonda, H. Ueda, S. Okayama, and N. Shima, "Aluminum oxide-coated article ". United States Patent 6333103, 2001.

[45] Accuratus, "Alumina Properties."

[46] V. A. Mukhanov, O. O. Kurakevich, and V. L. Solozhenko, "On the hardness of boron (III) oxide," *Journal of Superhard Materials*, vol. 30, pp. 71-72, 2008.

CHAPTER 7. CO2 LASER/WATERJET CUTTING OF POLYCRYSTALLINE CUBIC BORON NITRIDE

(An article published in SME - North American Manufacturing Research Conference 36, Mexico)

D. Kalyan-Sundaram, J. Wille, P. Shrotriya, and P. Molian

Laboratory for Lasers, MEMS, and Nanotechnology

Department of Mechanical Engineering

Iowa State University Ames, IA

7.1. Abstract

Polycrystalline cubic boron nitride (PCBN) is a difficult-to-machine ceramic material due to its ultra-high hardness and good chemical and thermal stability. In this paper, we report a novel CO2 laser cutting method based on crack separation mechanism for electrically insulating PCBN blanks with aluminum nitride as the binder phase. During the localized laser heating of the blank surface in an oxygen-rich environment, the binder phase undergoes chemical transitions resulting in a build-up of tensile stresses due to shrinkage and thermal gradients; these tensile stresses in the surface layers lead to crack formation and subsequent separation of PCBN wafers along the laser path. The material removal mechanism was investigated in both CO2 laser alone and hybrid CO2 laser/waterjet cutting systems. In comparison to CO2 laser alone, hybrid CO2 laser/waterjet system required more energy but produced better cut quality in terms of kerf, cut straightness, taper and surface roughness.

7.2. Introduction

Cubic boron nitride (CBN) is the second hardest material on earth. It is advantageous over diamond, the first hardest material, in terms of greater thermal stability (high temperature) and chemical stability (less reactive to metals like iron and titanium). Due to its ultra-high hardness and high-temperature chemical stability, PCBN tool inserts are used for machining hard cast iron, high chrome alloy steels, high-strength nickel superalloys and powder metal alloys. PCBN is available in two forms: one is in the form of thin layers backed on a cemented carbide substrate and the other is solid cylindrical compact produced by consolidation of boron nitride powders with binders at high pressures and temperatures. The binders infiltrated in PCBN are either metallic (cobalt) or ceramic (TiN and AlN).

Tool inserts are cut from the compact blanks by diamond sawing, electric discharge machining (EDM) and Nd:YAG laser cutting and finished by diamond grinding, lapping, and polishing. A variety of tool geometries such as square, triangular, circular and rhombus are fabricated for use in various machining operations. The main requirements of a manufacturing process in cutting the desired geometry of tool inserts are: capabilities to generate smooth surface, parallel kerf, narrow kerf, minimal heat affected zone and excellent dimensional tolerance enabling precision; and acceptable cutting speed.

Co and TiN-sintered PCBN cause the compacts to be electrically conductive, which allows convenient cutting of the blanks by EDM. However, a family of AlN-sintered PCBN blanks is electrically insulating and thus cannot be cut using EDM techniques. Waterjet cutting of blanks, a slow process, gives rise to wider kerf, poor surface finish and taper limiting the precision. Typically a Q-switched Nd:YAG laser in the fundamental mode is used to machine such PCBN blanks due to its excellent absorption characteristics[1]. However, this type of laser cutting removes the material through melt blow and evaporation mechanisms resulting in the formation of recast layer, conical and wider kerf, rough edge and collateral thermal damage. In order to improve the precision, laser-cut tools need to be finished by diamond grinding [1].

There is considerable interest in investigating novel material removal methods and mechanisms to overcome the deficiencies of conventional laser cutting of PCBN. Hidai and Tokura [2] investigated the hydrothermal-reaction assisted laser drilling of PCBN in steam environment based on measurements of mass loss at high temperatures. CBN film deposited on copper substrate, binder-containing sintered PCBN, and binderless sintered PCBN were irradiated with an Ar-ion laser in water and steam as well as in different gas atmospheres. Single-crystal and binderless sintered CBN reacted very well with steam and thus hydrothermal-reaction-assisted laser machining was effective. However the technique failed in binder-containing sintered CBN.

Swiss Federal Institute of Technology in Lausanne, Switzerland has developed Laser-Microjet® [3], a hybrid technology based on waterjet-guided Nd:YAG laser for machining of PCBN. In this unique laser cutting technique, a free laminar waterjet is used as an optical waveguide to direct the Nd:YAG laser beam onto the sample. The Laser-Microjet® allows precise cutting of PCBN materials with small kerf and good surface finish. Q-switched pulse laser (up to 300 W) of 532 nm wavelength and water pressure of 2-10 MPa was employed for the process. The waterjet prevented any thermal damage and permitted parallel beam transmission through the sample leading to taper-free and narrow kerf features. The tolerances are much smaller than those obtained with conventional laser and EDM processes. However the process suffers from very slow cutting speeds as it reports 70 passes with each pass at a speed of 7 mm/min to cut 3.25 mm thick PCBN sample.

In this work, we report a novel cutting process for PCBN that relies upon development of tensile stresses due to chemical transitions and thermal gradients; these stresses initiate controlled separation of material through crack formation rather than by traditional melting and evaporation. The material separation technique consists of melting and resolidification of thin surface layers of binder-containing PCBN in an oxygen-rich environment. The shrinkage associated with phase transformation and oxidation of surface layers coupled with temperature gradients drive the development of tensile stresses, resulting in crack propagation and material separation. The technique is tested using CO2 laser alone as well as a hybrid CO2 laser/waterjet (CO2-LWJ) machining systems. The CO2-LWJ is a non-traditional hybrid machining process

that has been developed by our group and applied to electronic ceramics such as aluminum oxide and aluminum nitride [4-6]. Details of the design and working principles of CO2-LWJ are described in a NAMRC 35 paper [6]. CO2-LWJ is beneficial over diamond saw, conventional laser and abrasive waterjet cutting processes in improving the precision and is competitive with Nd:YAG Laser-Microjet for improving the cutting speed.

7.3. Experimental Procedure

Cutting experiments were conducted on a commercial grade, electrically insulating PCBN blank (75 mm diameter X 1.6 mm thickness) supplied by Diamond Innovations, Inc. (Worthington, Ohio). PCBN blank is a part of BZN 7000 series with a composition of 82% CBN (particle size of 8-12 μm) and 18% of AlN binder and other impurities. All the experiments were performed on a computer numerically controlled (CNC) worktable using a continuous wave, 10.6 μm wavelength CO2 laser with a rated power of 1500 W (Model 820 Spectra Physics). Three sets of experiments were conducted.

The first set of cutting experiments was carried out with the laser alone and oxygen as an assist gas. The beam from the laser was sent through a circular polarizer and then directed into a focusing lens in a gas-jet cutting assembly. The 127-mm focal length lens produced a theoretical focal spot diameter of 0.2 mm at the sample surface. The laser power was set at 400 W. Oxygen with a pressure of 69 kPa (10 psi) and 138 kPa (20 psi) was delivered through a coaxial nozzle with a diameter of 2 mm. The nozzle was maintained at a standoff distance of 1-2 mm from the surface of the substrate. The sample was placed on x-y positioning table controlled by a computer numerical (CNC) controller. The cutting speed ranged from 4 mm/sec (10 in/min) to 6 mm/sec (15 in/min).

Second set of experiments was carried out with the laser alone and argon as an assist gas in order to identify the role of chemical transformation of surface layers. Assist gas pressure, laser power and cutting speed were maintained to be same as in the first set of experiments.

Third set of cutting experiments was carried out with CO2-LWJ cutting head (details are given in Reference 6) where the laser beam was focused to a spot size of 0.2 mm diameter on the sample surface and air pressure in the coaxial nozzle was held at 35 kPa (5 psi) to protect the lens from spatter. The water-jet pressure was made constant at 3445 kPa (500 psi). The water-jet trailed the laser beam on the workpiece surface with a spacing of 3.1 mm between their centers. The laser power was varied between 400 W and 800 W while the cutting speed was in the range 2.1 mm/sec (5 in/min) to 6.3 mm/sec (15 in/min). Straight-line, single track cuts were made.

Optical and scanning electron microscope (SEM) observations were used to characterize the cut quality features. Kerf width on the top and bottom surface, size of heat affected zone, and taper of cut surface were measured using an optical microscope equipped with an image acquisition system. Surface roughness measurements were performed using a Zygo model 5000 series optical profilometer that has a vertical measurement resolution of 0.1 nm. This instrument based on white light optical interference offers a non-contact, rapid method of characterizing and quantifying 3-D surface data including surface roughness, step heights, critical dimensions, and other topographical features with excellent precision and accuracy. SEM along with energy dispersive spectroscopy was used to identify chemically transformed regions on the cut surface.

7.4. Results and Discussion

Cutting experiments conducted in oxygen-rich environment exhibited crack formation and subsequent material separation along the laser path. While in the case of laser with argon assist gas, only a superficial scribe with no discernible material removal was observed on the PCBN specimens for the same power and cutting speed. The comparison clearly demonstrates that oxidation-induced stress is essential for crack propagation and material separation in CO2 laser cutting of PCBN.

The cut specimens were divided into three different groups: scribed (surface cracks without material separation), scribe-cut (through the thickness crack and snapping at light pressure material separation) and

through-cut (clean fracture and material separation). Figure 7.1 shows how these types of machining are dependent on the energy density parameter P/DV (J/mm^2) where P is the laser power, D is the spot size, and V is the cutting speed.

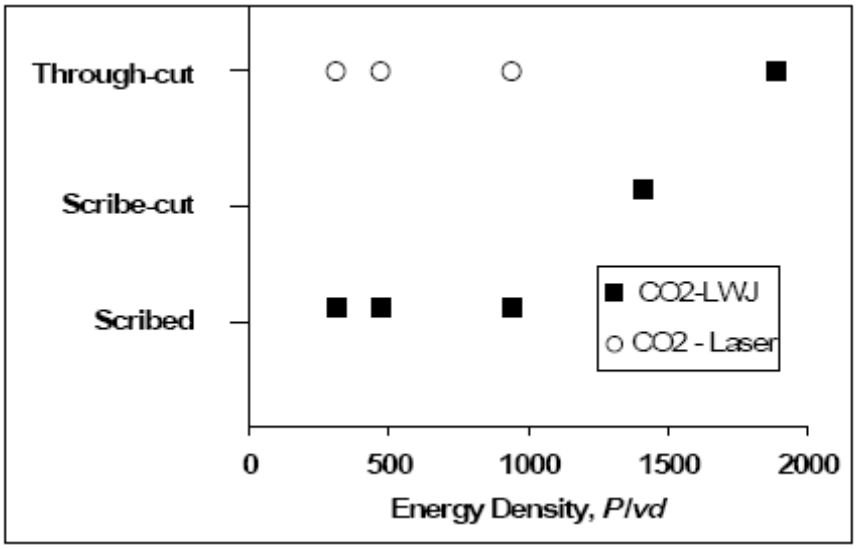

Figure 7.1: Effect of Energy Density

In both cases of cutting, the crack induced in the workpiece propagated in controlled manner along the laser path and was arrested at the end of cut coincident with final beam location. Blind cuts with a through the thickness crack propagation (but no material separation) were used to study the kerf and heat affected zone. Through-cut samples were used to measure the surface roughness and identify chemically transformed regions.

In oxygen-gas assisted dry laser cutting, through-cuts were observed for the energy density range investigated (Figure 7.1). Kerf width on the top surface was 0.2 mm and negligible on the bottom surface indicating that material separation took place due to crack propagation. Although fine kerfs were obtained, the key problems noted were large heat affected zone (~1.5 mm) and undulations in the crack path propagation through the thickness leading to taper and rough surface. Figure 7.2 shows the top view of a typical scribe-cut PCBN illustrating the fine kerf and large heat affected zone. Undulations in the crack path become very pronounced near the starting edge (Figure 7.3a) of the specimens resulting in large taper

(between 18 to 20°) as seen in Figure 7.3b. The cutting mechanism, kerf width and taper of cut remain unaffected by the change in pressure of oxygen assist gas from 69 kPa (10 psi) to 138 kPa (20 psi).

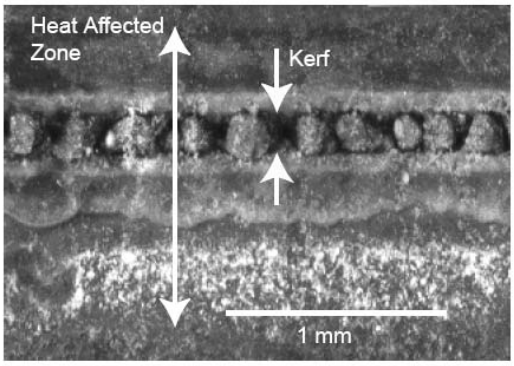

Figure 7.2: Top view of Laser cut PCBN

In contrast to oxygen-assisted dry laser cutting, the type of cut during the LWJ strongly varied with energy density parameter, P/DV as shown in Figure 7.1. At the lowest energy density range (300 – 1000 J/mm^2), scribing of the PCBN sample occurred with a fine kerf width on the top surface (approx 0.05 mm). Increasing the line energy to 1500 J/mm^2 resulted in scribing with a slightly higher but still a narrow kerf and crack propagation through the thickness such that application of light pressure lead to snapping and material separation. At the highest energy density (~1800 J/mm^2), a longitudinal, throughthe-thickness crack propagated along the laser path, leading to clean cut. Kerf width for through-cuts was approximately 0.15 mm which was slightly lower compared to oxygen-assisted, dry laser-cut PCBN surfaces. A side view of a typical LWJ cut PCBN sample is shown in Figure 7.4. In both scribe-cut and through-cut specimens, the crack in LWJ cutting propagated through the thickness along a straight line with no undulations resulting in a straight cut surface with little or no taper (max taper angle ~2°) as depicted in Figure 7.4. For blind cuts, the cracks are not visible at the bottom surface of the cut therefore kerf width at the bottom surface for LWJ cutting could not be measured.

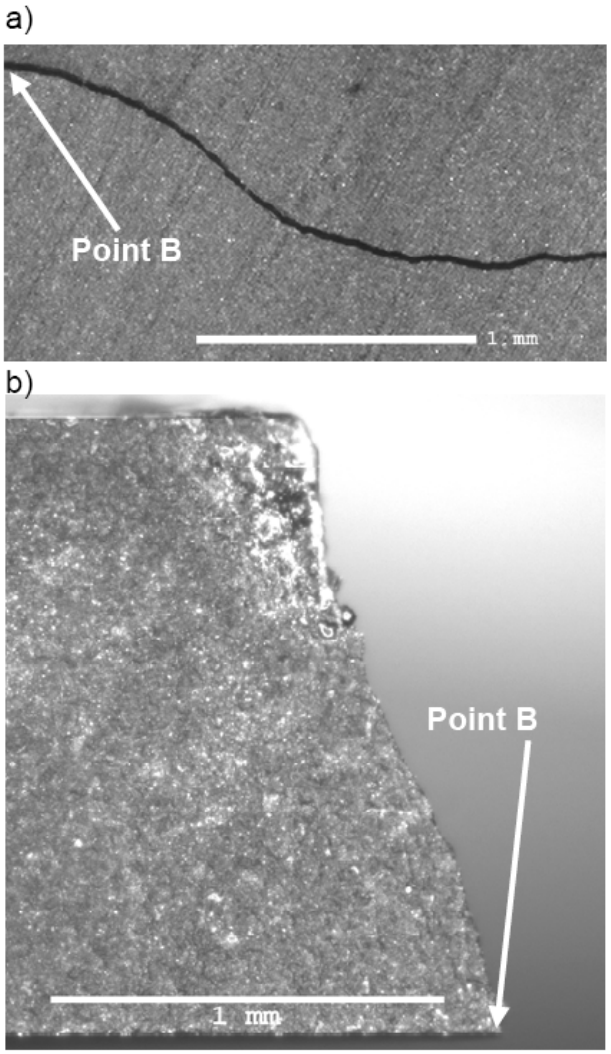

Figure 7. 3: Undulations of crack path a) bottom view b) side view

At the beginning of the LWJ cut, the laser beam is incident on the sample. As a result, a larger kerf is formed on the sample surface for a distance that separates the waterjet from the beam. However the kerf becomes narrower when both laser beam and waterjet are acting on the sample surface as shown in Figure 5. This decrease in the kerf indicates that during LWJ cutting all of the laser power does not reach the sample surface. A significant portion of the laser power is being absorbed by water vapor produced during quenching of heated sample surface which in turn increased the energy density requirement for through-cut as compared to oxygen-assisted laser cutting (Figure 7.1).

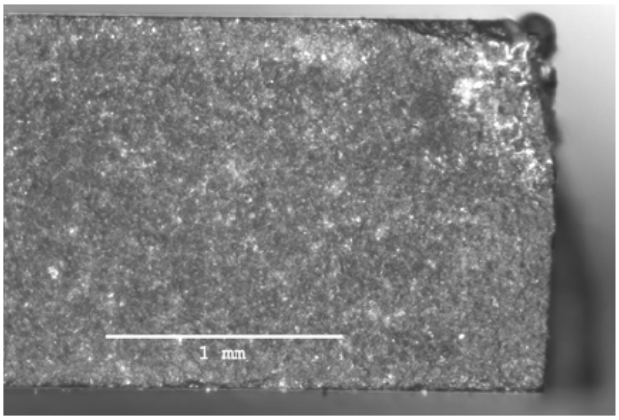

Figure 7.4: Side view of typical cut by LWJ

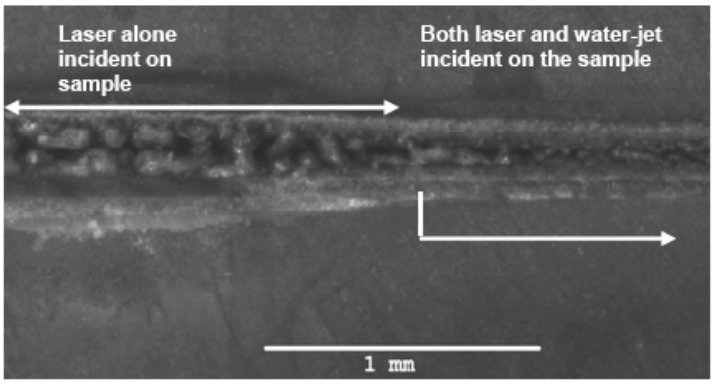

Figure 7.5: Top view of PCBN cut by LWJ highlighting the change in kerf with the introduction of waterjet

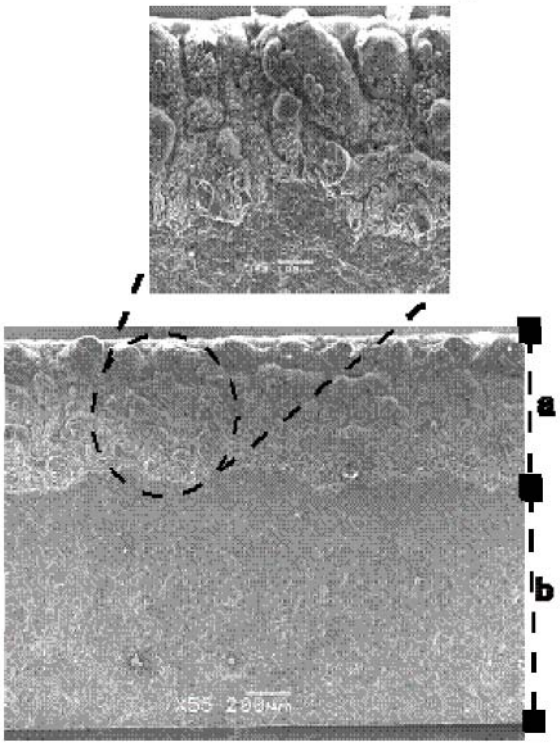

Figure 7.6: SEM image of oxygen assisted laser cut surface. Inset shows details of surface layer undergoing transformation

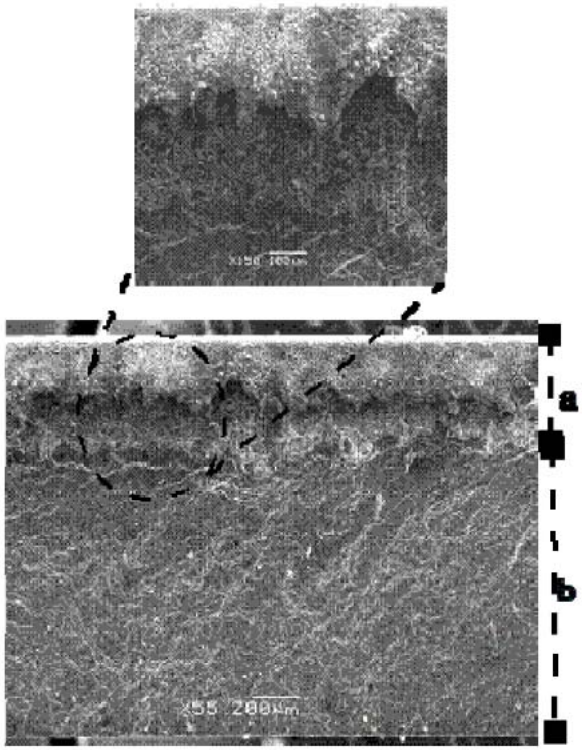

Figure 7.7: SEM image of cross section cut by LWJ. Inset shows the details of transformation

Compositional analysis revealed that the recast layer is covered with small particles of aluminum oxide.

Recast layer is consistently observed to be 30 to 50% larger for samples cut using oxygen-assisted laser

cutting than for LWJ. Representative optical profilometer traces along fractured region (area "b") of oxygen-assisted laser and LWJ cut samples are shown in Figures 7.8 and 7.9 respectively. Roughness of the fractured area is similar in both cases with an average roughness (Ra) approximately equal to 10 μm.

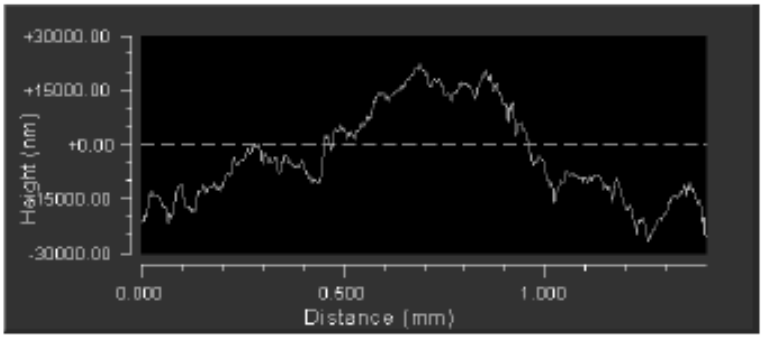

Figure 7.8: Typical profilometer trace of oxygen assisted laser cut sample

The mechanism of crack-cutting for PCBN begins with localized heating and phase transformation of surface layers due to the laser energy. Assuming one-dimensional heat transport, the surface temperature of PCBN during laser irradiation can be determined using the following equation:

$$T_s = T_0 + (I/k)\left(\sqrt{4Dt/\pi}\right) \qquad \text{-- Eqn (1)}$$

where To is the ambient temperature (300 K), I is the absorbed laser power density, k is thermal conductivity (1400 Wm/K [1]), D is thermal diffusivity of PCBN (5 x10^{-4} m^2/s [1]) and t is the interaction time. For a customary laser power density of 2.5 x 10^4 W/cm^2 and interaction time of 0.05 seconds, surface temperature is estimated as 1300 K. Previous experimental studies on oxidation [7-9] have established that AlN starts oxidizing at about 1173 K and rate of oxidation follows a parabolic law above 1273 K. Thus, laser heating of PCBN surface to temperatures above 1173 K in an oxygen-rich atmosphere certainly causes the oxidation of the AlN binder phase and formation of aluminum oxide (recast layer) in the laser-irradiated spot.

As the laser spot travels away, recast layer as well as the substrate cool down to room temperature. Thermal expansion coefficient of aluminum oxide (~ 8.2 x 10^{-6} /K) is higher than PCBN (~ 5.6 x10^{-6} /K [1]) and thermal expansion mismatch will result in development of tensile stresses in the recast layer during

cooling down period. Hence, the residual tensile stresses induce the formation of cracks in recast layer that in turn cause the separation of PCBN samples. Magnitude of tensile stresses in recast layer may be estimated from:

$$\sigma_{res} = E_{Al_2O_3}\left(\alpha_{Al_2O_3} - \alpha_{PCBN}\right)\left(T - T_f\right) \qquad \text{-- Eqn (2)}$$

where E is Young's modulus (aluminum oxide ~ 360 GPa); α is thermal expansion coefficient, T is final temperature (~ 25°C) and T_f is stress-free temperature. Assuming that aluminum oxide layer is stress-free at start of oxidation (~1173 K), magnitude of tensile stress in aluminum oxide particles is approximately 830 MPa. Given that PCBN tool blanks are composed of approximately 18% of AlN binder phase, the average tensile stress in the recast layer is about 150 MPa. At this level of tensile stresses, a simplified estimate of critical crack length, a_{cr}, required for separation of PCBN blank is given by:

$$a_{cr} = \frac{1}{\pi}\left(\frac{K_{IC}}{\sigma_{avg}}\right)^2 \qquad \text{-- Eqn (3)}$$

where K_{IC} is the fracture toughness of PCBN (~2.8 MPa.$m^{1/2}$). This simplified analysis indicates that any crack about 110 μm in length will propagate through the thickness. As shown in Figures 7.6 and 7.7, recast layer on the cut surface is greater the 150 μm for both oxygen-assisted laser as well as LWJ cutting. Hence, during cooling, the presence of highly-stressed aluminum oxide leads to nucleation of the crack that propagates through the entire thickness leading to material separation.

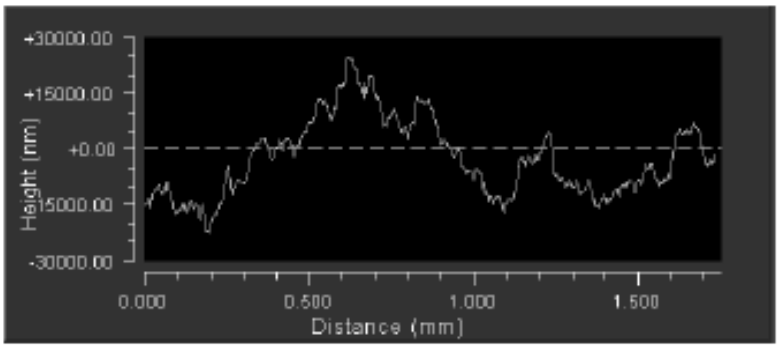

Figure 7.9: Typical profilometer trace of LWJ cut sample

During oxygen-assisted dry laser cutting, laser-formed recast layer and substrate cool down due to dissipation of heat through conduction into the substrate. Given the high thermal conductivity of PCBN, magnitude of thermal gradients is relatively small and the cooling process does not lead to development of significant thermal stresses. Hence only the tensile stresses generated due to oxidation of binder phase near the surface drives the crack through the thickness. As a result, the crack path undulates as it propagates into the unstressed material below the surface layer leading to large taper and deviations (shown in Figure 7.3).

In contrast during LWJ cutting, the heated recast layer is rapidly quenched form the heated state due to the water-jet. The rapid quenching leads to thermal shock and development of additional tensile stresses. PCBN is a highly thermal conductive, hence there will not be significant thermal gradients across the small wafer thickness but the spatial proximity of the heated material under the laser spot and quenched material under the water-jet will lead to large in-plane thermal gradients. As a result, the heated material will be subjected to compressive stresses while the neighboring quenched material will be subjected to tensile stresses. The tensile stresses in recast layer generated due to binder phase oxidation nucleate and drive the crack through the thickness. Superposition of the in-plane thermal tensile stresses due to waterjet quenching ensures that the crack does not deviate from the laser path as it propagates through the thickness leading to material separation with minimal taper of cut surfaces (as shown in Figure 7.4).

7.5. Conclusions

A novel cutting mechanism of CO2 laser cutting of electrically insulating PCBN tool blank with AlN binder phase was investigated. PCBN wafers were cut using oxygen-assisted laser and laser/waterjet (LWJ) machining systems. The material removal mechanism is identified to be controlled fracture of PCBN wafers due to development of tensile stresses associated with high-temperature oxidation of AlN in oxygen-rich environment and thermal gradients induced by the laser beam and waterjet. Results show that oxygen-assisted laser cutting enables splitting of PCBN wafers at lower energy density but has poor cut quality in terms of large heat affected zone and large taper as compared to LWJ cutting. The results also infer that LWJ manufacturing process can be further developed to be an excellent alternative to the currently used methods for machining and cutting PCBN tool blanks.

ACKNOWLEDGEMENTS

The authors gratefully acknowledge the financial support for this research provided by the U.S. National Science Foundation under the Grant DMI-0522788. In addition, donation of PCBN tool blanks by Diamond Innovations, Inc., and helpful discussions with Dr. Steven Webb, Diamond Innovations, Inc. are also gratefully acknowledged.

7.6. References

[1] C. A. Harper, *Handbook of Ceramics, Glasses and Diamonds*: Mc Graw Hill, 2001.

[2] H. Hidai and H. Tokura, "Hydrothermal-reaction-assisted laser machining of cubic boron nitride," *Journal of the American Ceramic Society*, vol. 89, pp. 1621-1623, 2006.

[3] O. D. Sibailly, F. R. Wagner, L. Mayor, and B. Richerzhagen, "High precision laser processing of sensitive materials by Microjet," presented at Fourth International Symposium on Laser Precision Microfabrication, 2003.

[4] C. Barnes, P. Shrotriya, and P. Molian, "A hybrid laser/waterjet processes for brittle materials," presented at SME-North American Manufacturing Research Institute 2006.

[5] D. Kalyanasundaram, G. Shehata, C. Neumann, P. Shrotriya, and P. Molian, "Design and validation of a hybrid laser/water-jet machining system for brittle materials," *Journal of Laser Applications*, vol. 20, pp. 127-134, 2008.

[6] G. Shehata, Molian, P.A., Bastawros, A., and Shrotriya, P, "Surface finish and flexural strength of CO2 laser-cut alumina by evaporative and thermal stress fracture modes," presented at Proceedings of NAMRC 35, Society of Manufacturing Engineers, 2006.

[7] J. W. Lee, I. Radu, and M. Alexe, "Oxidation behavior of AIN substrate at low temperature," *Journal of Materials Science-Materials in Electronics*, vol. 13, pp. 131-137, 2002.

[8] T. Sato, K. Haryu, T. Endo, and M. Shimada, "High temperature oxidation of hot-pressed aluminum nitride by water vapor," *Journal of Materials Science*, vol. 22, pp. 2277-2280, 1987.

[9] D. Suryanarayana, "Oxidation-Kinetics of Aluminum Nitride," *Journal of the American Ceramic Society*, vol. 73, pp. 1108-1110, 1990.

Chapter 8. CONCLUSIONS

This project involved completion of number of tasks related to hybrid laser/waterjet machining of ceramics. Specifics of the work are:

1. Design, fabrication, and validation of a hybrid machining system was achieved.
2. A mathematical model for prediction of temperature and stress fields was developed and was used to relate laser machining parameters to the fracture characteristics of the material.
3. Identified the material removal mechanisms for low and high thermal conductivity ceramics
    a. Thermal shock induced stress fields lead to controlled fracture of low conductive ceramics.
    b. Phase transformation and oxidation induced stresses lead to controlled fracture of high conductive ceramics
4. Significant improvement in cutting speed of ceramics as well as in cut quality compared to other cutting processes was achieved.

8.1 LWJ Machining System

A laser/waterjet cutting head was designed, fabricated, and integrated with an existing CNC laser system for machining hard and brittle materials such as ceramics. Cutting experiments were conducted on alumina to demonstrate the effectiveness of LWJ cutting head. Experimental results showed that laser/waterjet machining utilized the synergistic effects of laser and waterjet for material separation through controlled thermal fracture and required three to five times less energy input than conventional vaporization mode but in comparison to air cooled thermal fracture mode, LWJ material separation required more energy input.

8.2 Mathematical Model

Numerical model were developed to predict temperature, stress field and driving forces for cracks that results in scribing and separation of workpiece. Comparison of experimental and numerical results

indicated that critical value of driving force for channeling cracks determines the transitions between scribing to material separation whereas a critical value of surface energy density determines the transition from controlled separation to uncontrolled cracking of the workpiece. Based on these observations, a map is created to relate process parameters to fracture characteristics of alumina specimens. In other words, the analytical model presented clearly demonstrates that fracture behavior during LWJ machining can be related to the laser parameters and a process map could be generated.

8.3 LWJ Machining of Alumina

The LWJ machining of alumina achieved higher cutting speeds of 150 inch/min (59.2 mm/s) for a laser power of 200 W. This is higher than the previously reported speed of 5-30 mm/s. The cut quality of LWJ samples is better than the laser cut samples. As an example, we have compared samples cut at a laser power of 150 W and at a cutting velocity of 70 inch/min (29.6 mm/s). The kerf width of the sample cut by laser is 350-400 μm, while that cut by LWJ is less than 100 μm. The heat affected zone is around 600-700 μm in laser cut sample, while it ranges between 100-200 μm for LWJ cut sample. The surface roughness of the laser cut sample is 5.3 μm while that of the LWJ cut sample is 4.2 μm. The flexural strength of the laser cut sample is 195 MPa while that of the LWJ cut sample is 322 MPa. This substantiates the fact that LWJ cut quality is better than the laser cut quality.

8.4 LWJ Machining of Zirconia

A process map predicted using the mathematical model was used in the machining of zirconia. Experimental results showed that the mathematical model prediction was more appropriate and heavily relied on the thermal and optical properties of the material. Hence accurate properties data is required. Therefore, the technique is quite useful in determining a relationship between laser cutting parameters and fracture characteristics of ceramic materials. It can also be extended to different materials with suitable modifications. In the machining of zirconia by LWJ machining, no chemical change (such as oxidation or

reduction of the compounds) or phase transformation have been noticed and therefore material separation has been due to thermal shock only.

8.5 LWJ Machining of PCBN

Machining of PCBN was accomplished due to the chemical transformation of the aluminum nitride (binder) to aluminum oxide as well as the partial transformation of boron nitride to boron trioxide. The mathematical model has been used to manipulate the minimum transformational stresses that help in the material separation process and thereby prove the hypothesis. LWJ machining of 1.6 mm thick PCBN substrate resulted in improved cutting velocity of 160 mm/min compared to the previously reported speed of 7 mm/min. A comparison between laser cutting and LWJ cutting is made to understand the benefits of LWJ cutting. Kerf width for laser and LWJ cutting is 216 μm and 148 μm respectively. Similarly the heat affected zone width for laser and LWJ cutting was 1560 μm and 730 μm respectively. However, the surface roughness (Ra) in both cases were almost the same and was equal to 10 μm.

8.6 LWJ Machining of PCD

Experimental and numerical results demonstrate that PCD substrates can be machined along one dimension at high cutting velocity using both CO_2 laser and CO_2 laser/waterjet. Machining is accomplished using novel thermochemical material removal mechanism in which localized heating of PCD leads to phase transformation and the expansion associated with the phase transformation leads to localized loading and controlled crack propagation. The transformational strains calculated from these stresses are about 4% which is much less than the lattice spacing difference between diamond and graphite. The maximum cutting speeds experimentally determined (86.64 mm/s by laser cutting and 43.32 mm/s by CO_2 LWJ cutting) are much higher than previously reported cutting speed of PCD by Nd:YAG laser. However, the overall surface roughness by LWJ cutting is better than the surface roughness obtained in laser cutting.

8.7 Future Work

8.7.1 Multi-pass LWJ Machining of thicker ceramics

The LWJ technique described in this work suits machining of ceramics for thicknesses from 0.5 mm to 1.6 mm. However, single pass cutting of thicker ceramics (~ 4.8mm) resulted either in uncontrolled cracking or unsmooth cut surface (with spatter and recast layer) due to the excessive energy input. Multi-pass cutting has produced cut surface with better cut quality. Modeling of the multi-pass cutting is one of the future scopes of work.

8.7.2 Contour Cutting

The LWJ head has been designed and fabricated with a 'Rotating Housing' that has vertical grooves on its circumference to assist in interfacing of the laser cutting head to the third axis of the CNC positioning table through a belt and pulley system. The rotating housing is designed such that the housing, nozzle, and water inlet can freely rotate with respect to the laser path. This arrangement will help the waterjet (flowing from the water outlet in the nozzle) to rotate about the laser outlet in order to follow the laser path during profile cutting. Efforts with the aid of gas pressure will be undertaken to prevent splashing of water around the peripheral devices such as optics etc. Water-jet pressure determines the rate of quenching and heat transfer on the sample surface and consequently, the magnitude of stresses imposed due to thermal shock. Preliminary design calculations indicate that waterjet pressure of 5 MPa will be sufficient to quench the samples during LWJ machining at maximum laser power of 1500 W. The LWJ system includes a water pump that will be able to attain the required pressure levels. Experiments and numerical analysis need to be conducted to identify the processing parameters required for contour cutting of ceramics.

8.7.3 LWJ Milling

Crack Spalling is third mode of fracture that can occur due to thermal stresses generated in LWJ machining. The spalling mode of fracture can be used to mill pockets of different depths. Ceramic milling will find extensive applications given its brittle nature and chemical inertness which has made conventional

machining and chemical etching non-effective in terms of time and cost. Experiments and numerical analysis need to be conducted to identify the processing parameters required for LWJ milling of ceramics.

8.7.4 3-D Finite Element Formulation

A 3-D finite element formulation of the LWJ machining can be performed to solve for the thermal stresses generated and can be used to check the appropriateness of the stress determined. It can also be used to create a 3-D map of the stress distribution.